ISBN ISBN 978-82-326-4284-7 (printed)
ISBN ISBN 978-82-326-4285-4 (electronic)
ISSN 1503-8181

Doctoral Thesis

Aditya Suneel Sole

NTNU
Norwegian University of
Science and Technology

Doctoral theses at NTNU, 2019:344

Aditya Suneel Sole

Image-Based Bidirectional Reflectance Measurement of Non-Diffuse and Gonio-Chromatic Materials

NTNU
Norwegian University of
Science and Technology
Faculty of Information Technology
and Electrical Engineering
Department of Computer Science

NTNU
Norwegian University of
Science and Technology

Doctoral theses at NTNU, 2019:344

NTNU

Aditya Suneel Sole

Image-Based Bidirectional Reflectance Measurement of Non-Diffuse and Gonio-Chromatic Materials

Thesis for the degree of Philosophiae Doctor

Gjøvik, December 2019

Norwegian University of Science and Technology
Faculty of Information Technology
and Electrical Engineering
Department of Computer Science

NTNU
Norwegian University of
Science and Technology

NTNU
Norwegian University of Science and Technology

Thesis for the degree of Philosophiae Doctor

Faculty of Information Technology
and Electrical Engineering
Department of Computer Science

ISBN ISBN 978-82-326-4284-7 (printed version)
ISBN ISBN 978-82-326-4285-4 (electronic version)
ISSN 1503-8181

Doctoral theses at NTNU, 2019:344
Printed by Skipnes Kommunikasjon as

Declaration of Authorship

I, Aditya Suneel Sole, declare that this thesis titled, 'Image-Based Bidirectional Reflectance Measurement of Non-Diffuse and Gonio-Chromatic Materials' and the work presented in it is entirely my own. Where I have consulted the work of others, this is always clearly stated.

Signed: _____

(Aditya Suneel Sole)

Date: _____

Abstract

Visual appearance of packaging material can vary in terms of perceived colour or lightness properties with a change in illumination and viewing directions mainly due to its optical properties. This gives a desirable visual appearance and makes the package look attractive and standout on a supermarket or an airport duty-free shelf. To characterise and reproduce such a material, objective measurements in terms of the amount of the light incident and reflected from the material surface are performed. To perform such measurements, standardisation bodies like the International Commission on Illumination (CIE) and the ASTM International recommended measurement geometries based on the material optical properties. Single measurement geometries recommended by these standardisation bodies, however, are inadequate to measure and characterise materials that reflect the incident light in a non-diffuse and goniometric way. Bidirectional measurements are required to characterise such packaging print materials which can be difficult and time consuming.

Gonio-spectrophotometers that measure at a broad number of illumination and viewing directions are commercially available and used to perform bidirectional reflectance measurements. Gonio-spectrophotometers can be slow due to moving light source, to illuminate a flat measurement sample, and a detector, to record the light reflected from the sample surface. To overcome these drawbacks, image-based measurement techniques have been proposed and presented in the past. An image-based measurement setup uses a camera as a detector to objectively measure the incident and reflected light from the material surface.

In this thesis we investigate the applicability of using an image-based measurement technique to perform bidirectional reflectance measurements, analytically estimate, and represent the bidirectional reflectance distribution function (BRDF) of flexible and homogeneous packaging print materials having different optical properties.

We present an image-based measurement setup (measurement setup) to perform fast bidirectional reflectance measurements of flexible, homogeneous packaging print materials. The packaging materials measured in this thesis show reflectance properties that vary from diffuse to non-diffuse and gonio-chromatic. We evaluate the accuracy of the measurement setup by comparing it against two commercially available gonio-spectrophotometers. The uncertainty in calculating the incident and viewing directions was large and is dependent on the physical measurements within the measurement setup. The practical use of such a setup

to perform bidirectional reflectance measurements is dependent on the material to be measured, precision of the physical measurements within the measurement setup and their implications.

Further we investigate the suitability of using the measurement setup to perform bidirectional reflectance measurements and analytically estimate material BRDF using an analytical reflectance model. Measurements from two commercially available gonio-spectrophotometers are used to validate the measurement setup.

Depending on the material reflectance properties, different combinations of reflectance models, measurement datasets and cost functions are used for estimation. A salient measurement dataset is investigated for BRDF estimation and representation of the materials measured in this thesis. Retro-reflective measurements obtained using the measurement setup provided a good BRDF estimation for visual representation. Measurements in addition to retro-reflective measurements did improve the visual representation of the material with gonio-chromatic relfectance property.

The measurement setup can be used as a tool to generate BRDF datasets of flexible, homogeneous, and isotropic materials having different reflectance properties provided precise physical measurements within the measurement setup are performed.

Acknowledgment

There are many who I would like to acknowledge, without their help and support it would have not been possible to complete this thesis. Foremost, I would like to express my sincere gratitude to my supervisors associate professor Peter Nussbaum and professor Ivar Farup for their continuous support during my Ph.D. study and research. Many thanks go to my former supervisor professor Jon Yngve Hardeberg and professor Phil Green for their support and guidance in the initial years of the study.

Besides by supervisors, I would like to thank the rest of my thesis committee: professor Philipp Urban, associate professor Vein Chung, and associate professor Daniel Nyström for their encouragement, insightful comments, and hard questions.

My sincere thanks also go to Dr. Shoji Tominaga for his support, guidance, and collaboration during the Ph.D. studies and his valuable suggestions to the research topic. Thank you professor Horiuchi Takahiko at Chiba University and Dr. Shoji Tominaga for access to their laboratory and the goniospectrophotometer instrument for measurements. Thank you for supporting me during my internship at your laboratory at Chiba University, Chiba, Japan in 2014.

Many thanks to Niklas Johansen, Ole Norberg and Mattias Andersen at Mid Sweden University, Sweden for their support in terms of access to laboratories and the goniospectrophotometer for measurements, valuable discussions and suggestions regarding the topic and measurement approach. Thanks to Mohammed Bouzidi for fixing the film projector that was used in the sample measurements at the Colourlab and to Mekides Assefa Abebe for discussions and suggestions related to the HDR image capture and generation.

I would also like to thank members of the Norwegian Colour and Visual Computing Laboratory: Marius Pedersen, Eivind Johansen, Faouzi Alaya Cheikh, Sony George, Casper Find Andersen, Dag Waaler, Giuseppe Claudio Guarnera, Dar'ya Guarnera, Vlado Kitanovski, Mohib Ullah, Helene B. Midtfjord, Reiner Eschbach, Binu Devassy, Anne Kristin Kvitle, Gregory High, and others.

Special thanks to the members of the former Faculty of Information and Media Technology at Gjøvik University College: Hilde Bakke, Simon McCallum, Rachael McCallum, Urszula Nowostawska, and others. I would also like to thank in particular Dr. Morten Irgens, Kathrine Markengbakken, Terje Stafseng, and Dr. Nils Svendsen for providing the funding from the department to start my Ph.D. studies.

Thank goes out to the CP7.0 project and MUVApp project consortium and

members for their support.

Special thanks to Dr. Janicek Petr and Dr. Panak Ondrej for their collaboration and support in the research carried out at the University of Pardubice, Pardubice, the Czech Republic in 2017.

I would also like to thank Kari Lauritzen, Ragnhild Fjeld, professor Akshay Joshi, my dear friends Aditya Deshpande, Salil Nirkhee, Sayli Nirkhee, Kiran Deshpande, Ankur Tade, Deepa Tade, Deepti Mishra, Aland Mendoza, Sashidharan Komandur, Sushant Deshpande, Amit Athavale, Shrikala Kannade, and Mandar Khandekar for their support and encouragement.

My deepest appreciation is due to my family and extended family for all their love and encouragement. For my parents, Suneel Rajaram Sole and Smita Suneel Sole and my elder brother Siddharth who raised me with love and supported me in all my pursuits. For my mother-in-law for her kind words and encouragement. Towards my darling Manasvi for being such a sweet and supportive daughter. And most of all for my loving and supportive wife Snehal whose faithful support during my Ph.D. is so much appreciated.

Thank you all.

Gjøvik, Norway
December 2019
Aditya Suneel Sole

Contents

Figures

List of Papers

Paper I - Paper VII are the main contribution of this thesis. In addition, **Paper VIII** and **Paper IX** are supplementary papers that relate to the main contribution of this thesis.

List of Included Papers

Paper I

A. Sole, I. Farup and S. Tominaga, 'An image based multi-angle method for estimating reflection geometries of flexible objects', in *Color and Imaging Conference*, vol. 2014, Society for Imaging Science and Technology, 2014, pp. 91–96

Paper II

A. Sole, I. Farup and S. Tominaga, 'Image based reflectance measurement based on camera spectral sensitivities', *Electronic Imaging*, vol. 2016, no. 9, pp. 1–8, 2016, ISSN: 2470-1173

Paper III

A. Sole, I. Farup, P. Nussbaum and S. Tominaga, 'Evaluating an image-based bidirectional reflectance distribution function measurement setup', *Applied Optics*, vol. 57, no. 8, pp. 1918–1928, 2018

Paper IV

A. Sole, I. Farup and T. Shoji, 'An image-based multi-directional reflectance measurement setup for flexible objects', in *Measuring, Modelling, and Reproducing Material Appearance 2015*, SPIE/IS&T Electronic Imaging 2015, 2015

Paper V

A. Sole, I. Farup and P. Nussbaum, 'Evaluating an image based multi-angle measurement setup using different reflection models', *Electronic Imaging*, vol. 2017, no. 8, pp. 101–107, 2017, ISSN: 2470-1173

Paper VI

A. Sole, I. Farup, P. Nussbaum and S. Tominaga, 'Bidirectional reflectance measurement and reflection model fitting of complex materials using an image-based measurement setup', *Journal of Imaging*, vol. 4, no. 11, 136:1–16, 2018

Paper VII

A. Sole, G. C. Guarnera, I. Farup and P. Nussbaum, 'Measurement and rendering of complex non-diffuse and goniochromatic packaging materials', *Manuscript submitted for publication*, 2019

List of Related Papers

Paper VIII

P. Nussbaum, A. Sole and J. Y. Hardeberg, 'Analysis of color measurement uncertainty in a color managed printing workflow', *Journal of Print and Media Technology Research*, no. 1, pp. 7–24, 2012

Paper IX

P. Janíček, E. Schützová, O. Panák, A. S. Sole and P. Nussbaum, 'Measurement of bidirectional reflectance distribution function on custom made gonio spectrophotometer', *Scientific papers of the University of Pardubice. Series A, Faculty of Chemical Technology. 24/2018*, 2018

Chapter 1

Introduction

1.1 Context

Packaging/wrapping material plays an important role in the industry. The appearance of a package can highly influence the buyer's choice and may increase the sales of a product. To make a package look attractive, and stand out on a supermarket or airport duty-free shelf, a wide range of materials are involved in production process of a packaging for example decor paper, cardboard, plastics, metallic foils, special effect printing inks (colour changing effects), coatings, etc. Packaging material can be printed using inks that contain colour pigments and/or special effect pigments and often undergo a finishing process, like a varnish coat or embossing. This gives the package a shiny appearance thus making the final package look rich, desirable, and of high quality.

Special effect pigments may contain metal flakes that specularly reflect light that is incident on it, or pearlescent pigments that reflect different parts of the incident light spectrum in different directions. Pearlescent pigments are also known as pearl interference pigments and containing metal oxide layers on transparent mica platelets. Inks with special effect pigments are often printed on paper or cardboard materials using conventional printing techniques (for example, offset, screen printing) to produce packaging materials that can be used for products like perfume bottles, decor articles, liquor bottles, chocolates, jewelry, etc [10].

Paper or plastic packaging material printed using special effect pigments produce a desirable appearance in terms of perceived colour and lightness variation to change in the illumination and viewing directions [11]. Measuring such materials with an appropriate geometry (illumination and viewing direction) is therefore important and will affect the measurement output [12]. To measure such materials, Takagi *et al.* [13] mentioned about using 1485 different measurement geometries, whereas, Ferrero *et al.* [14] showed that a maximum of 10 geometries could be sufficient to characterise the colour shift of the gonio-chromatic materials. Performing these many measurements can, however, be practically difficult and time-consuming. Instruments with a single measurement geometry, like $45° : 0°$ and sphere-based geometries, are recommended by International Commission on Illumination (CIE) [15] to measure traditional light-absorbing pigments printed on

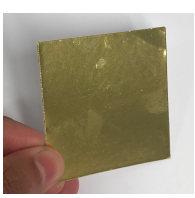

(a) Photograph - 1

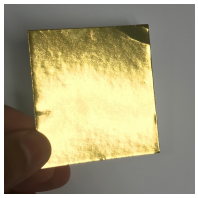

(b) Photograph - 2

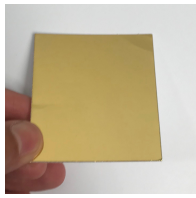

(c) Photograph - 3

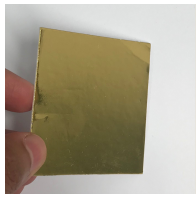

(d) Photograph - 4

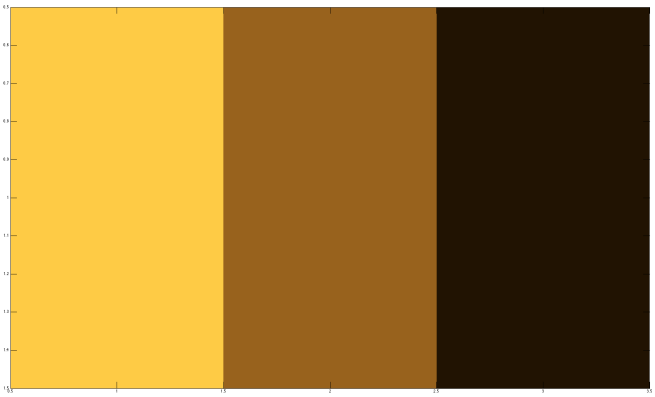

(e) Measured using single measurement geometries: $di : 8°$ (left), $de : 8°$ (middle), and $45° : 0°$ (right).

Figure 1.1: Perfume bottle box package (Gold) photographed in different directions. Measured using single measurement geometries and visualised using a display profile.

diffuse materials like paper and cloth. Single measurement geometries are sufficient to characterise reflectance of such diffuse materials in a way that correlates well with how we perceive material appearance [15] but are inadequate to measure and characterise prints produced using special effect pigments [11, 16–19]. To demonstrate this, we measured a perfume bottle box package, that is produced using a metallic gold colour ink printed on cardboard, using the conventional single measurement geometries, $45° : 0°$, $di : 8°$, and $de : 8°$. The geometries, $di : 8°$, and $de : 8°$, are sphere-based measurement geometries, as defined in [15], to measure the reflectance of the sample that is irradiated by an integrating sphere. The radiation reflected from the sample surface is received at 8° off the sample normal. In specular excluded geometry ($de : 8°$) the radiation reflected in the direction of the receiver from the mirror angle is blocked using a black-trap. Figure 1.1 shows a photograph of the package and the visualisations obtained from the measurements. Based on the measurement geometry, the visual appearance of the packaging material is different. Bidirectional measurements are therefore

needed to characterise and obtain a reflectance function of the material that can characterise the material reflectance properties in a way such that it can correlate well with how we perceive material appearance [11].

ASTM International (ASTM) recommended measurement geometries [20, 21], different from the recommendations made by CIE [15], and are based on the material optical properties. Multi-angle spectrophotometers that measure at a fixed number of measurement geometries (more than one illumination and viewing direction) and gonio-spectrophotometer that measure at a broad range of illumination and viewing directions are commercially available and used for bidirectional reflectance measurements [10]. These instruments record the ratio of the reflected and incident power (ϕ_r/ϕ_i) at multiple illumination and viewing directions. The reflectance function of material can be computed in terms of the bidirectional reflectance distribution function [22] using the obtained measurements.

When using a gonio-spectrophotometer, the material to be measured should be lying flat while the light source and the sample or the detector rotates to perform bidirectional measurements [3]. This can be time-consuming and relatively expensive when performing measurements during high-speed production and quality control of the packaging print materials using conventional printing techniques. Image-based measurements can be performed to address the above limitations. Instruments using image-based measurement techniques have been used in the past [23, 24] for velvet and human skin measurements, and within the computer graphics field [24, 25]. They perform bidirectional measurements at a relatively fast speed and can easily be used during high-speed production and quality control of the packaging print materials. The obtained measurement can be used to analytically estimate material BRDF using different reflectance models. Material appearance can be visualised by generating photo-realistic images using the estimated bidirectional reflectance distribution function of material and different physically based rendering techniques [26, 27].

1.2 Thesis Objective

The overall objective of the thesis is to investigate the applicability of using an image-based measurement technique, herein referred to as measurement setup, to perform bidirectional reflectance measurements of flexible and homogeneous packaging print materials having different reflectance properties. Second, analytically estimate the bidirectional reflectance distribution function of materials using different reflectance models and represent material appearance. With this we can outline the following research questions:

RQ1 Is it possible to perform bidirectional reflectance measurements of flexible homogeneous packaging print materials in a relative fast and in-expensive way?

RQ2 How good is the proposed measurement setup in terms of measurement accuracy in comparison to a commercially available gonio-spectrophotometer?

RQ3 Is it possible to analytically estimate and represent material BRDF using

reflectance models and the measurement data obtained using the measurement setup?

RQ4 What will be an optimal dataset that is enough to analytically estimate material BRDF of flexible packaging print materials with non-diffuse and gonio-chromatic reflectance properties? Would a single photograph captured using the measurement setup be enough?

RQ5 Are retro-reflective measurements sufficient to estimate BRDF of materials with gonio-chromatic reflectance properties?

RQ6 Is it possible to visualise the gonio-chromatic effect of material using its BRDF that is estimated analytically with a reflectance model and the measurements obtained using the measurement setup?

To address these research questions, we divide the work carried out in this thesis into two parts as described below.

Part 1 - Imaging and Instrumentation

In part 1, we implement the measurement setup using a point light source, as an illuminant, and a commercially available DSLR camera, as a detector, to perform bidirectional reflectance measurements of flexible and homogeneous packaging print materials (investigated in **Paper I** [1] and **Paper II** [2]). We estimate measurement accuracy of the measurement setup by comparing it with commercially available gonio-spectrophotometers (investigated in **Paper III** [3]).

Part 2 - BRDF measurement and representation

In part 2, we investigate the suitability of using the measurement setup to measure packaging print materials with different reflectance properties (from lambertian to specular and angle dependent reflectance [10]), analytically estimate material BRDF using reflectance models (investigated in **Paper II** [2], **Paper IV** [4], **Paper V** [5], **Paper VI** [6], and **Paper VII** [7]) and represent material appearance using the estimated material BRDF (investigated in **Paper VII** [7]).

1.3 Thesis Outline

This thesis is divided into four main chapters, Chapter 2, Chapter 3, Chapter 4 and Chapter 5. In Chapter 2, we provide the relevant background in terms of notations, definitions, and literature related to the topic of this thesis. Chapter 3 gives an overview of the main contributions of the included papers. In Chapter 4 we discuss the findings of this thesis, applicability of the measurement setup and the practicality it brings to the field of material appearance measurement and representation. Chapter 5 concludes the work followed by Chapter 6 that talks about future work and activities within the thesis topic.

Chapter 2

Background

This chapter covers the most relevant literature that is related to the work carried out in this thesis. Wherever needed, for a detailed review of the relevant topics, the reader is referred to the necessary literature. This chapter is divided into three parts as follows:

- Visual appearance and packaging print materials
- Bidirectional reflectance measurements
- BRDF models and representation

2.1 Visual Appearance and Packaging Print Materials

In the print and packaging industry, the visual appearance of the printed packaging material is one of the many parameters that affect customer choice for purchase and use of a product the package is carrying, for example, perfume or liquor bottles.

The visual appearance of an object is a combination of different chromatic and geometric attributes generated due to the interaction of the material surface with light incident on it in a given condition [28, 29]. CIE [29] defined the overall appearance of material as '*visual sensation through which an object is perceived to have attributes such as size, shape, colour, texture, gloss, translucency, opacity, etc*'. Using the material optical properties, the visual appearance of the material surface can be classified into colour, gloss, translucency and texture [29]. As described in [29], incident light spectrally absorbed and diffusely reflected by an opaque material tells us about the colour of the material. A material surface with diffuse reflecting property scatter the incident light in all directions instead of just in the specular direction ($\theta_i = \theta_r$). Incident light reflecting off an opaque material surface in and around the specular direction gives the perceived gloss information. Translucency is a subjective term that describes the amount of light transmitted through the material and texture is defined as '*the visible surface structure depending on the size and organisation of small constituent parts of a material*' [29].

Packaging materials printed using traditional light-absorbing inks and special effect pigments having different optical properties result in an unique visual

appearance of the printed material surface. The optical properties of such printed materials are dependent on different materials and process parameters [10, 30–32]. The traditional light-absorbing inks contain pigments that are spherical particles [10] and spectrally absorb part of the incident light and scatter the remaining part to give a diffuse reflection [33]. Visually, the appearance of the material printed using ink that contains this kind of pigments is independent of the illumination and viewing direction. Special effect pigments such as the one used in metallic inks contain metal flakes that specularly reflect the incident light. The perceived brightness from metallic inks is dependent on the viewing direction but independent of the illumination direction. Perceived hue and chroma, however, is independent of the illumination and viewing direction [34]. Inks containing pearlescent pigments are made using thin metal oxide layers on transparent mica platelets [30]. These metal oxide layers can have different refractive indices that help reflect different parts of the light spectrum and light intensity in different directions [30, 34–36]. Packaging material printed using metallic inks can be termed as 'non-diffuse' materials due to their specular reflectance properties, while, materials printed using pearlescent coatings are termed as 'gonio-chromatic' materials as their appearance (in terms of colour) changes with a change in illumination and viewing directions [34] resulting in a desirable and visually appealing appearance.

Even though the change in visual appearance, in terms of perceived colour and gloss, with the change in illumination and viewing direction can be visually appealing, it is difficult to characterise and objectively measure properly. Bidirectional measurements are needed to characterise and objectively describe such materials [10, 11, 13, 14, 16, 18, 34]. The light reflected from the material surface in a given spectral and geometrical condition should help describe and quantify the interaction of light with the material surface (absorbed, reflected, transmitted, etc) and characterise the appearance of a material surface in the given condition. Reflectance, which is a ratio of the reflected radiant flux (Φ_r) to the incident radiant flux (Φ_i) in the given conditions of spectral composition, polarization, and geometrical distribution [37, 38] is widely used as a measure to quantify and describe the interaction of light with an opaque material surface.

Section 2.2 covers the terminology, definitions, and literature necessary to understand reflectance and reflectance measurements in the context of the work carried out in this thesis.

2.2 Bidirectional Reflectance Measurements

2.2.1 Bidirectional Reflectance Distribution Function

Bidirectional reflectance measurements are used in calculating the bidirectional reflectance distribution function (BRDF) of a material. BRDF is a radiometric function that describes how a light ray incident on an opaque homogeneous surface gets reflected. It is an approximation of the bidirectional sub-surface scattering reflectance distribution function (BSSRDF) that ignores sub-surface scattering with

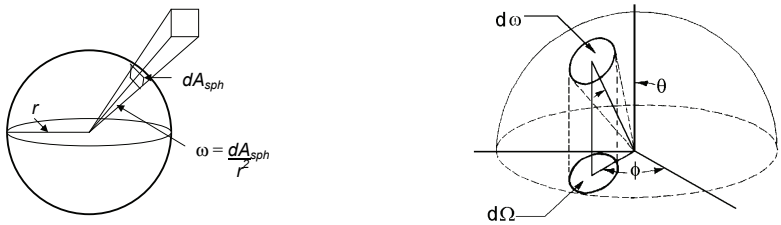

(a) ω **(b)** Ω

Figure 2.1: Solid angle Figure 2.1a and Projected solid angle Figure 2.1b [Images adapted from [37]].

an assumption that the incident light on an opaque homogeneous surface is reflected from the same point [22].

Next, we define in brief the radiometric terminology needed for the BRDF definition and measurements. The definitions are referred from [37] and [39]. For a comprehensive review on radiometry please refer [37, 39, 40].

Radiometric Definitions

Radiant Flux, (Φ), is energy (Q) per unit time t as shown in Equation (2.1) (unit: W).

$$\Phi = \frac{dQ}{dt} \tag{2.1}$$

Solid Angle, (ω), is the ratio of spherical area dA_{sph} to the square of the sphere radius (r) as shown in Equation (2.2) and Figure 2.1.

$$\omega = \frac{dA_{sph}}{r^2} \tag{2.2}$$

Projected Solid Angle, (Ω), is defined as the solid angle projected onto the plane of observation as shown in Equation (2.3). The unit of projected solid angle is (sr). θ is as defined in Figure 2.1.

$$d\Omega = d\omega \cos(\theta) \tag{2.3}$$

Radiant Intensity, (I), is flux emitted per unit solid angle (ω) in a specific direction (units: W/sr) as shown in Equation (2.4).

$$I = \frac{d\Phi}{d\omega} \tag{2.4}$$

Irradiance, (E_i), is a function of position on the given surface defined as flux per unit area incident on a surface area (A_p) (units: W/m^2) as shown in Equation (2.5).

$$E = \frac{d\Phi}{dA_p} \tag{2.5}$$

Inverse Square Law is an approximation in which irradiance from an isotropic point light source varies inversely with the square of the distance between the surface and the light source [37]. Equation (2.6) gives the relationship between irradiance and distance between the point light source and the surface that is normal to it.

$$E = \frac{\Phi}{A_P} = \frac{I}{D^2} \tag{2.6}$$

In Equation (2.6), D is the distance between the point light source and the surface. For surface orthogonal to the point light source a $\cos\theta$ term is introduced as shown in Equation (2.7)

$$E = \frac{\Phi}{A_P} = \frac{I\cos\theta_i}{D^2} = \frac{d\Phi\cos\theta}{d\omega D^2} \tag{2.7}$$

In Equation (2.7), θ is the angle between the normal to the surface and the direction of the point light source.

Radiance, (L), describes the amount of light at a given surface. It is defined as flux (Φ) per unit area (A_P) at point P, per unit projected solid angle (Ω) (unit: $W/m^2.sr$) as shown in Equation (2.8).

$$L = \frac{d^2\Phi}{dA_P cos\theta d\omega} = \frac{d^2\Phi}{dA_P d\Omega} \tag{2.8}$$

Radiance Factor, (β), is the ratio of radiance $L(\theta_i, \phi_i, \theta_r, \phi_r)$ reflected from a surface in a infinitesimal solid angle to the radiance reflected by a perfect reflecting diffuser L_{ref} in the same illumination and viewing conditions [41]. In a generalised form, it is defined as shown in Equation (2.9).

$$\beta = \frac{L(\theta_i, \phi_i, \theta_r, \phi_r, \lambda)}{L_{ref}} \tag{2.9}$$

From a perfect white diffuse material, the radiance reflected $(L_{ref})$is proportional to the incident irradiance (E) as $L_{ref} = E\pi$ [39]. BRDF can therefore be calculated using $f_r = \frac{\beta}{\pi}$ relation.

BRDF

As defined by Nicodemus *et al.* [22], BRDF is a ratio of the radiance reflected from the sample surface to the irradiance at the sample surface and is given as

$$f_r(\mathbf{l}, \mathbf{v}) = \frac{dL_r(\mathbf{v})}{dE_i(\mathbf{l})} = \frac{dL_r(\mathbf{v})}{L_i(\mathbf{l})\cos\theta_i d\omega_i} \tag{2.10}$$

In Equation (2.10), $L_r(\mathbf{v})$ is the reflected radiance in the viewing direction $(\mathbf{v})$, $E_i(\mathbf{l})$ is the irradiance from the incident direction $(\mathbf{l})$, L_i is incident radiance (flux

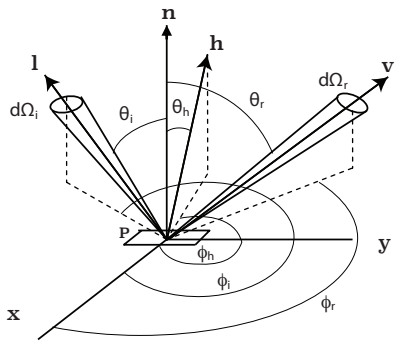

Figure 2.2: BRDF geometry [Image adapted from [37]].

per unit area, per unit solid angle (ω_i)), L_r is the reflected spectral radiance, d is the differential, and **v** and **l** are unit directional vectors. Inverse steradian [1/sr] is the unit of the BRDF. Figure 2.2 shows the geometry of the BRDF and the incoming and outgoing light directions. In Figure 2.2, the vectors **x**, **y** and **n** define a local reference frame where, **n** is the normal at point P on the surface, **x** is the tangent vector perpendicular to the normal **n**, and **y** is the bi-normal vector.

For BRDF to be physically valid, it is required to fulfill the following physical properties:

- non-negativity: for any combination of incident (**l**) and viewing (**v**) directions the BRDF (f_r) should be ≥ 0,
- Helmholtz reciprocity: incident (**l**) and viewing (**v**) directions should be reversible $f_r(\mathbf{l},\mathbf{v})$=$f_r(\mathbf{v},\mathbf{l})$
- Energy conservation: the amount of energy reflected from the surface is $\leq$ the incident energy.

Depending on the characteristics of the material surface, BRDF can be classified as **Isotropic BRDF** and **Anisotropic BRDF**. In **Isotropic BRDF**, reflection from the material surface remains unchanged with the rotation of the surface around direction vector **n**, whereas, in **Anisotropic BRDF** the reflection from the material surface changes with rotation of the surface around direction vector **n**.
For BRDF measurements, theoretically, the light is incident and reflected within an infinitesimally small solid angle. In practise, the light is incident and reflected within a finite solid angle resulting in an approximate measurement [42]. Relative measurements are therefore performed using a calibrated reference white standard material when calculating material BRDF [42].

2.2.2 Reflectance Measurement Setup

A reflectance measurement instrument typically comprises of a light source, to uniformly illuminate the material surface, and a detector, to measure the amount

of light reflected from the surface. To measure reflectance, CIE [15] recommended different sphere based and bidirectional single geometries to measure using a reflectance measurement instrument to measure the attribute "*colour*" in the *total appearance* as defined in [29]. Reflectance measured of an isotropic diffuse material using an instrument with one of these recommended geometries correlate well with how we perceive material appearance [15]. In print and packaging industry, instruments with $45°a : 0°$ and $0° : 45°a$ geometry are used to control printing process and quality evaluation for traditional light absorbing pigments printed on diffuse paper materials [43]. $d_i : 8°$ and $8° : d_i$ geometry instruments are used with the paint, textile and plastic industries. Using a single measurement geometry, however, is inadequate to measure and characterise print material produced using special effect pigments [11, 16–19].

Based on the optical properties of a material, ASTM recommended measurement geometries [20, 21] to perform multiple geometry measurements. When measuring different attributes of the visual appearance of a material, spectral changes in material surface reflectance define the colour, while directional changes (incident and viewing direction) define other attributes (like gloss, sparkle, etc) in many of the cases. For special effect coatings used in the packaging industry, directional changes also affect spectral reflectance of the material surface. ASTM-E179 [44] defines the terminology, measurement scales, and instrumentation for describing appearance attributes of reflective or transmissive materials. Change in appearance of a material as a function of change in incident and viewing direction is measured using instruments with several defined sets of measurement directions. Such instruments are termed as a multi-angle spectrophotometer, whereas when measured over a broad range of angles are termed as goniospectrophotometer [45].

As discussed in [42], the goniospectrophotometer can be classified into two types; scanning based instrument and image based instrument. The scanning instrument usually measures a ratio of the reflected to incident power (Φ_r/Φ_i) using a broadband illumination, as a light source, and a spectro-radiometer, as a detector. A radiometer records the spectral radiance at a material surface usually in the visible range of 400nm to 700nm in either 1nm, 5nm, or 10nm interval. Figure 2.3 shows a schematic diagram of a typical scanning based instrument. With the sample material to be measured lying flat, the detector and the light source or the sample material rotates when performing bidirectional reflectance measurements (different incident and viewing directions)[9, 47–51]. Measurements performed by a scanning based instrument are accurate but slow, as the geometrical and spectral calibration of the detector and light source or the material rotation stage contributes to the measurement time.

Image based instrument makes use of a camera as a detector to perform bidirectional reflectance measurements. Measurements are performed much faster compared to a scanning based instrument as an image based instrument captures the light reflected from the surface using camera images. The obtained measurements, however, can be less accurate compared to the scanning based measurements. Several image based measurement setups are presented and implemented

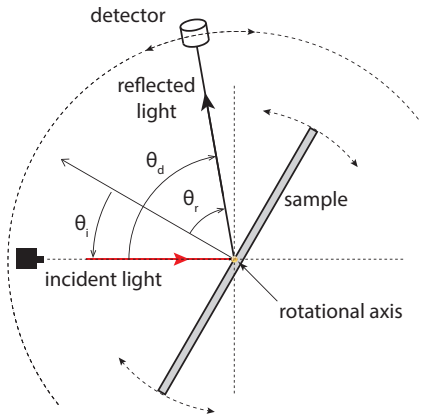

Figure 2.3: Schematic diagram of a gonio-spectrophotometer [Reprinted with permission of IS&T: The Society for Imaging Science and Technology sole copyright owners of the CIC20: Twentieth Color and Imaging Conference [46]].

to perform bidirectional reflectance measurement of different materials like human skin, material surface with varying optical properties (specularity), and velvet cloth material [23, 52–55].

A fast and accurate image based measurement setup presented in [24] measures the bidirectional reflectance of homogeneous materials including human skin. This setup used a hand-held digital camera (with a CCD sensor and RGB filters), as a detector, and a flashlight source, as illumination, to measure material surface with simple shapes like a sphere. Figure 2.4 shows the schematic diagram

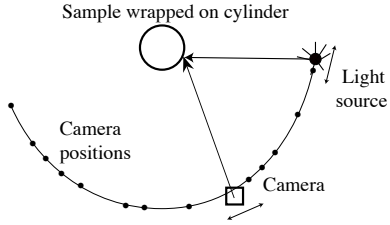

Figure 2.4: Schematic diagram of image based measurement setup similar to the one presented in [24].

of the setup similar to the one presented in [24]. A similar setup was used in [56] to create a bidirectional reflectance measurement database from 100 isotropic materials. Another setup presented in [55] measures anisotropic flat and flexible materials wrapped around a cylinder. The material to be measured is cut into strips and mounted on the cylinder with different orientations. The cylinder is

connected to a motor to perform measurements at different tilt angles. This setup can capture full four dimensional bidirectional reflectances of the material.

For a comprehensive review of different reflectance measurement setups refer [25].

2.3 BRDF Models and Representation

To represent a material BRDF, using an analytical model is one of the most compact ways [57]. Several BRDF models have been proposed to date. Guarnera *et al.* [25] presented an overview of BRDF models, proposed mainly within the computer graphics community, that represent the material surface reflectance properties.

BRDF models can be classified into analytical and data-driven models [57]. Analytical models can be further classified into physical and phenomenological models. Physical models take into account material surface roughness by using micro-facets with distribution in size and direction. Phenomenological models are approximations of reflectance data using measured data and fitting of the same using an analytical model. The data-driven model represents material BRDF as a dense set of measurements instead of using an analytical formula [56]. In Section 2.3.1 below, we present in brief the different analytical BRDF models used in the work carried out in this thesis.

A comprehensive review on BRDF models and representation can be referred at [25] and [57].

2.3.1 Analytical BRDF Models

Many analytical BRDF models also called as reflectance models have been proposed till now, especially within the computer graphics community. The Phong model [58] is one of the earliest models for non-lambertian surfaces based on the cosine law. The Phong model as shown in Equation (2.11) is an empirical model which is computationally efficient to analytically estimate reflectance properties of the material surface.

$$I_P = k_d \cos\theta_i + k_s \cos\theta_{mr}^{\alpha} \tag{2.11}$$

In Equation (2.11), I is the intensity at the point (P) on the material surface, θ_i is the angle between the incident light direction ($\mathbf{l}$) and the normal ($\mathbf{n}$) to the sample surface, θ_{mr} is the angle between the viewing direction ($\mathbf{v}$) and the mirror direction of the incident light direction ($\mathbf{l}$). k_d and k_s are the diffuse and specular Phong model parameters. The α parameter controls the shape of the specular reflection highlight. The Phong model does not follow the energy conservation and Helmholtz reciprocity properties of the BRDF and fails to estimate the material surface reflectance at grazing directions. However, it is a compact and computationally efficient model with just three parameters (seven in case the BRDF is estimated using camera RGB channels) to estimate surface reflectance properties for materials that show some roughness and specularity.

The Ward reflectance model [59] comes under the category of phenomenological model and was designed to fit bidirectional reflectance measurements. It uses a gaussian distribution to represent the specular peak and can be used to estimate isotropic and anisotropic material BRDF. The Ward model does not follow the energy conservation property of the BRDF at grazing angles. In the isotropic Ward model presented in Equation (2.12), k_d is the diffuse reflectance parameter, k_s parameter controls the magnitude of the specular reflectance, α controls the width of the specular reflectance lobe and $4\pi\alpha^2$ is a normalisation factor. Referring Figure 2.2, at a point (P) on material surface, θ_i is the angle between the incident light direction (**l**) and the normal (**n**), θ_r is the angle between the viewing direction (**v**) and the normal (**n**). θ_h is the angle between the halfway vector (**h**) and the normal (**n**).

$$f_r(\mathbf{l},\mathbf{v}) = \frac{k_d}{\pi} + \frac{k_s}{\sqrt{\cos\theta_i \cos\theta_r}} \cdot \frac{e^{-\tan^2(\theta_h/\alpha^2)}}{4\pi\alpha^2} \tag{2.12}$$

In the anisotropic Ward model, two parameters α_x and α_y are used to control the width of the specular reflectance lobe in the two principal anisotropy directions. Anisotropic Ward model is defined as in Equation (2.13).

$$f_r(\mathbf{l},\mathbf{v}) = \frac{k_d}{\pi} + \frac{k_s}{\sqrt{\cos\theta_i \cos\theta_r}} \cdot \frac{e^{-\tan^2(\theta_h)\left(\cos^2\theta_h/\alpha_x^2 + \sin^2\theta_h/\alpha_y^2\right)}}{4\pi\alpha_x\alpha_y} \tag{2.13}$$

The Lafortune model [60], is a flexible empirical model that is generalised using cosine lobe based models similar to the Phong model. It follows the Helmholtz reciprocity and energy conservation properties of the BRDF. Due to the weighted dot product, the Lafortune model shows an increased flexibility compared to the Ward model, is computationally efficient and is able to fit complex material reflectances. It is generalised using a 3×3 matrix in which the direction vectors are defined in a fixed local co-ordinate system with respect to the surface normal (**n**). The model presented in Equation (2.14) is one of the simplest forms of the lafortune model to use. C_x, C_y, C_z and α_l control the shape and orientation of the specular reflectance lobe. Retro-reflection and anisotropy can be controlled by setting C_x, C_y, C_z as positive and $C_x \neq C_y$ respectively. $l_{x,y,z}$ and $v_{x,y,z}$ are direction components of the incident (**l**) and viewing (**v**) direction vectors.

$$f_r(\mathbf{l},\mathbf{v}) = \frac{k_d}{\pi} + k_s\left[C_x l_x v_x + C_y l_y v_y + C_z l_z v_z\right]^{\alpha_l} \tag{2.14}$$

Under the physically based BRDF models, Cook-Torrance (CT) [61] model is widely used especially in computer graphics. CT model uses the micro-facet theory and the halfway vector (**h**) to calculate the specular reflectance lobe and the diffuse reflectance is lambertian [25]. CT model does not follow the energy conservation property of the BRDF. It can be defined mathematically as shown in Equation (2.15).

$$f_r(\mathbf{l},\mathbf{v}) = k_d + k_s \frac{FDG}{\pi \cos\theta_i \cos\theta_r} \tag{2.15}$$

In Equation (2.15), F is the Fresnel term that calculates the amount of incident light reflecting and transmitting from material surface. G is the geometrical attenuation factor that accounts for the masking and self-shadowing effect depending on the micro-facet projected area. D is the Beckmann distribution that defines the micro-facet distribution in terms of size and direction. F, G and D are defined mathematically in Equation (2.16), Equation (2.17), and Equation (2.18).

$$F = \frac{(g-c)^2}{2(g+c)^2}\left\{1+\frac{[c(g+c)-1]^2}{[c(g-c)+1]^2}\right\} \tag{2.16}$$

$$G = \min\left\{1, \frac{2(\mathbf{n}\cdot\mathbf{h})(\mathbf{n}\cdot\mathbf{v})}{(\mathbf{v}\cdot\mathbf{h})}, \frac{2(\mathbf{n}\cdot\mathbf{h})(\mathbf{n}\cdot\mathbf{l})}{(\mathbf{v}\cdot\mathbf{h})}\right\} \tag{2.17}$$

$$D = \frac{1}{m^2\cos^4(\theta_h)} e^{-\left[\frac{(\tan(\theta_h))}{m}\right]^2} \tag{2.18}$$

In Equation (2.16), $c = \mathbf{v}\cdot\mathbf{h}$, $g = \eta^2 + c^2 - 1$ and η is the index of refraction. In Equation (2.18), m is the roughness parameter and θ_h is the angle between the halfway vector ($\mathbf{h}$) and the normal ($\mathbf{n}$).

Another physically based BRDF model used in the work carried out in this thesis is the micro-facet ABC model defined in [62] and given in Equation (2.19). Löw *et al.* [62] presented two isotropic BRDF models based on Rayleigh-Rice light scattering theory and the micro-facet theory to render glossy surfaces. Both the models are the modified version of the ABC model presented in [63, 64]. The micro-facet ABC model is based on the CT model and uses the geometrical attenuation (G) and Fresnel factor (F) as defined in [61] and given in Equation (2.16) and Equation (2.17).

$$f_r(\mathbf{l},\mathbf{v}) = \frac{k_d}{\pi} + \frac{S(\sqrt{1-(\mathbf{n}\cdot\mathbf{h})}F(\theta_h)G(\mathbf{n}\cdot\mathbf{l},\mathbf{n}\cdot\mathbf{v})}{(\mathbf{n}\cdot\mathbf{l})(\mathbf{n}\cdot\mathbf{v})} \tag{2.19}$$

In Equation (2.19), S is the micro-facet distribution based on the ABC model from [63, 64].

$$S(\Psi) = \frac{A}{(1+B\Psi^2)^C}, \tag{2.20}$$

Equation (2.20) is a non-normalised distribution. B and C control the width of specular reflectance peak and the fall-off rate of wide-angle scattering respectively. A is used as the specular reflectance parameter. Ψ is defined as $\sqrt{\Psi_x^2+\Psi_y^2}$ where, $\Psi_x = (\sin\theta_r\cos\phi_r - \sin\theta_i)/\lambda$ and $\Psi_y = (\sin\theta_r\sin\phi_r)/\lambda$. λ is the wavelength of the incident light. The ABC model follows the Helmholtz reciprocity BRDF property but not the energy conservation property.

Several flexible BRDF models have been introduced to date to model material appearance. Some of the models (Phong model, Ward reflectance model, and CT) presented above are well-established models and are very much in use due to computational simplicity and ease of optimisation with a limited number of model

parameters. Lafortune reflectance model and ABC reflectance model are flexible with more number of optimisation parameters and can provide accurate fits to the measured BRDF data but can be computationally complex.

This chapter covered the background relevant to the work carried out as part of this thesis. Next, in Chapter 3, we summarise the work done in this thesis.

Chapter 3

Summary and Contribution of Included Papers

Chapter 3 gives an overview of the research carried out in this thesis and how the included papers contribute to the main objective. The overall objective of this thesis is to investigate the applicability of using the measurement setup to measure and represent BRDF of flexible and homogeneous packaging print materials with complex optical properties. The research carried out contributes to the two parts, **Imaging and Instrumentation** and **BRDF measurement and representation** and address the research questions (**RQ1** - **RQ6**) presented in Section 1.2. Outcome of the research work carried out is published in different conferences and journals. The relation between the included papers is demonstrated in Figure 3.1. **Paper I** [1], **Paper II** [2], and **Paper III** [3] contribute towards **Imaging and Instrumentation** part and address research questions **RQ1 - RQ3**. **Paper IV** [4], **Paper V** [5], and **Paper VI** [6] address research questions **RQ1**, **RQ3 - RQ4** while **Paper VII** [7] works towards answering research questions **RQ4 - RQ6**. All the four papers contribute towards **BRDF measurement and representation** part in the thesis. In Figure 3.1, included papers coloured in blue are published in conference proceedings, whereas, included papers in green are published as journal articles. Work carried out in **Paper VIII** [8] and **Paper IX** [9] strongly relates to the thesis topic and objectives. These two papers are therefore listed as related papers in this thesis.

3.1 Imaging and Instrumentation

In this section we present the work carried out to implement the measurement setup and calculate its measurement accuracy when performing bidirectional reflectance measurements of flexible, homogeneous packaging print materials. Section 3.1 address the research questions **RQ1**, **RQ2**, and **RQ3** set out in Section 1.2. We divide this section in two parts as,

- Measurement setup
- Accuracy of the measurement setup

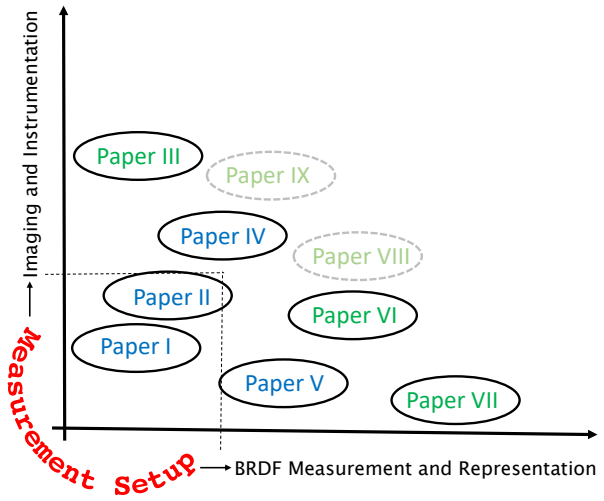

Figure 3.1: Diagram demonstrating the included papers and their contribution towards the thesis objective.

3.1.1 Measurement Setup

Figure 3.2 shows the schematic diagram of the measurement setup that has been used to perform fast bidirectional reflectance measurements of a flexible, homogeneous packaging print materials. The materials show different reflectance properties that range from diffuse to non-diffuse and gonio-chromatic. The measurement setup uses an uniform point light source to illuminate a homogeneous flexible material sample that is curved onto a cylinder of known radius. We use a film projector, consisting of a halogen tungsten lamp, as a point light source with a spectral power distribution as shown in Figure 3.3. As the film projector uses focusing lens, the origin of the point light source was calculated using inverse square law (calculation details can be referred in **Paper III** [3]). A commercially available digital camera is used as a detector. Figure 3.4 shows the measurement setup using a DLSR camera as a detector and a film projector as a point light source. The light source and the detector is at a fixed position from the sample. The point light source illuminates the sample from a fixed direction (in range of $\theta^\circ < \theta_L < 90^\circ$) at a known distance ($d_L$). With the measurement setup in a vector plane, incident (θ_i) and viewing (θ_r) direction at point P can be calculated as shown in Equation (3.1).

$$\cos\theta_i = \frac{\mathbf{P_L}\cdot\mathbf{n}}{|P_L|}, \quad \cos\theta_r = \frac{\mathbf{P_C}\cdot\mathbf{n}}{|P_C|} \tag{3.1}$$

Every point P on the curved material surface makes a corresponding incident (θ_i) and viewing (θ_r) direction with respect to the normal ($\mathbf{n}$) at point P thus measuring the bidirectional reflectance information. When measuring with a digital

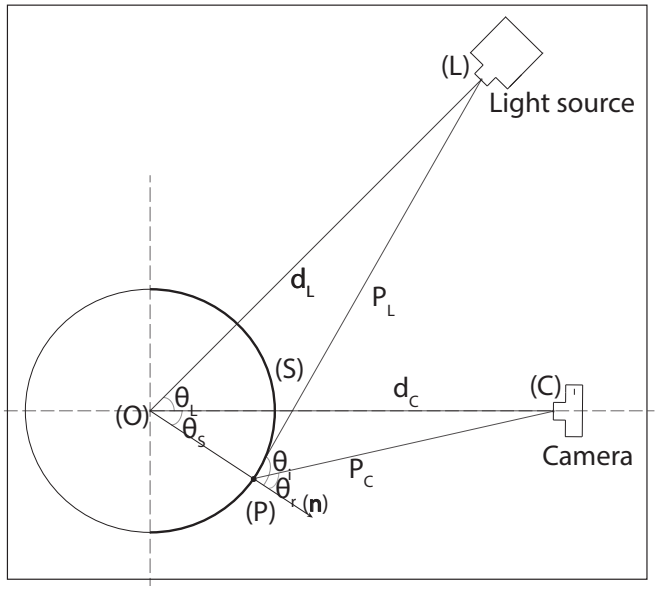

Figure 3.2: Schematic diagram of the measurement setup.

camera as a detector, each pixel in the captured image corresponds to a point (P) on the curved sample surface. **Paper I** [1] presents the measurement setup, incident (θ_i) and viewing (θ_r) direction estimation and validation.

A monochrome CCD camera or a commercially available digital colour (RGB) camera can be used as a detector in the measurement setup. Image captured by a digital colour camera records the light information in digital values for each camera sensor. In order to calculate material BRDF using the obtained measurements and compare them with a gonio-spectrophotometer, spectral sensitivity of the camera sensor should be known. **Paper II** [2] presents the work carried out to measure camera spectral sensitivities ($r(\lambda)$, $g(\lambda)$, $b(\lambda)$) of a Nikon D200 DSLR camera that is used as a detector in the measurement setup. Figure 3.5 shows the camera spectral sensitivities obtained using the monochromator and the telespectroradiometer. A 3×3 conversion matrix $\hat{M}$ was calculated using the CIE 2° colour matching functions ($\bar{x}, \bar{y}, \bar{z}$) [65] and the obtained camera spectral sensitivities. The bidirectional reflectance measurements performed using the measurement setup can then be converted into a colorimetric space (CIEXYZ) using $\hat{M}$. The measured camera spectral sensitivities and the calculated $\hat{M}$ were evaluated using a standard ColourChecker test chart.

3.1.2 Measurement Setup Accuracy

The measurement setup presented in Section 3.1.1 can perform fast bidirectional measurements of flexible, homogeneous packaging materials like printed pack-

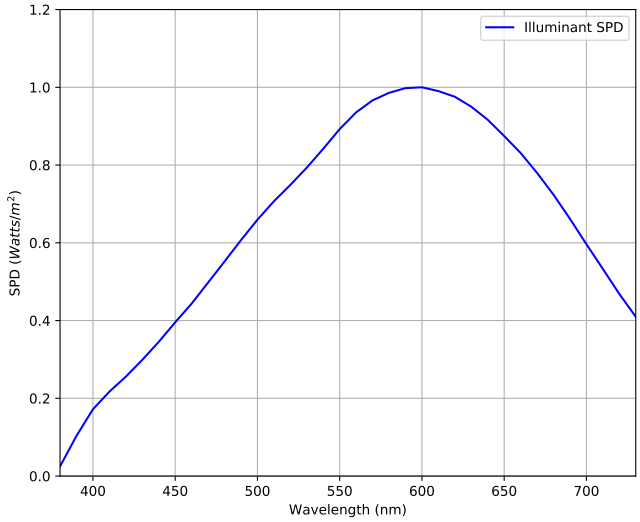

Figure 3.3: Spectral power distribution of the point light source used in the measurement setup.

aging paper material with different reflectance properties. Accuracy of the measurement setup to perform bidirectional reflectance measurements is investigated using propagation-of-error analysis. The measurements obtained using the measurement setup were compared with measurements from two commercially available gonio-spectrophotometers by converting them into a common domain. **Paper III** [3] presents the work carried out in calculating the measurement setup accuracy when performing bidirectional reflectance measurements. Four different flexible, homogeneous, and isotropic packaging print samples, *LightCyan*, *LightMagenta*, *Cyan* and *Magenta*, produced using matt coated paper and wax-based inks are measured using the measurement setup and two commercially available gonio-spectrophotometers. Spectral bidirectional reflectance is measured by both the gonio-spectrophotometers. The measurement setup recorded a 16-bit raw RGB image using the Nikon D200 DSLR camera as a detector. To compare measurements obtained using the measurement setup and the gonio spectrophotometers, the spectral BRDF measurements are converted to camera RGB values using the camera spectral sensitivity functions of the Nikon D200 DSLR camera (measured in **Paper II** [2]), spectralon reference white tile (ST) measured using one of the two gonio-spectrophotometers used in the comparison and a tele spectroradiometer as a detector in the measurement setup.

We identify two main sources of error when performing bidirectional reflectance measurements using the measurement setup:

- **Geometrical error**: uncertainty in estimating the incident (θ_i) and viewing (θ_r) directions,

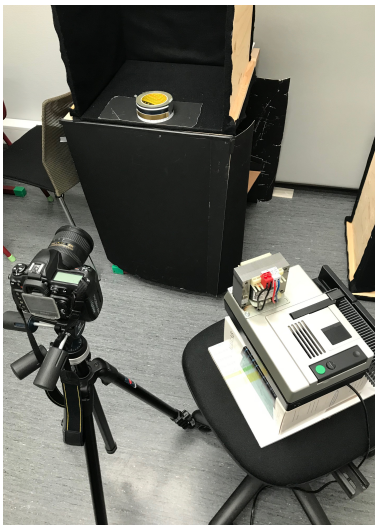

(a) Top view 1

(b) Top view 2

(c) Side view

Figure 3.4: Measurement setup using a DSLR camera as a detector, a film projector as a point light source and the measurement sample wrapped around a cylinder of the known radius.

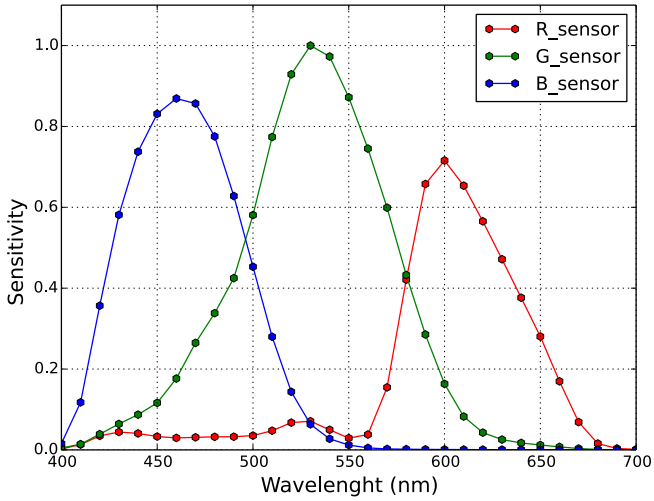

Figure 3.5: Sensor sensitivity functions of the camera used as a detector in the measurement setup [Reprinted with permission of IS&T: The Society for Imaging Science and Technology sole copyright owners of Electronic Imaging: Measuring, Modeling and Reproducing Material Appearance 2016] (**Paper II** [2]).

- **Matrix error**: error is calculating the conversion matrix $\hat{M}$ using the camera spectral sensitivities measured using a monochromator.

Geometrical Error

Error uncertainty (Δ) in estimating the incident (θ_i) and viewing (θ_r) direction is derived using the procedure given by the Joint Committee for Guides in Metrology (JCGM) [66]. The uncertainty in performing physical measurements (d_L, d_C, R, θ_L, and d_p) in the measurement setup in order to estimate the incident (θ_i) and viewing (θ_r) direction is approximated. Table 3.1 shows the derived and approximated uncertainty in estimating the incident (θ_i) and viewing (θ_r) directions.

Matrix Error

To estimate the error introduced by $\hat{M}$ calculations (using the camera spectral sensitivities), CIE Y was calculated using,

- $\hat{M}$ and the RGB values obtained using the radiance at the sample surface and spectral sensitivities of the Nikon D200 camera used as a detector in the measurement setup ($Y_{(\hat{M}-RGB)}$),

Table 3.1: Measurement uncertainty in the measurement setup parameters (from **Paper III**) (adapted with permission from [3]).

	Setup parameters	Uncertainty
Calculated	θ_i	±7.6°
	θ_r	±7.4°
	θ_S	±6.7°
	F_P	±1973 pixels
Approximated	R	±5 mm
	d_C	±10 mm
	d_p	±5 pixels
	d_L	±20 mm
	θ_L	±4°

- radiance at the sample surface and the CIE 2° colour matching functions ($Y_{(L_r-CIE2^\circ)}$).

The error, ΔY, is calculated relative to the CIE 2° colour matching functions using Equation (3.2).

$$\Delta Y = \frac{\sqrt{(Y_{(\hat{M}-RGB)} - Y_{(L_r-CIE2^\circ)})^2}}{Y_{(L_r-CIE2^\circ)}} \tag{3.2}$$

Table 3.2 shows the error in the CIE Y estimation in the packaging print materials, *LightCyan*, *LightMagenta*, *Cyan* and *Magenta* measured using the measurement setup. Materials *LightCyan* and *LightMagenta* showed diffuse reflectance properties whereas materials *Cyan* and *Magenta* show some specularity but overall were diffuse. Reflectance properties of the packaging print material that is measured using the measurement setup and the gonio-spectrophotometers are discussed briefly in Section 3.2. The measurement setup was evaluated by analysing the

Table 3.2: Error (ΔY) in CIE Y calculation (from **Paper III**) (adapted with permission from [3]).

Sample	*LightCyan*	*LightMagenta*	*Cyan*	*Magenta*
ΔY	0.11	0.12	0.18	0.13

CIE Y value estimated using the measurements obtained from the measurement setup and the gonio-spectrophotometers. Figure 3.6 shows a flow diagram of the steps followed to estimate CIE Y value from the obtained measurements. Relative error ($Error_{\Delta Y}$) is calculated using Equation (3.3) and shown in Table 3.3 for each sample using the CIE Y value estimated from the gonio-spectrophotometer (Y_{Gonio}) and the measurement setup (Y_{Setup}) measurements.

$$Error_{\Delta Y} = \frac{\sqrt{(Y_{Gonio} - Y_{Setup})^2}}{Y_{Gonio}} \tag{3.3}$$

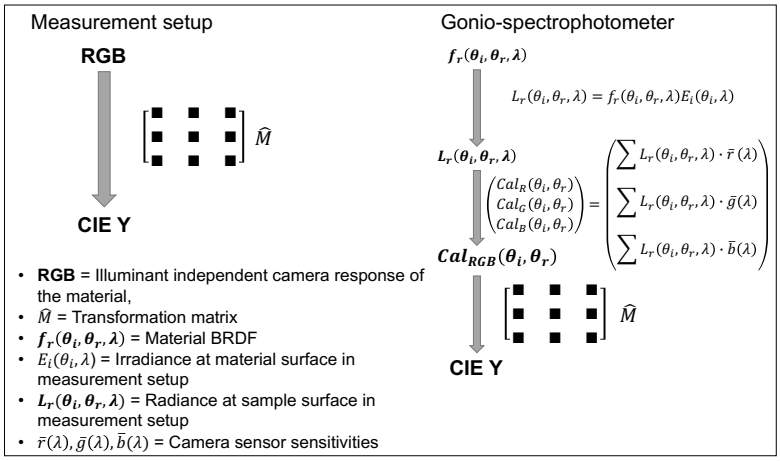

Figure 3.6: CIE Y value estimation using the measurements obtained from the measurement setup and the gonio-spectrophotometer.

Table 3.3: Average $Error_{\Delta Y}$ between CIE Y calculated using measurements obtained from the measurement setup and the gonio-spectrophotometer (from **Paper III**) (adapted with permission from [3]).

Gonio-spectrophotometer	*LightCyan*	*LightMagenta*	*Cyan*	*Magenta*
LAMBDA1050	0.14	0.05	-NM-	-NM-
GCMS	-NM-	-NM-	0.24	0.21

-NM- = could not measured

3.1.3 Summary

We summarised the work carried out in **Paper I** [1], **Paper II** [2], and **Paper III** [3] that address research questions **RQ1**, **RQ2**, and **RQ3** from Section 1.2 and contribute towards the **Imaging and Instrumentation** part of the thesis.

We presented the measurement setup (**Paper I** [1], **Paper II** [2]), and investigated the accuracy of the measurement setup (**Paper III** [3]) by comparing the bidirectional measurements obtained using the measurement setup and two commercially available gonio-spectrophotometers. Uncertainty in calculating the incident (θ_i) and viewing (θ_r) directions and the conversion matrix $\hat{M}$ (using the camera spectral sensitivities) was estimated.

3.2 BRDF Measurement and Representation

To investigate the suitability of using the measurement setup for bidirectional reflectance measurement and material BRDF estimation, we measured packaging print materials with reflectance properties varying from diffuse to non-diffuse and

(a) Spectralon tile (white reference).

(b) *LightCyan* and *LightMagenta* material (diffuse reflectance).

(c) Print materials with diffuse and non-diffuse reflectance properties.

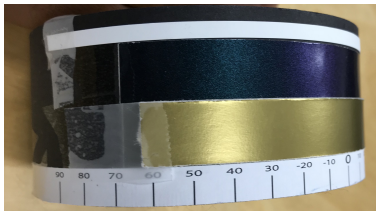

(d) *Gold* and *BlueGreen* material (non-diffuse and gonio-chromatic reflectance).

Figure 3.7: Print materials with different reflectance properties measured using the measurement setup, LAMBDA1050, and GCMS. Figures 3.7b and 3.7c reprinted with permission of IS&T: The Society for Imaging Science and Technology sole copyright owners of Electronic Imaging: Measuring, Modeling and Reproducing Material Appearance 2016 and of Electronic Imaging: Material Appearance 2017 respectively. [Images adapted from **Paper II** [2], **Paper V** [5], and **Paper VI** [6]].

Gonio-chromatic. This section addresses research questions **RQ1**, and **RQ3 - RQ6** by estimating material BRDF using different analytical reflectance models and measurement datasets obtained using the measurement setup and commercial gonio-spectrophotometers. Non-diffuse and Gonio-chromatic reflectance properties are visualised using BRDF estimated with optimal measurement data set. We divide this section into three parts as,

- Measurement samples
- Bidirectional reflectance measurement and BRDF estimation
- BRDF representation

3.2.1 Measurement Samples

The packaging materials that are used as measurement samples in this thesis are chosen based on their surface properties like homogeneity, flexibility, and reflectance. The measurement samples used are homogeneous, flexible and show surface reflectance properties from diffuse to non-diffuse and Gonio-chromatic. Another important criterion was the easy access to the samples for measurements using the measurement setup and the gonio-spectrophotometers. Access to gonio-

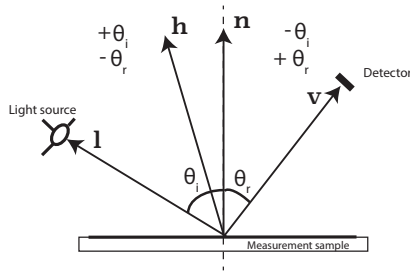

Figure 3.8: Angular sign convention followed in bidirectional measurements using the measurement setup and the two gonio-spectrophotometers.

spectrophotometers, as a reference measurement instrument, and the measurement sample (*BlueGreen* material) with Gonio-chromatic reflectance properties has been a challenge in this thesis.

In total 11 print materials, as shown in Figure 3.7, were measured using the measurement setup. Due to limited access, eight out of the 11 print materials were measured using two commercially available gonio-spectrophotometers. The two gonio-spectrophotometers are herein referred to as LAMBDA1050 and GCMS. Both the instruments perform in-plane measurements ($\phi_i = \phi_r = 0°$). For details and specifications of the LAMBDA1050 and the GCMS instruments, the reader is requested to refer PerkinElmer's LAMBDA1050 manual[1] and Murakami's GCMS-3B Goniospectrophotometric Color Measurement System manual[2] respectively.

Due to limited access to the gonio-spectrophotometers, two print materials *LightCyan* and *LightMagenta* along with the spectralon white reference tile (Figure 3.7a and Figure 3.7b) were measured using only LAMBDA1050. *BlueGreen*, *Gold*, (refer Figure 3.7d), *Red*, *MunsellWhite*, *Cyan*, and *Magenta* (refer Figure 3.7c) were measured using the GCMS instrument. The incident (θ_i) and viewing (θ_r) direction are as defined in Figure 2.2 and follow the sign convention as shown in Figure 3.8. Figure 3.9 shows the radiance factor measurements performed using the two gonio-spectrophotomters. Reflectance properties vary from diffuse to non-diffuse and also gonio-chromatic for the *BlueGreen* material (refer Figure 3.10).

Materials *LightCyan* and *LightMagenta* are 100% ink patches of the light cyan and light magenta ink printed on matt coated paper using the HP DesignJet Z3200-ps plotter. Materials *Cyan*, *Magenta* are 100% ink patches printed on matt coated paper using the Océ ColorWave 600 plotter. *Red*, *Pantone10309C*, *Pantone10213C*, *Pantone10153C* are produced using the process inks in the Océ ColorWave 600 plotter. *Gold* material is a metallic gold thin cardboard commonly used for dec-

[1]Lambda 1050 uv/vis/nir spectrophotometer, `http://www.perkinelmer.com/product/lambda-1050-uv-vis-nir-spectrophotometer-l1050?searchTerm=L1050&pushBackUrl=?searchName=L1050`. Accessed:2019-08-23.

[2]Gcms-3 goniospectrophotometer system, `http://www.aviangroupusa.com/pdf/GCMS3_Des.pdf`. Accessed: 2019-08-23

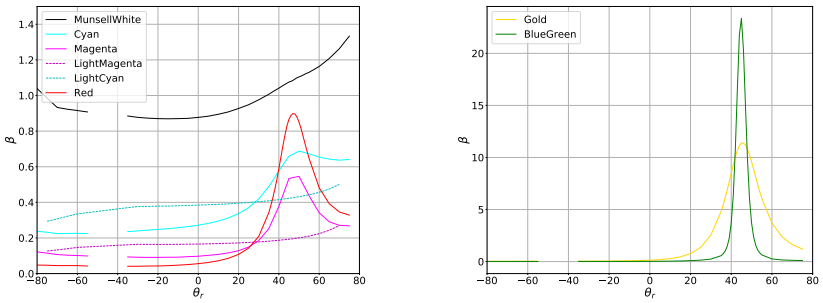

Figure 3.9: Print materials with different reflectance properties from diffuse to non-diffuse. Spectral radiance factor (β) measured at 560nm, $\theta_i = -45°$ and θ_r in the range of $-80°$ to $80°$.

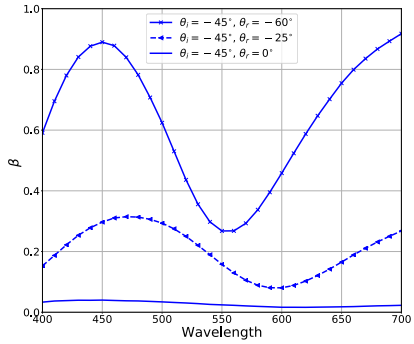

Figure 3.10: Gonio-chromatic reflectance of the *BlueGreen* print material [Image adapted from **Paper VI** [6]. Spectral shift obtained with change in the viewing (θ_r) direction.

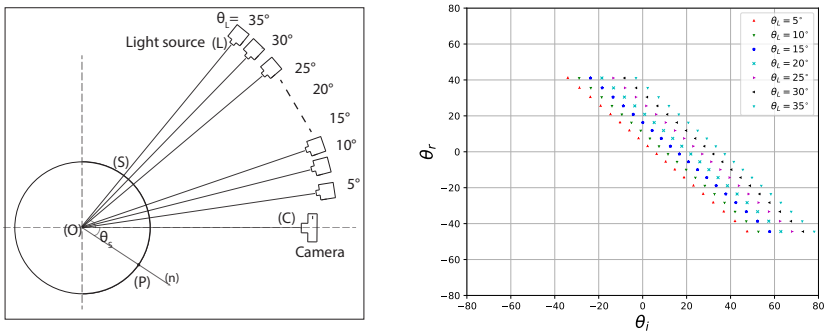

Figure 3.11: Schematic diagram of the measurement setup with multiple illumination directions (θ_L) and the obtained incident (θ_i) and viewing (θ_r) directions.

orative purposes in the packaging industry. *BlueGreen* material is produced using effect pigments and varnish coating on paper using conventional printing techniques. Along with these materials a Munsell White N9/ sheet (*MW*) produced according to ANSI standards was measured using the measurement setup and the GCMS instrument.

3.2.2 Bidirectional Reflectance Measurement and BRDF Estimation

To analytically estimate material BRDF, reflectance model parameters are optimised using a cost function and the bidirectional reflectance measurements of the print material obtained using the measurement setup.

As presented in Section 3.1.1, the measurement setup uses a tungsten point light source to illuminate the measurement sample curved onto a cylinder and a DSLR camera as a detector. The camera captures a 16-bit raw RGB image that digitally records the radiance exited from the curved measurement sample surface. Each pixel in the captured image corresponds to a point (P) on the curved sample surface with a unique incident (θ_i) and viewing (θ_r) direction combination with respect to the normal ($\mathbf{n}$) at surface point P. Illuminating the measurement sample at several illumination directions (θ_L) should help perform many measurements. Figure 3.11 shows a schematic of the measurement setup with multiple illumination directions (θ_L) and the obtained incident (θ_i) and viewing (θ_r) directions. Figure 3.12 shows the radiance exited from the *Red* material surface and measured using the measurement setup. As the measurement samples are curved onto a cylinder, for highly non-diffuse materials, a single exposure image captured by a digital camera may not capture the complete dynamic range. This was the case when measuring the *Gold* and the *BlueGreen* print materials using the measurement setup (**Paper VI** [6]). Both the materials are non-diffuse and show very high specularity (refer Figure 3.7). Multiple exposure captures are therefore required to record the full dynamic range of such highly non-diffuse materials. A high dynamic range (HDR) image (a radiance map) can be further generated from these

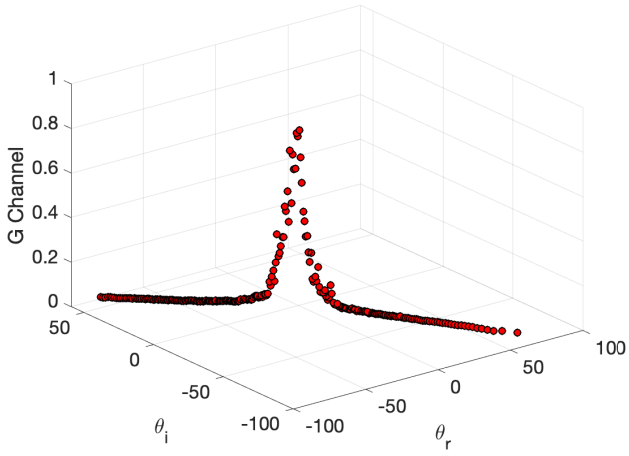

Figure 3.12: *Red* material measured using the measurement setup by wrapping around a cylinder, illuminating at $\theta_L = 20°$ and measuring using a Nikon D200 DSLR camera.

multiple exposure images. We used the Debevec and Malik's [67] algorithm to calculate a HDR image for the *Gold* and *BlueGreen* sample measured using the measurement setup at multiple exposures (**Paper VI** [6]). The algorithm gives a radiance map as an output which can further be tone mapped for visualisation using a tone mapping algorithm of your choice.

The bidirectional measurements obtained from the measurement setup can be further used to optimise reflectance model parameters using a cost function. As discussed in Section 2.3.1, several analytical reflectance models have been proposed till now to estimate material BRDF. The choice of the reflectance model to use will depend on the material surface properties, model parameters to be optimised and computational complexity [25, 57]. Reflectance model parameters control how the incident light is reflected from the material surface (diffuse reflection, specular reflection, intensity and width of the specular lobe, direction, etc). No single generalised reflectance model exists that can estimate BRDF of a wide range of materials with different surface reflectance properties [25].

The *LightCyan* and *LightMagenta* print materials were measured using the measurement setup and modelled using the Phong model [58]. As both the samples showed diffuse reflectance properties, it was believed that a simple cosine lobe based Phong model should be sufficient to successfully estimate material BRDF. Both the materials were measured at three illumination directions (θ_L) with a single exposure captured using the Nikon D200 DSLR camera as a detector. In **Paper IV** [4], we normalised the measurements using the spectralon tile measurements recorded at approximately $\theta_r = 0°$. Phong model parameters were optimised using the normalised measurements and root mean square (RMS) error

as a cost function. Nelder-Mead downhill simplex algorithm [68] was used for the optimisation. In **Paper II** [2], we converted the measurements into CIEXYZ colorimetric space using the conversion matrix $\hat{M}$. The Phong model parameters were optimised using the measurements in the CIEXYZ colorimetric space and a euclidean error as a cost function. Figure 3.13 shows the *LightCyan* and *LightMagenta* material measured with the measurement setup and estimated using the Phong model in the CIEXYZ colorimetric space.

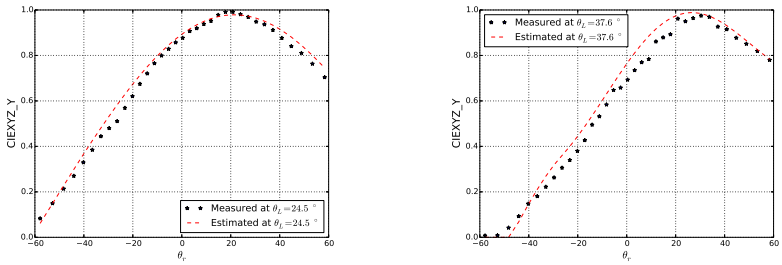

(a) *LightCyan* material **(b)** *LightMagenta* material

Figure 3.13: *LightCyan* and *LightMagenta* material measured using measurement setup and estimated using the Phong model [Images adapted from **Paper II [2]].**

In **Paper V** [5], seven packaging print materials (refer Figure 3.7c) having diffuse and non-diffuse reflection properties were measured bidirectionally using the measurement setup. Material BRDF of these samples were estimated using two reflectance models, CT [61] and isotropic Ward reflectance model (Ward) [59], presented in Section 2.3.1. Parameters of both the reflectance models were optimised using the measurements, in the CIEXYZ colorimetric space, and the CIEΔ_{00} [15] colorimetric difference as a cost function. To evaluate the measurement setup against physical measurements, one of the print material, *Cyan*, was measured using a tele-spectro radiometer in four viewing (θ_r) directions. It was illuminated at $\theta_i = 40°$. Figure 3.14 shows the obtained results in terms of estimated BRDF of the *Cyan* material and comparison against the tele-spectroradiometer measurements.

The *Gold* and *BlueGreen* materials are highly non-diffuse compared to the other samples measured using the measurement setup. In **Paper VI** [6]], both the materials were measured at multiple exposures to record the full dynamic range. Along with these highly non-diffuse materials, a fairly diffuse material, *Red*, was measured using a single exposure image.

Following the definition of β given in Equation (2.9) and discussions in [69], BRDF of both the materials were calculated in terms of β using Equation (3.4). *MW* material was used as a perfect reflecting diffuser (*PRD*) when calculating β for the *Gold* and *BlueGreen* materials using Equation (3.4).

$$\beta(\theta_i, \phi_i, \theta_r, \phi_r, \lambda) = \frac{L_r(\theta_i, \phi_i, \theta_r, \phi_r, \lambda)}{L_r^{PRD}(\theta_i, \phi_i, \theta_r, \phi_r, \lambda)} \tag{3.4}$$

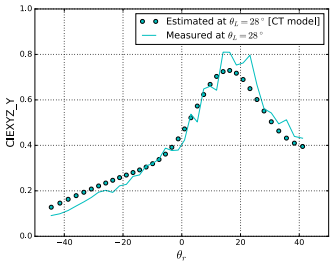

(a) CIEXYZ Y value measured using the measurement setup and estimated using CT model.

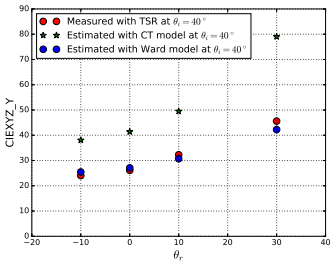

(b) CIEXYZ Y value measured using telespectro radiometer and estimated using CT and Ward reflectance model.

Figure 3.14: *Cyan* material measured and estimated using the reflectance models [Images adapted from **Paper V** [5]].

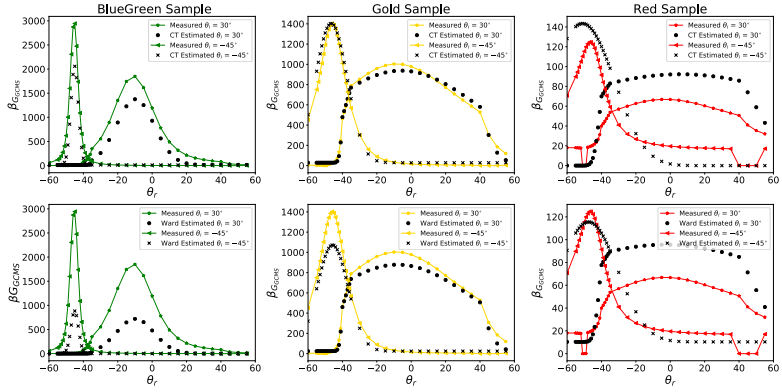

Figure 3.15: Material BRDF (G-channel) measured using GCMS instrument and estimated using the optimised reflectance model parameters of the CT and Ward model [Image adapted from **Paper VI** [6]].

To investigate the suitability of using the measurement setup to measure such highly non-diffuse and gonio-chromatic packaging print materials, the measurements were compared against the GCMS measurements. Measurement performed by GCMS have different dimensions compared to the measurements performed by the measurement setup. For comparison, the measurements obtained from both the instruments were converted to a common domain (cameraRGB).

Material BRDF was estimated in the cameraRGB domain by optimising the CT and Ward model parameters using the measurements obtained from the measurement setup and RMS error as a cost function. Figure 3.15 shows the measured (using the GCMS) and estimated (using the optimised reflectance model parameters) BRDF ($\beta_{RGB_{GCMS}}$) of the three packaging materials.

When measuring using the measurement setup we have used a number of illumination directions (θ_L) which adds to the measurement time and complexity. Obtaining an optimal measurement data set to estimate material BRDF would help reduce the measurement time and complexity. CT and Ward model parameters were optimised using measurements collected with different combinations of the illumination directions (θ_L). To evaluate the performance, a relative error was calculated using Equation (3.5), between the measured ($\beta_{P_{mea}}$) and estimated ($\beta_{P_{est}}$) material BRDF. Figure 3.16 shows box-and-whisker plots for the relative error (ΔErr_P) calculated using Equation (3.5).

$$\Delta Err_P = \frac{\sum_p \mid \beta_{P_{mea}} - \beta_{P_{est}} \mid}{\sum_p \beta_{P_{mea}}} \tag{3.5}$$

To colorimetrically evaluate the performance, CIE1976 $u^{'}v^{'}$ uniform chromaticity

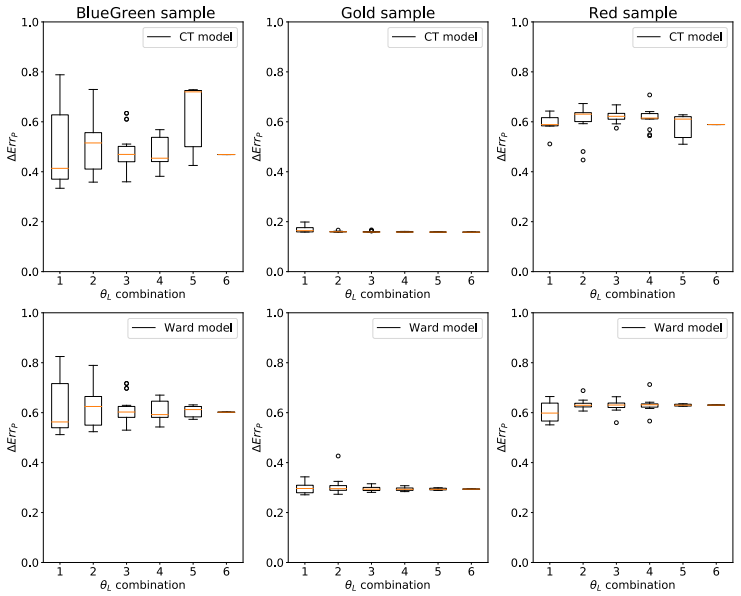

Figure 3.16: Box-and-whisker plots of the relative error (ΔErr_P) between measured and estimate material BRDF (G-channel) using the optimised reflectance model parameters [Image adapted from **Paper VI** [6]].

co-ordinates [15] were calculated from the measured and estimate BRDF. Matrix $\hat{M}$ was used to convert the measurements to the CIEXYZ colorimetric space. CIEXYZ values were further converted to chromaticity coordinates CIE1976 $u^{'}v^{'}$ [15]. Figure 3.17 shows the measured and estimate BRDF in the CIE1976 $u^{'}v^{'}$ uniform chromaticity co-ordinate [15] space. Colorimetrically, both the reflectance models struggled to estimate BRDF of the BlueGreen sample. Packaging print materials with non-diffuse and gonio-chromatic reflectance could be measured using

the measurement setup but with a noticeable error (**Paper VI**) [6]. Based on the obtained results, we learn that to estimate BRDF of materials similar to the ones measured in **Paper VI** [6] (*Gold* and *BlueGreen*) require measurements that are obtained using the measurement setup at a minimum of two illumination directions (θ_L), reflectance models with more free parameters (to better control the complex reflectance properties), and an optimisation algorithm not converging to local minimum.

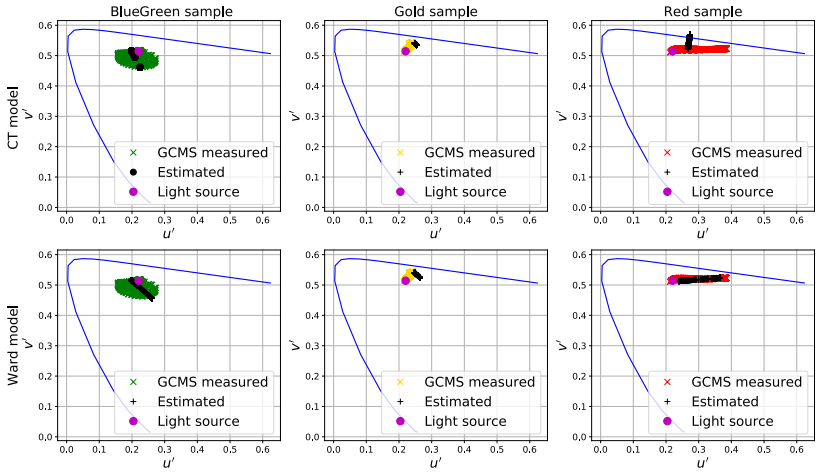

Figure 3.17: CIE1976 $u'v'$ uniform chromaticity co-ordinates calculated using the measured (using GCMS instrument) and estimated (using the reflectance model parameters of the CT and Ward model optimised using the measurement setup measurements) BRDF. [Image adapted from **Paper VI** [6]].

3.2.3 BRDF Representation

To successfully estimate BRDF of packaging materials with complex reflectance properties and obtain a synthetic image that will visualise these properties is a challenge in the packaging industry. **Paper VII** [7] contribute towards obtaining a successful visual representation of the non-diffuse and gonio-chromatic packaging materials (*Gold* and *BlueGreen*) using material BRDF that is estimated using two reflectance models, Lafortune model (Lafortune) [60] and micro-facet theory based ABC model (ABC model) [62]. Both the models use a higher but reasonable amount of parameters compared to the CT (with Fresnel term $F = 1$) and the Ward model (used in **Paper VI** [6]). As the measurement obtained using the measurement setup and the gonio-spectrophotometers used are limited to in-plane measurements, an additional non-diffuse material, "Blue Metallic Paint" (BMP), from the MERL dataset [56] was used to asses the performance of the in-plane measurements.

Both the model parameters were optimised for the *Gold*, *BlueGreen*, and BMP material using the in-plane measurements obtained from the measurement setup and the MERL dataset; additionally, the measurements from the GCMS were used for comparison. The choice of the cost function to optimise reflectance model parameters depends on the material to be measured and the reflectance model [62]. Due to the complex reflectance properties of the packaging materials, we used two different metrics (M_1 and M_2) as cost functions when optimising the reflectance model parameters (**Paper VII** [7]).

As the packaging materials are isotropic, we optimised the Lafortune model parameters with the condition $C_x = C_y$. Using the in-plane measurements from the measurement setup for optimisation and the M_1 cost function resulted in the Nelder-Mead downhill simplex algorithm converge to a local minimum making it difficult to obtain an optimal set of the model parameters. Similar results were obtained using the GCMS instrument and in-plane measurements of the MERL dataset for the BMP material.

In the ABC model, A (in S) being not normalised, estimating an optimal set of ABC model parameters using the Nelder-Mead downhill simplex algorithm was difficult. A genetic algorithm (GA) based method was therefore used instead. GA based optimisation methods have been successfully used in the past to learn new analytical BRDF models [70] and for BRDF model parameter remapping [71]. The ABC model parameters were optimised using different measurement datasets from the measurement setup measurements to obtain a salient dataset to successfully estimate material BRDF using the ABC model. In total eight optimisations consisting of two cost functions (M_1 and M_2) and four different data subsets were used to optimise ABC model parameters. Back-scattering measurements often provide enough information to analytically estimate material BRDF [72–74]. In-plane retro-reflective measurements ($\theta_L = 0°$) obtained using the measurement setup were therefore used as one of the subsets.

Synthetic images visualising the complex reflectance properties of the packaging materials were obtained using the Mitsuba renderer [75] along with the geometry and lighting described in [76]. The salient measurement dataset was evaluated by calculating an average relative error across the camera sensors (RGB) using Equation (3.5). Figure 3.18 shows the average relative error obtained while using different measurement datasets and both the cost functions whereas, Figure 3.19, Figure 3.20, and Figure 3.21 shows the renderings obtained using the optimised reflectance models. In-plane retro-reflective measurements were salient enough to obtain a good rendering of the *Gold* and *BlueGreen* materials. Adding more measurements supported the *BlueGreen* material especially for visualisation of the Gonio-chromatic reflectance properties.

3.2.4 Summary

Included papers, **Paper IV** [4], **Paper V** [5], **Paper VI** [6], and **Paper VII** [7], addressed research questions **RQ1**, and **RQ3 - RQ6** from Section 1.2 and mainly contributed towards **BRDF measurement and representation** part of the thesis.

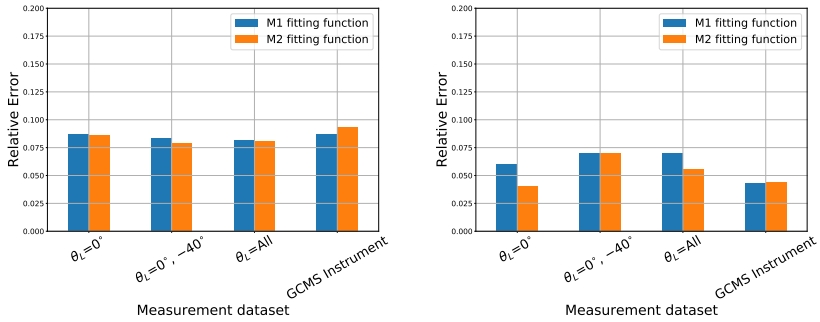

(a) Gold sample. **(b)** Blue-Green sample.

Figure 3.18: Average relative error between the measured and estimated measurement data using ABC model optimised with different measurement datasets and cost functions [Image adapted from **Paper VII** [7]].

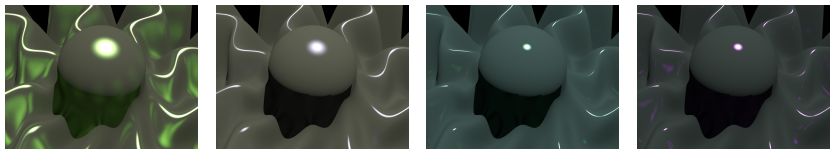

(a) Measurement Setup, *Gold*. **(b)** GCMS instrument, *Gold*. **(c)** Measurement Setup, *BlueGreen* **(d)** GCMS instrument, *BlueGreen*

Figure 3.19: Gold and Blue-Green material renderings using the Lafortune model. In all cases the M_1 fitting function was used [Image adapted from **Paper VII** [7]].

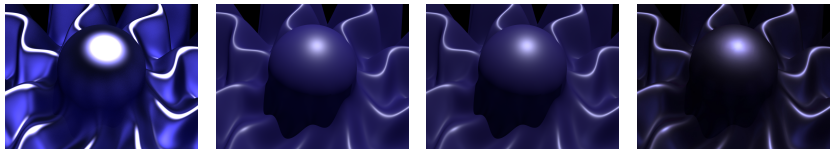

(a) BMP sample - in-plane dataset, M_1, Lafortune model **(b)** BMP sample - in-plane dataset, M_1, ABC model **(c)** BMP sample - in-plane dataset, M_2, ABC model **(d)** BMP sample - full MERL BMP sample dataset

Figure 3.20: BMP sample rendering using full BRDF measurement dataset and the Lafortune and micro-facet ABC model optimised using in-plane MERL dataset measurements [Image adapted from **Paper VII** [7]].

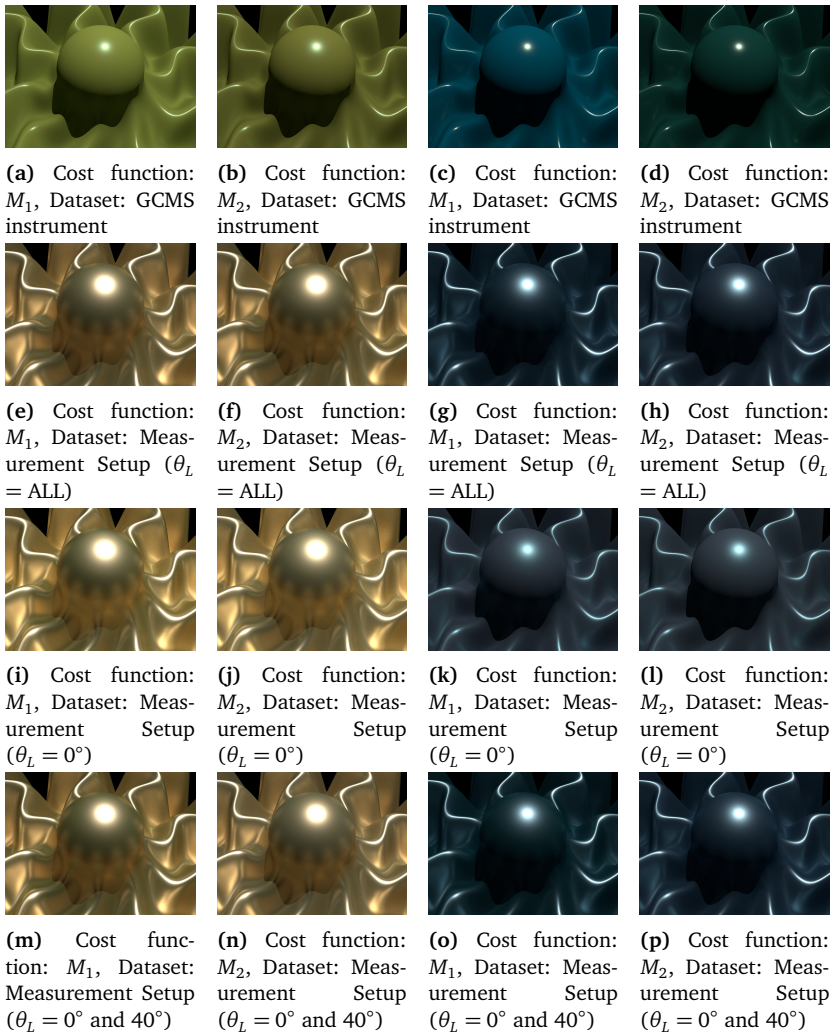

(a) Cost function: M_1, Dataset: GCMS instrument

(b) Cost function: M_2, Dataset: GCMS instrument

(c) Cost function: M_1, Dataset: GCMS instrument

(d) Cost function: M_2, Dataset: GCMS instrument

(e) Cost function: M_1, Dataset: Measurement Setup (θ_L = ALL)

(f) Cost function: M_2, Dataset: Measurement Setup (θ_L = ALL)

(g) Cost function: M_1, Dataset: Measurement Setup (θ_L = ALL)

(h) Cost function: M_2, Dataset: Measurement Setup (θ_L = ALL)

(i) Cost function: M_1, Dataset: Measurement Setup ($\theta_L = 0°$)

(j) Cost function: M_2, Dataset: Measurement Setup ($\theta_L = 0°$)

(k) Cost function: M_1, Dataset: Measurement Setup ($\theta_L = 0°$)

(l) Cost function: M_2, Dataset: Measurement Setup ($\theta_L = 0°$)

(m) Cost function: M_1, Dataset: Measurement Setup ($\theta_L = 0°$ and $40°$)

(n) Cost function: M_2, Dataset: Measurement Setup ($\theta_L = 0°$ and $40°$)

(o) Cost function: M_1, Dataset: Measurement Setup ($\theta_L = 0°$ and $40°$)

(p) Cost function: M_2, Dataset: Measurement Setup ($\theta_L = 0°$ and $40°$)

Figure 3.21: Gold (column 1 and 2) and Blue-Green (column 3 and 4) sample renderings using the micro-facet ABC model. The input data is measured using the GCMS instrument (first row) and using the measurement setup (second, third and last row) [Image adapted from **Paper VII** [7]].

This section presented the work carried out towards estimating and representing BRDF of packaging print materials with the bidirectional measurements obtained using the measurement setup (presented in Section 3.1.1). Measurements from commercially available gonio-spectrophotometers are used to validate the measurement setup and investigate its suitability in performing bidirectional measurements, estimating and representing material BRDF.

Packaging print materials printed using conventional and digital printers have been used as measurement samples. BRDF of these materials is estimated analytically using different reflectance models, measurement datasets and cost functions (**Paper II** [2], **Paper IV** [4], **Paper V** [5], **Paper VI** [6], and **Paper VII** [7]). A salient bidirectional measurement dataset from the measurement setup measurements to estimate and represent material BRDF has been investigated in **Paper VI** [6], and **Paper VII** [7]. The choice of the models and cost functions has been based on the material surface properties, model parameters and computational complexity.

Chapter 4

Discussion

The included papers contribute towards investigating the applicability to use the measurement setup for bidirectional reflectance measurement, and BRDF estimation and representation using different reflectance models. The work carried out in this thesis has to a large extent been dominated by implementation of the measurement setup and aimed towards bringing practicality to the field involving material appearance measurement and representation.

From the literature we learned that such a measurement setup was introduced in the computer graphics field [23, 24, 53–55] mainly for fast BRDF measurement of a variety of materials like, but not limited to, human skin, metal, plastics, and anisotropic materials like cloth, and velvet.

Through the work carried out in this thesis, we presented an image-based measurement setup (refer Section 3.1.1) similar to the one proposed and presented by Marschner *et al.* [24] and Ngan *et al.* [55] to measure flexible, homogeneous, and isotropic materials with an application within the print and packaging industry. The measurement setup (detailed in **Paper I** [1], and **Paper II** [2]) uses a film projector, as the point light source, and a digital camera, as a detector, to measure bidirectional reflectance from the curved measurement sample surface. Within the print and packaging industry, the measurement setup is simple and practically easy to implement in the production line to perform in-line bidirectional reflectance measurements (during process control) and obtain visual representation for quality evaluation and customer approval. However, the materials that can be measured are limited to being flexible, homogeneous and opaque. Considering these limitations, many packaging materials like thick cardboard (non-flexible), polyester (translucent), thin non-flexible wooden plates that are commonly used as a packaging material cannot be measured using the measurement setup. Similar to the setup from Ngan *et al.* [55], the measurement setup can be used for bidirectional reflectance measurements of anisotropic materials.

Spectral sensor sensitivities of the digital camera used, as a detector, in the measurement setup were measured (**Paper II** [2]) using a monochromator. The measured sensitivities supported in converting the obtained reflectance measurements into a colorimetric domain to calculate, evaluate, and compare appearance attributes like colour, lightness, etc. The full width at half maximum (FWHM)

for the monochromatic bandpass used to calculate the camera sensitivities was wide, around 22nm, compared to the bandpass recommended in ISO17321-1 [77] (5nm or narrower). This resulted in camera sensitivities (Figure 3.5) being smoother than expected which may affect the measurements of materials with gonio-chromatic reflectance properties. Access to a monochromator with narrower bandpass was however beyond the scope of this thesis.

Accuracy in performing bidirectional measurements using the measurement setup was investigated using propagation-of-error analysis. Several sources within the measurement setup such as, the camera lens distortion, geometrical error due to physical measurements, $\hat{M}$ calculation, sensor noise, point light source calculation, HDR image generation, material used as reference white (for example spectralon tile) can contribute to the accuracy of the bidirectional reflectance measurements obtained from the measurement setup. We believed that the geometrical error (due to physical measurements) and the matrix error ($\hat{M}$ calculation error due to the camera sensitivity measurements) contribute substantially to the total error in measuring the bidirectional reflectance. These two source of errors were investigated in **Paper III** [3]. The uncertainty in estimating the incident (θ_i) and viewing (θ_r) directions was large (refer Table 3.1) due to the error in performing physical measurements within the measurement setup. This makes us ask the question about whether it is possible to practically implement such a measurement setup in a packaging print production line for in-line bidirectional reflectance measurements? As discussed in **Paper III** [3], the practical use of such a measurement setup will depend on three main points as,

- the appearance attributes and reflectance properties (specularity, gloss, colour, gonio-chromaticity, sparkle, texture, etc) we aim to measure and understand,
- the type of material (whether the material is homogeneous, isotropic and can be wrapped around the cylinder),
- measurement accuracy needed depending on the field of application (print and packaging, medical, metrology, security, cosmetics, etc).

The uncertainty calculated in **Paper III** [3] is representative of the measurement setup represented and used in Section 3.1.1 and **Paper V** [5], **Paper VI** [6], and **Paper VII** [7] respectively. Depending on the material reflectance properties, replacing the detector or the light source with a different kind and performing precise physical measurements (for instance using an optical bench) with the measurement setup can reduce the error in estimating the incident (θ_i) and viewing (θ_r) direction and the measured bidirectional reflectance.

The measurements obtained using the measurement setup are used to estimate material BRDF using analytical reflectance models. When approximating material BRDF it is assumed that the light incident on the sample gets reflected from the same point on the material surface which may not be the case in many packaging materials (like paper, thin flexible cardboard, etc) due to sub-surface scattering.

The choice of analytical reflectance model has been based on the material

surface properties of the materials being measured and computational simplicity in terms of optimising a minimum number of model parameters. The overall goal was to have a simple, easy to implement and relatively fast measurement setup to measure, estimate, and represent BRDF of materials with different reflectance properties. With this goal, the obvious choice was to estimate material BRDF with simple and well-established reflectance models.

To estimate material BRDF, reflectance model parameters were optimised using different measurement data sets and cost functions (**Paper II** [2], **Paper IV** [4], **Paper V** [5], **Paper VI** [6], **Paper VII** [7]). Different combination of illumination directions (θ_L) within the measurement setup helped in obtaining measurement data sets with different illumination (θ_i) and viewing (θ_r) directions. The setup was evaluated by comparing it with two commercially available gonio-spectrophotometers. Packaging print materials with different reflectance properties were used as measurement samples. Access to commercially available gonio-spectrophotometers and the material with gonio-chromatic reflectance properties was a big challenge.

From the findings in **Paper VI** [6] and **Paper VII** [7], packaging materials similar to *BlueGreen* material require flexible models with more free parameters to estimate the gonio-chromatic reflectance properties. In-plane retro-reflective measurements proved to be sufficient for obtaining a good enough BRDF estimate and visual representation of non-diffuse and gonio-chromatic packaging print materials measured in (**Paper VII** [7]). This finding does bear resemblance to the results from Guo *et al.* [72], Ashikhmin and Premoze [73] and Guo and Pan [74]. Measurements in addition to retro-reflective measurements helped improve BRDF estimation especially of the material with gonio-chromatic reflectance properties.

Two incident light directions (θ_L), to illuminate the measurement sample in the measurement setup, were sufficient to analytically estimate BRDF of the materials measured in this thesis. These findings were similar to the one made by Nielsen *et al.* [78] where they have used the MERL dataset instead. Implementing the measurement setup, with two incident light directions (θ_L), for in-line measurements in a print production line should ideally be possible provided the measurement error could be controlled with precise physical measurements within the measurement setup.

This thesis has been carried out at a research laboratory that has been primarily focusing on its research activities within the field of colour measurement, imaging, and image quality. Therefore, until recently, the scope of this thesis had been on bidirectional reflectance measurement, estimation, and representation in the field of print and packaging, colour imaging, metrology, and goniometric measurements. A large number of measurements were performed in this thesis to generate data sets that will help to analytically estimate material BRDF. This was done with the understanding that using more number of measurements will result in a better BRDF estimate. Recently, with the research within the field of visual appearance where colour is one of the visual appearance attributes, the research activities in the laboratory have started to get closer to the work conducted within the field of Computer Graphics. This thesis has contributed and supported this change in

the research directions and has worked on the integration that has resulted in the work presented in **Paper VI** [6] and **Paper VII** [7]. Referring to the field of Computer Graphics, an ideal approach to address the thesis objectives could have been to start with a minimum number of measurements and gradually increase the measurements within the data set to find an optimal data set for BRDF estimation. This would have helped us achieve the results (that we have achieved today) much faster with less number of measurements and thus leaving more time for an investigation related to the measurement setup accuracy as discussed above.

Chapter 5

Conclusion

This thesis has presented the work carried out towards investigating the applicability of using the measurement setup to perform bidirectional reflectance measurements of flexible and homogeneous packaging print materials and analytically estimate and represent material BRDF. Findings and scientific contributions presented in Chapter 3 address various aspects of the applicability of using such a setup for bidirectional measurements. We followed an exploratory approach, where the work carried out is a direct consequence of the findings along the thesis duration. The included papers and publications, therefore, show a common theme and approach and are very well related to the overall thesis objective. To address the research questions (**RQ1-6**) set out in Section 1.2 and the overall thesis objective, we divided the work in two parts, **Imaging and Instrumentation** and **BRDF measurement and representation**.

We introduced an image-based measurement setup to perform bidirectional reflectance measurements in a fast and inexpensive way by using a commercially available digital camera as a detector and a point light source to illuminate the measurement sample. By curving the sample onto a cylinder we can record bidirectional measurements in a single photograph thus reducing the measurement time (**RQ1**). The accuracy of the measurement setup was calculated by comparing it with two commercially available gonio-spectrophotometers (**RQ2**). The error in estimating the incident (θ_i) and viewing (θ_r) direction being large, the measurement setup needs more precise physical measurements for accurate bidirectional reflectance measurements.

BRDF of flexible, homogeneous, and isotropic print materials was estimated analytically using different reflectance models and measurements obtained using the measurement setup (**RQ3**). In-plane retro-reflective measurements were sufficient to obtain a good enough BRDF estimate and visual representation of materials measured in this thesis (**RQ4 - RQ6**). Using a minimum of two illumination directions was sufficient to analytically estimate material BRDF (**RQ4**).

With precise (physical) measurements within the measurement setup and camera sensor sensitivity, the measurement setup can be used as a tool to produce new BRDF data sets of flexible, homogeneous and isotropic materials with different reflectance properties not only within the print and packaging industry but also

beyond.

With the above said, we conclude that we worked and investigated the research questions (**RQ1-6**) and the overall objective set out at the beginning of this thesis.

Chapter 6

Future work

The measurement setup performs in-plane bidirectional reflectance measurements of isotropic and flexible materials having a homogeneous surface. A natural extension to the work carried out in this thesis would be to investigate further the applicability of the measurement setup to perform out-of-plane measurements (azimuthal directions) and measure anisotropic materials.

Referring to the work done by Ngan *et al.* [55], the measurement samples can be wrapped around the circular cylinder in different orientations to be able to measure at different azimuthal (ϕ_i, ϕ_r) directions. This will enable us to perform bidirectional measurements of anisotropic materials in addition to the isotropic materials.

Using the circular cylinder as a sample holder limits the measurement setup to measure at the grazing angles (directions far away from the surface normal). This can be addressed by exploring the use of objects with elliptical shape instead of cylinders to hold the sample or to use a camera with fish-eye lens as a detector. With the need to measure materials with complex reflectance properties, the DLSR camera used as a detector in the measurement setup can be replaced with a multi-spectral or light-field camera to be able to record measurements in the UV and near-infrared range of the electromagnetic spectrum.

The packaging materials used as measurement samples in this thesis were limited to having diffuse, non-diffuse and gonio-chromatic reflectance properties. A number of materials with different visual properties like sparkle and holograms are produced and widely used within the packaging industry. Holographic foils are widely used to create shiny and attractive packaging. The work done in [79–81] to measure, estimate, and visualise reflectance properties of such homogeneous materials can be explored further by performing bidirectional reflectance measurements using the measurement setup for BRDF/BTF and svBRDF estimation.

Bibliography

[1] A. Sole, I. Farup and S. Tominaga, 'An image based multi-angle method for estimating reflection geometries of flexible objects', in *Color and Imaging Conference*, vol. 2014, Society for Imaging Science and Technology, 2014, pp. 91–96.

[2] A. Sole, I. Farup and S. Tominaga, 'Image based reflectance measurement based on camera spectral sensitivities', *Electronic Imaging*, vol. 2016, no. 9, pp. 1–8, 2016, ISSN: 2470-1173.

[3] A. Sole, I. Farup, P. Nussbaum and S. Tominaga, 'Evaluating an image-based bidirectional reflectance distribution function measurement setup', *Applied Optics*, vol. 57, no. 8, pp. 1918–1928, 2018.

[4] A. Sole, I. Farup and T. Shoji, 'An image-based multi-directional reflectance measurement setup for flexible objects', in *Measuring, Modelling, and Reproducing Material Appearance 2015*, SPIE/IS&T Electronic Imaging 2015, 2015.

[5] A. Sole, I. Farup and P. Nussbaum, 'Evaluating an image based multi-angle measurement setup using different reflection models', *Electronic Imaging*, vol. 2017, no. 8, pp. 101–107, 2017, ISSN: 2470-1173.

[6] A. Sole, I. Farup, P. Nussbaum and S. Tominaga, 'Bidirectional reflectance measurement and reflection model fitting of complex materials using an image-based measurement setup', *Journal of Imaging*, vol. 4, no. 11, 136:1–16, 2018.

[7] A. Sole, G. C. Guarnera, I. Farup and P. Nussbaum, 'Measurement and rendering of complex non-diffuse and goniochromatic packaging materials', *Manuscript submitted for publication*, 2019.

[8] P. Nussbaum, A. Sole and J. Y. Hardeberg, 'Analysis of color measurement uncertainty in a color managed printing workflow', *Journal of Print and Media Technology Research*, no. 1, pp. 7–24, 2012.

[9] P. Janíček, E. Schützová, O. Panák, A. S. Sole and P. Nussbaum, 'Measurement of bidirectional reflectance distribution function on custom made gonio spectrophotometer', *Scientific papers of the University of Pardubice. Series A, Faculty of Chemical Technology. 24/2018*, 2018.

[10] K. Kehren, 'Optical properties and visual appearance of printed special effect colors', PhD thesis, Technischen Universität Darmstadt, Darmstadt, Germany, 2013.

[11] C. McCamy, 'Observation and measurement of the appearance of metallic materials. part i. macro appearance', *Color Research & Application*, vol. 21, no. 4, pp. 292–304, 1996.

[12] R. G. W. Hunt, *Measuring Color*, 3rd ed. Fountain Press, 1998.

[13] A. Takagi, S. Sato and G. Baba, 'Prediction of spectral reflectance factor distribution of color-shift paint finishes', *Color Research & Application*, vol. 32, no. 5, pp. 378–387, 2007.

[14] A. Ferrero, A. Rabal, J. Campos, F. Martínez-Verdú, E. Chorro, E. Perales, A. Pons and M. L. Hernanz, 'Spectral BRDF-based determination of proper measurement geometries to characterize color shift of special effect coatings', *JOSA A*, vol. 30, no. 2, pp. 206–214, 2013.

[15] CIE15.2, *Colorimetry*, CIE standard, 2004.

[16] C. McCamy, 'Observation and measurement of the appearance of metallic materials. part ii. micro appearance', *Color Research & Application*, vol. 23, no. 6, pp. 362–373, 1998.

[17] A. Höpe, K. Hauer, T. Atamas and K. Kehren, 'Appearance of printed interference effect ink in commercially used multi-geometry configurations', in *2nd CIE Expert Symposium on Appearance-When appearance meets lighting, Book of Abstracts*, 2010, pp. 56–58.

[18] M. R. Pointer, N. J. Barnes, M. J. Shaw and P. J. Clarke, 'A new goniospectrophotometer for measuring gonio-apparent materials', *Coloration technology*, vol. 121, no. 2, pp. 96–103, 2005.

[19] A. Gilchrist, 'Characterising special-effect colours', *Surface Coatings International Part B: Coatings Transactions*, vol. 85, no. 4, pp. 281–285, 2002, ISSN: 1476-4865.

[20] ASTM-E2539, *Standard practise for multiangle color measurement of interference pigments*, ASTM Standard, 2012.

[21] ASTM-E2194, *Standard practise for multiangle color measurement of metal flake pigmented materials*, ASTM Standard, 2012.

[22] F. E. Nicodemus, J. Richmond, J. J. Hsia, I. W. Ginsberg and T. Limperis, *Geometrical considerations and nomenclature for reflectance*, National Bureau of Standards, 1977.

[23] J. Rong Lu, J. Koenderink and A. M. L. Kappers, 'Optical properties (bidirectional reflection distribution functions) of velvet', *Applied Optics*, vol. 37, no. 25, pp. 5974–5984, 1998.

[24] S. R. Marschner, S. H. Westin, E. P. F. Lafortune, K. E. Torrance and D. P. Greenberg, 'Image-based brdf measurement including human skin', in *10th Eurographics Workshop on Rendering*, 1999, pp. 139–152.

[25] D. Guarnera, G. C. Guarnera, A. Ghosh, C. Denk and M. Glencross, 'BRDF representation and acquisition', in *Computer Graphics Forum*, Wiley Online Library, vol. 35, 2016, pp. 625–650.

[26] W. Jakob, *Mitsuba renderer*, http://www.mitsuba-renderer.org, 2010.

[27] M. Pharr, W. Jakob and G. Humphreys, *Physically based rendering: From theory to implementation*. Morgan Kaufmann, 2016.

[28] C. Eugène, 'Measurement of "total visual appearance": A CIE challenge of soft metrology', in *12th IMEKO TC1 and TC7 Joint Symposium on Man, Science and Measurement*, Annecy, France, 2008, pp. 61–65.

[29] CIE175, 'A framework for the measurement of visual appearance', International Commission on illumination, Tech. Rep., 2006.

[30] F. J. Maile, G. Pfaff and P. Reynders, 'Effect pigments—past, present and future', *Progress in organic coatings*, vol. 54, no. 3, pp. 150–163, 2005.

[31] G. Pfaff, *Special effect pigments: technical basics and applications*. Vincentz Network GmbH & Co KG, 2008.

[32] M. Haas, 'Impacts on the impression of printed effect pigments', in *Proceedings of the 38th International Research Conference of IARIGAI*, 2011.

[33] R. S. Berns, *Billmeyer and Saltzman's Principles of Color Technology*. John Wiley & Sons, 2000.

[34] M. E. Nadal and E. A. Early, 'Color measurements for pearlescent coatings', *Color Research & Application*, vol. 29, no. 1, pp. 38–42, 2004.

[35] G. A. Klein and T. Meyrath, *Industrial color physics*. Springer, 2010, vol. 154.

[36] I. Tomić, S. Dedijer, D. Novaković and I. Jurič, 'Artificial neural networks for optimising camera-based colour measurements of prints enhanced with pearlescent pigments', *Coloration Technology*, vol. 134, no. 5, pp. 364–372, 2018.

[37] J. Palmer and B. G. Grant, *The Art of Radiometry*, ISBN 978-0-8194-7245-8. SPIE Press Bellingham, Washington USA, 2010.

[38] H.-C. Lee, *Introduction to color imaging science*. Cambridge University Press, 2005.

[39] R. McCluney, *Introduction to Radiometry and Photometry*. Artech house, Inc, 1994.

[40] W. L. Wolfe, *Introduction to radiometry*. SPIE Press, 1998, vol. 29.

[41] CIE17.4, *International lighting vocabulary*, CIE standard, 1987.

[42] N. Johansson, 'Measuring and modelling light scattering in paper', PhD thesis, Mid Sweden University, 2015.

[43] ISO5-4, *Photography and graphic technology - density measurements: Geometric conditions for reflection density*, ISO standard, 2009.

[44] ASTM-E179, *Standard guide for selection of geometric conditions for measurement of reflection and transmission properties of materials*, ASTM Standard, 2012.

[45] ASTM-E2175, *Standard practise of specifying the geometry of multiangle spectrophotometers*, ASTM Standard, 2008.

[46] N. Johansson and M. Andersson, 'Angular variations of reflectance and fluorescence from paper-the influence of fluorescent whitening agents and fillers', in *Color and Imaging Conference*, Society for Imaging Science and Technology, vol. 2012, 2012, pp. 236–241.

[47] D. Hünerhoff, U. Grusemann and A. Höpe, 'New robot-based gonioreflectometer for measuring spectral diffuse reflection', *Metrologia*, vol. 43, no. 2, S11, 2006.

[48] R. Baribeau, W. S. Neil and É. Côté, 'Development of a robot-based gonioreflectometer for spectral BRDF measurement', *Journal of Modern Optics*, vol. 56, no. 13, pp. 1497–1503, 2009.

[49] G. Obein, R. Bousquet and M. E. Nadal, 'New NIST reference goniospectrometer', in *Optical Diagnostics*, International Society for Optics and Photonics, vol. 5880, 2005, 58800T.

[50] F. B. Leloup, S. Forment, P. Dutré, M. R. Pointer and P. Hanselaer, 'Design of an instrument for measuring the spectral bidirectional scatter distribution function', *Applied optics*, vol. 47, no. 29, pp. 5454–5467, 2008.

[51] W. Zhang and F. Wang, 'Measuring of spectral BRDF using fiber optic spectrometer', in *5th International Symposium on Advanced Optical Manufacturing and Testing Technologies: Optoelectronic Materials and Devices for Detector, Imager, Display, and Energy Conversion Technology*, International Society for Optics and Photonics, vol. 7658, 2010.

[52] S. R. Marschner, S. H. Westin, E. P. Lafortune, K. E. Torrance and D. P. Greenberg, 'Image-based BRDF measurement including human skin', in *Rendering Techniques' 99*, Springer, 1999, pp. 131–144.

[53] J. Arney, H. Heo and P. Anderson, 'A micro-goniophotometer and the measurement of print gloss', *Journal of Imaging Science and Technology*, vol. 48, no. 5, pp. 458–463, 2004.

[54] S. Tominaga and N. Tanaka, 'Estimating reflection parameters from a single color image', *IEEE Computer Graphics and Applications*, vol. 20, no. 5, pp. 58–66, 2000.

[55] A. Ngan, F. Durand and W. Matusik, 'Experimental analysis of brdf models.', *Rendering Techniques*, vol. 2005, no. 16, p. 2, 2005.

[56] W. Matusik, 'A data-driven reflectance model', PhD thesis, Massachusetts Institute of Technology, 2003.

[57] J. B. Nielsen, H. Aanæs, J. R. Frisvad and K. Conradsen, 'On practical sampling of bidirectional reflectance', PhD thesis, Technical University of Denmark (DTU), 2016.

[58] B. T. Phong, 'Illumination for computer generated pictures', *Communications of the ACM*, vol. 18, no. 6, pp. 311–317, 1975.

[59] G. WARD, 'Measuring and modeling anisotropic reflection', *Computer graphics*, vol. 26, no. 2, pp. 265–272, 1992.

[60] E. P. Lafortune, S.-C. Foo, K. E. Torrance and D. P. Greenberg, 'Non-linear approximation of reflectance functions', in *Proceedings of the 24th annual conference on Computer graphics and interactive techniques*, ACM Press/Addison-Wesley Publishing Co., 1997, pp. 117–126.

[61] R. L. Cook and K. E. Torrance, 'A reflectance model for computer graphics', *ACM Transactions on Graphics (TOG)*, vol. 1, no. 1, pp. 7–24, 1982.

[62] J. Löw, J. Kronander, A. Ynnerman and J. Unger, 'Brdf models for accurate and efficient rendering of glossy surfaces', *ACM Transactions on Graphics (TOG)*, vol. 31, no. 1, p. 9, 2012.

[63] E. L. Church, P. Z. Takacs and T. A. Leonard, 'The prediction of BRDFs from surface profile measurements', in *Scatter from Optical Components*, International Society for Optics and Photonics, vol. 1165, 1990, pp. 136–151.

[64] E. L. Church and P. Z. Takacs, 'Optimal estimation of finish parameters', in *Optical Scatter: Applications, Measurement, and Theory*, International Society for Optics and Photonics, vol. 1530, 1991, pp. 71–86.

[65] G. Wyszecki and W. Stiles, 'Color science: Concepts and methods, quantitative data and formulas', 1968.

[66] J. JCGM *et al.*, 'Evaluation of measurement data—guide to the expression of uncertainty in measurement', *Int. Organ. Stand. Geneva ISBN*, vol. 50, p. 134, 2008.

[67] P. E. Debevec and J. Malik, 'Recovering high dynamic range radiance maps from photographs', in *ACM SIGGRAPH 2008 classes*, ACM, 2008, p. 31.

[68] J. A. Nelder and R. Mead, 'A simplex method for function minimization', *The computer journal*, vol. 7, no. 4, pp. 308–313, 1965.

[69] A. Höpe and K.-O. Hauer, 'Three-dimensional appearance characterization of diffuse standard reflection materials', *Metrologia*, vol. 47, no. 3, p. 295, 2010.

[70] A. Brady, J. Lawrence, P. Peers and W. Weimer, 'Genbrdf: Discovering new analytic brdfs with genetic programming', *ACM Transactions on Graphics (TOG)*, vol. 33, no. 4, p. 114, 2014.

[71] D. Guarnera, G. C. Guarnera, M. Toscani, M. Glencross, B. Li, J. Y. Hardeberg and K. Gegenfurtner, 'Perceptually validated cross-renderer analytical BRDF parameter remapping', 2018.

[72] J. Guo, Y.-w. Guo and J.-g. Pan, 'A retroreflective brdf model based on prismatic sheeting and microfacet theory', *Graphical Models*, vol. 96, pp. 38–46, 2018.

[73] M. Ashikhmin and S. Premoze, 'Distribution-based brdfs', *Unpublished Technical Report*, p. 10, 2007.

[74] J. Guo and J. Pan, 'A physically-based brdf model for retroreflection', in *Proceedings of the Computer Graphics International Conference*, ACM, 2017, p. 36.

[75] W. Jakob, *Mitsuba renderer, 2010*, 2010.

[76] V. Havran, J. Filip and K. Myszkowski, 'Perceptually motivated brdf comparison using single image', in *Computer Graphics Forum*, Wiley Online Library, vol. 35, 2016, pp. 1–12.

[77] ISO17321-1, *Graphic technology and photography - colour characterisation of digital still cameras (dscs) - part 1: Stimuli, metrology and test procedures*, ISO standard, 2012.

[78] J. B. Nielsen, H. W. Jensen and R. Ramamoorthi, 'On optimal, minimal brdf sampling for reflectance acquisition', *ACM Transactions on Graphics (TOG)*, vol. 34, no. 6, p. 186, 2015.

[79] A. Ferrero and S. Bayón, 'The measurement of sparkle', *Metrologia*, vol. 52, no. 2, p. 317, 2015.

[80] A. Toisoul, D. S. Dhillon and A. Ghosh, 'Acquiring spatially varying appearance of printed holographic surfaces', in *SIGGRAPH Asia 2018 Technical Papers*, ACM, 2018, p. 272.

[81] J. Guo, Y. Chen, Y. Guo and J. Pan, 'A physically-based appearance model for special effect pigments', in *Computer Graphics Forum*, Wiley Online Library, vol. 37, 2018, pp. 67–76.

Paper I

A. Sole, I. Farup and S. Tominaga, 'An image based multi-angle method for estimating reflection geometries of flexible objects', in *Color and Imaging Conference*, vol. 2014, Society for Imaging Science and Technology, 2014, pp. 91–96

Paper II

A. Sole, I. Farup and S. Tominaga, 'Image based reflectance measurement based on camera spectral sensitivities', *Electronic Imaging*, vol. 2016, no. 9, pp. 1–8, 2016, ISSN: 2470-1173

Image based reflectance measurement based on camera spectral sensitivities

Aditya Sole*[1]*, Ivar Farup*[1]*, and Shoji Tominaga*[2]*;
1. The Norwegian Colour and Visual Computing Laboratory, Gjøvik University College, Gjøvik, Norway,
2. Graduate School of Advanced Integration Science, Chiba University, Chiba, Japan

Abstract

Image based measurement techniques are increasingly used to perform multi-directional reflectance measurements of objects/materials. In these techniques, commercially available colour (RGB) cameras are used along with the monochrome CCD cameras to measure the radiance reflected from the object/material surface at multiple reflection directions. The data acquired through these cameras is used to estimate the BRDF of given sample/material.

This paper presents an image-based method to measure the reflectance of the sample material using the camera spectral sensitivities. A multi-angle measurement setup described in previous studies was used to perform the measurements. A reflection model of the sample was derived in a colorimetric space using the Phong model. Camera spectral sensitivities were measured using a Bentham monochromator to build a tranformation from Camera RGB to CIEXYZ colour space. A reflection model was fitted in the colorimetric domain (CIEXYZ) for the sample materials used. Results show that image based multi-directional reflectance measurements can be performed using the camera spectral sensitivities.

Introduction

Multi-angle instruments and gonio-spectrometers are increasingly used to perform multi-directional measurements of radiance reflected from objects/materials (especially goniochromatic and non-diffuse object materials like metallic inks and special effect coatings). These instruments are precise and accurate and provide the measurements to calculate the bidirectional-reflection distribution function (BRDF) of a given objects/material. However, they are expensive, measure at fixed illumination and reflection angles and performing measurements is time consuming [1].

To overcome these drawbacks, image-based measurement techniques are increasingly used in performing multi-directional reflectance measurements of objects/materials [2, 3, 4]. These are fast and relatively cheaper. Monochrome CCD cameras or commercially available digital colour (RGB) cameras are used in these setups. The image captured using the colour camera records the light information in digital values [0 - 225] (for an 8-bit camera) for the individual camera sensors (R, G and B) also known as camera response C_k for that particular pixel.

The camera response C_k, for an image pixel, can be modelled using Equation (1).

$$C_k^j = \sum_i E(\lambda_i) \times R_j(\lambda_i) \times Q_k(\lambda_i)\Delta\lambda + n_k \qquad (1)$$

Where, C_k^j is the sensor response for the k^{th} channel (R, G, B or monochrome) and for j^{th} pixel, n_k is the noise in the k^{th} channel, Q_k is the spectral sensitivity function for the k^{th} sensor channel, $E(\lambda)$ is the spectral power distribution of the illuminant, $R_j(\lambda)$ is the spectral reflectance imaged at pixel j, scalar $\Delta\lambda$ is the sampling step (in nm).

In order to compare measurements made using image based techniques to measurements performed using gonio-spectrometers or multi-angle spectrophotometers (which basically record the radiance reflected from the sample object in the spectral range 380nm - 730nm), we will have to either convert the camera captured R, G and B digital values to spectral or colorimetric values or convert the spectral reflectance values captured by the multi-angle spectrophotometers and gonio-spectrometers to camera RGB (digital) values.

For this conversion, it is important to know the camera spectral sensor sensitivity (Q_k) functions of the imaging device used in the measurement setup. Digital camera spectral sensitivity data being confidential is difficult to obtain from the camera manufacturer and is therefore needed to be either measured or estimated.

Looking at some of the work done till now in the area of digital camera spectral sensitivity measurements [5, 6, 7, 8, 9] we can observe that direct measurement of camera spectral sensitivity using a monochromator and a radiometer is much more accurate compared to estimation using colour patches with known spectral reflectance (for example using a ColourChecker test chart). However, the drawback in using the direct measurement approach is the time required, cost and availability of expensive equipment like monochromator and radiometers. Recently, a multi-primary image projector based camera sensitivity measurements system was introduced by Hirai et. al [10], where they used a multi-primary image projector to generate the monochromatic light which is used to measure the camera sensitivity. They used a one-shot-type camera spectral sensitivity measurement in which they reproduce rainbow projection for the measurement.

In this study we used a monochromator to measure the camera spectral sensitivities of the red (R), green (G) and blue (B) channels of the Nikon D200 camera. These measured camera sensitivities were further used in converting the camera RGB data to CIEXYZ colorimetric data. The camera spectral sensitivity measurement procedure and camera RGB to CIEXYZ conversion matrix estimation process is explained in the *Method's* section.

An image based multi-directional measurement setup as described in [4] was used to perform multi-angle colour measurements of a homogenous flexible packaging paper material. As discussed by us [4], modelling the reflection properties of mate-

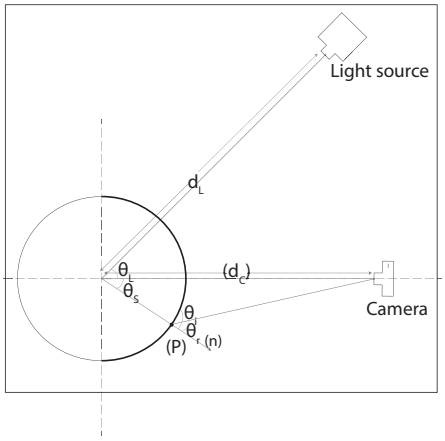

Figure 1. *Multi-angle measurement setup [4].*

rial surface is important for material appearance measurement and simulation and is used mostly in the computer graphics field to generate image simulations [11, 12, 13]. A reflection model was fitted using the Phong model to the data measured by the measurement setup. The Phong model is an empirical model with two surface reflectance components, one for diffuse surface (diffuse component) and one for specular surface (specular component) [11]. A three-dimensional light reflection using the Phong model can be described [14] as

$$H(\theta_i,\theta_r,\lambda) = S_a(\lambda)E(\lambda) + (\cos\theta_i)S_d(\lambda)E(\lambda) + (\cos^{\alpha}(\theta_r-\theta_i))S_sE(\lambda) \quad (2)$$

$H(\theta_i,\theta_r,\lambda)$ is the radiance of light reflected from a surface and is a function of wavelenght (λ), including the illumination direction angle (θ_i) and the viewing angle (θ_r). $S_a(\lambda)$ is the ambient-spectral reflectance, $S_d(\lambda)$ is the diffuse-spectral reflectance of an object (diffuse component), S_s is the specular constant, and $E(\lambda)$ is the spectral power distribution of the light source. α is used as the measure of surface roughness.

Objectives

The objectives of the work presented in this paper are:

- to measure the sensor spectral sensitivity of the camera used as an imaging device in the multi-angle measurement setup. Obtaining these should help convert the camera RGB data to colorimetric/spectral space.
- to evaluate the measured sensor spectral sensitivity functions.
- to fit a reflection model in a colorimetric space using the camera measured data of the sample materials.
- to evaluate the reflection model.

Method

Sensor sensitivity measurement

As an imaging device in the multi-dimensional measurement setup, we used a commercially available Nikon D200 digital camera to capture the light reflected from the samples. Spectral sensitivity of the 3 sensors (R, G and B) of the camera were measured.

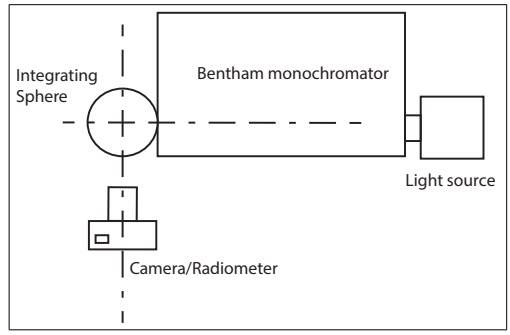

Figure 2. *Schematic diagram of the camera sensor sensitivity measurement setup.*

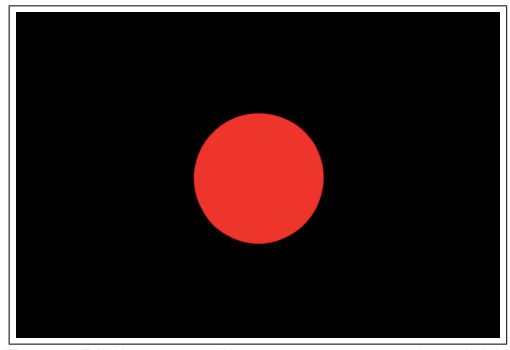

Figure 3. *RAW image captured by camera at 610nm monochromatic light.*

In order to be precise and with limited access to a Bentham monochromator and Minolta CS1000 Tele-Spectro-Radiometer (TSR), we used the direct measurement approach to measure the spectral sensitivity of the Nikon D200. The 3 sensors' (R, G and B) sensitivity were measured by recording their responses to monochromatic light bands (narrow band wavelengths) using the monochromator. The measurements were performed in a dark-room. Figure 2 shows a schematic diagram of the measurement setup. The monochromator was mounted with a $BaSO_4$ coated sphere at the exit to have a uniform light output. The camera was positioned exactly in front of the sphere and focused. The distance between the camera and the sphere was adjusted in a way that the projected light was recorded in the center of the camera sensor array. Figure 3 shows an illustration of the RAW image captured by the camera of the monochromatic light projected at 610nm. RAW images of the monochromatic light ranging from 380nm to 730 nm at 10 nm intervals were captured by the camera.

Figure 4 shows the camera responses for the projected monochromatic light. After recording the projected light with the camera sensors, same was measured using the TSR to record the spectral power of the monochromatic light. For this, the

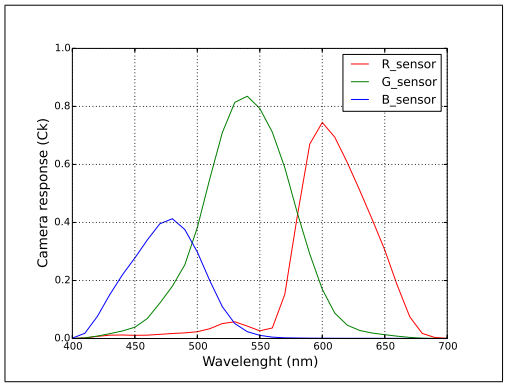

Figure 4. *Camera response to monochromatic projections.*

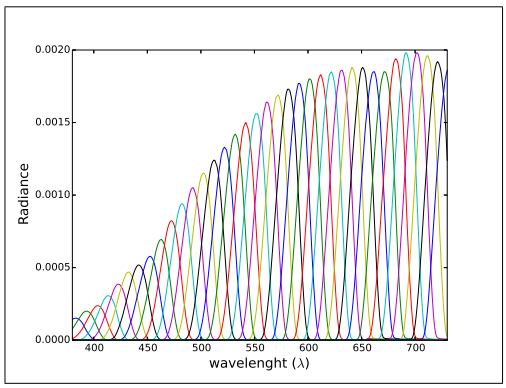

Figure 5. *Spectral power distribution of monochromatic bands.*

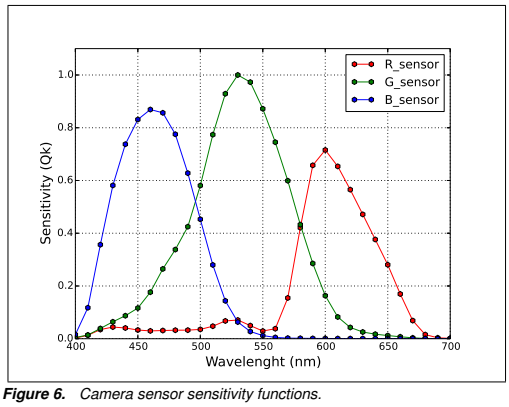

Figure 6. *Camera sensor sensitivity functions.*

camera was replaced with the TSR in the setup (refer Figure 2). Figure 5 shows the spectral power distributions measured by the TSR for all the monochromatic lights (400nm to 700nm at 10nm intervals) projected by the monochromator. In order to find out the actual band-width of the monochromatic bands projected by the monochromator, the Full Width at Half Maximum (FWHM) of the wavelength bandpass was calculated. Table 1 shows the maximum and minimum FWHM for the monochromatic bands used for the camera sensor measurements and the corresponding wavelength peak. The average bandwidth obtained was 22nm. This wide band-width was obtained due to slit limitations on the Bentham monochromator used in the sensor measurement process. According to ISO17321-1 [15], the bandpass of the monochromator to be used as an illuminating instrument shall be 5nm or narrower. However, due to limited access to the monochromator and the monochromator slitwidth limitations, the average minimum slit width obtained was approximately 22 nm. The camera response (see Figure 4) obtained for the

Table 1: Maximum and minimum FWHM of monochromatic bands that are used for camera sensor measurement

Monochromatic band peak (nm)	Bandwidth (nm)
410	20.3
670	23.3

monochromatic bands are dependent on the light source used by the monochromator. The camera sensor sensitivity is therefore calculated using the camera response and the spectral power distribution (SPD) measurements of the monochromatic bands made using the TSR. With reference to Equation (1), the camera response in this measurement procedure can be expressed as,

$$C_k(\lambda) = \sum_i Q_k(\lambda_i) L_k(\lambda_i) \Delta\lambda \tag{3}$$

where, C_k is the sensor response for the k^{th} channel, $Q_k(\lambda)$ is the spectral sensitivity function for the k^{th} sensor channel, $L_k(\lambda)$ is the spectral radiance. Assuming that the monochromatic band-pass $L_k(\lambda)$ has a narrow spectral power distribution compared to the sensor sensitivity in the same wavelength region, Equation (3) will be

$$\begin{aligned} C_k(\lambda) &= Q_k(\lambda) \sum_i L_k(\lambda_i) \Delta\lambda \\ Q_k(\lambda) &= \frac{C_k(\lambda)}{\sum_i L_k(\lambda_i) \Delta\lambda} \end{aligned} \tag{4}$$

Figure 6 shows the camera sensor sensitivities calculated using Equation (4). The main aim of measuring the camera sensitivity functions was to be able to convert the camera RGB data captured using the multi-angle measurement setup to colorimetric space. To do so, we calculate a transformation matrix $\hat{M}$ using the camera sensor sensitivities $(r(\lambda),\ g(\lambda),\ b(\lambda))$ (estimated using Equation (4)) and the CIE 2° colour matching functions $(\bar{x},\ \bar{y},\ \bar{z})$ by minimising the error using the least square technique such as,

$$\hat{M} = \arg\min_M \|C - RM\|_F \tag{5}$$

where, C is a 31×3 matrix containing the CIE 2° colour matching functions, R is a 31×3 matrix of the camera sensitivities $(r(\lambda), g(\lambda), b(\lambda))$ estimated using Equation (4) (refer Figure 6). $\hat{M}$ will be a 3×3 matrix. Therefore the transformed colour matching functions $(\hat{C})$ will be,

$$\hat{C} = R\hat{M} \tag{6}$$

In order to verify the accuracy of the transformation matrix $\hat{M}$ and the camera sensitivity measurements, we did capture a passport size 24 patches ColourChecker test chart. Figure 7 shows the captured image of the test chart using the Nikon D200 camera. The test chart patches were measured using the TSR (by replacing the camera with the TSR) in the same measurement conditions thus keeping the light source and, the illumination direction constant. Camera RGB data of the patches was transformed into CIEXYZ colour space using matrix $\hat{M}$. Similarly CIEXYZ values of the ColourChecker patches were computed from the radiance measurements made using the TSR and the transformed colour matching functions $\hat{C}$. CIEXYZ values were further converted to CIE $L^*a^*b^*$ colourspace using the Spectralon tile in the scene to compute the colour difference. Figure 8 shows a^* vs b^* plots of these 24 patches. An average $\Delta E_{a^*b^*}$ of 3.85 was obtained with the maximum at 8.21 for the cyan patch (refer Row1Column3 in Figure 7). Figure 9 shows a histogram plot of the colour difference in $\Delta E_{a^*b^*}$ for the ColourChecker patches.

Figure 7. *Captured ColourChecker test chart.*

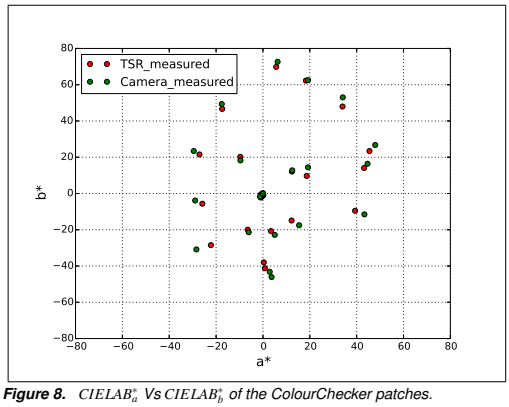

Figure 8. *$CIELAB_a^*$ Vs $CIELAB_b^*$ of the ColourChecker patches.*

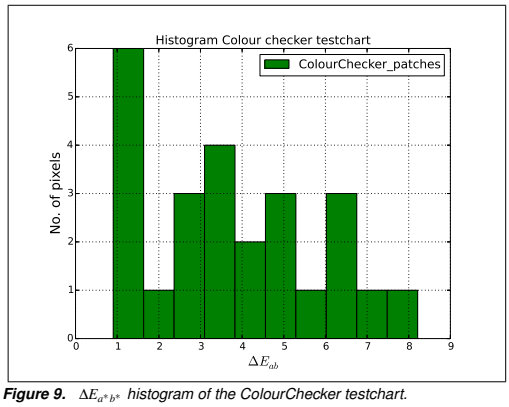

Figure 9. *$\Delta E_{a^*b^*}$ histogram of the ColourChecker testchart.*

Sample measurement

In this paper we used two materials as measurement samples that can be termed as homogeneous flexible packaging materials. The first sample was a 100% Cyan (C) colour patch and second was a 100 % Magenta (M) colour patch, both printed using wax based inks on matt coated white plotter paper using OCE ColorWave 600 plotter.

These 2 samples were measured using the multi-angle measurement setup [4] at three illumination directions (θ_L = 24.5°, 31.5° and 37.6°). A tungsten point source was used as light source illuminating the sample and Nikon D200 DSLR camera as measurement sensor. Paper white (W) was also measured along with the samples (C) & (M).

Figure 10 shows the captured image of the sample at θ_L = 37.6°. Spectralon tile was used as reference white in the scene. The incident (θ_i) and reflection (θ_r) angles at given pixel points (P) were calculated for the 3 illumination directions (θ_L). Captured reflection data of the samples in terms of R, G and B intensities was then converted into CIEXYZ colour space using the transformation matrix $\hat{M}$. Figure 11 and 12 show the *CIEY* value for the corresponding reflection angles for the two samples (C) and (M) at $\theta_L = 24.5^\circ$ and $\theta_L = 37.6^\circ$.

Colorimetric Reflection Model

Measuring and modelling the reflection properties of an object material is important, if the material appearance of it needs to be reproduced using a 2.5D or 3D printing techniques or simulated using computer graphic techniques. Reflection models are used to estimate the reflection properties of these objects/materials. The surface-spectral reflectance of an object/material will vary with 1) the illumination, 2) viewing geometry and, 3) object's material composition [14].

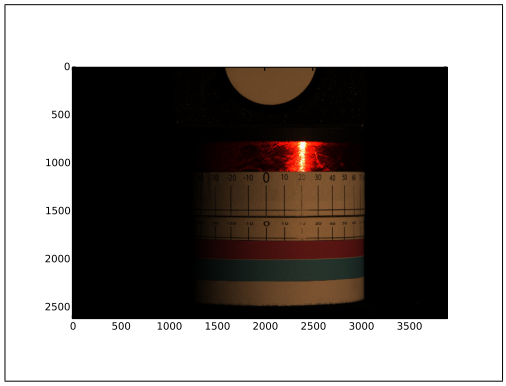

Figure 10. *Sample image captured at $\theta_L = 37.6°$.*

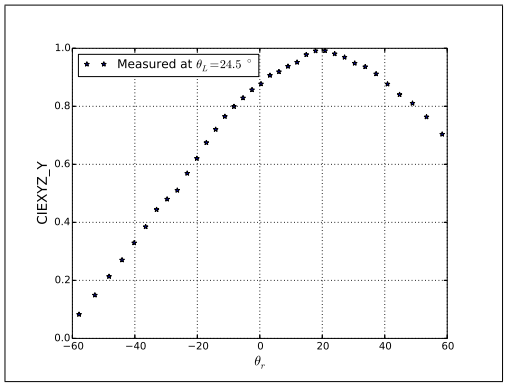

Figure 11. *CIEXYZ Y value of (C) sample.*

The material (C) and (M) used being fairly diffuse we used the Phong model as described in Equation (2) to fit a reflection model for these two materials using the measured data. The Phong model has two components: *body reflectance* also known as diffuse component and *interface reflectance* known as specular component. This model describes the light reflection as a sum of interface and body reflection [14]. Colorimetric data (CIEXYZ) of the samples (C) and (M) (at multiple reflection angles) was obtained from the camera RGB using the conversion matrix $\hat{M}$. A reflection model was fitted in the CIEXYZ colour space using Equation (2) and the colorimetric data (CIEXYZ). As the data measured using RGB colour camera, was converted into the colorimetric space CIEXYZ using conversion matrix $\hat{M}$, referring to the measurement setup [4] and inserting the model parameters in Equation (2), the camera colorimetric output $H_{(X,Y,Z)}$ at spatial location p will be,

$$H_p = \begin{bmatrix} H_{pX} \\ H_{pY} \\ H_{pZ} \end{bmatrix} = k_a \mathbf{H_a} + k_d \mathbf{H_d} (\cos\theta_i) + k_s \mathbf{H_s} (\cos^{\alpha}(\theta_r - \theta_i)) \quad (7)$$

where, $\mathbf{H_a}$ is the ambient light vector, $\mathbf{H_d}$ is the diffuse component (body reflectance) vector proportional to $(S_d(\lambda)E(\lambda))$, $\mathbf{H_s}$ is the specular component (interface reflectance) vector proportional to $E(\lambda)$, θ_i is the incident angle and θ_r the reflection angle. k_a, k_d, k_s are the ambient, diffuse and specular reflection coefficients and α is the coefficient for sample roughness.

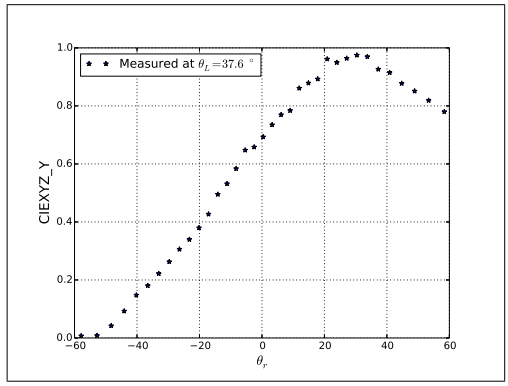

Figure 12. *CIEXYZ Y value of (M) sample.*

As the measurements were performed in the darkroom conditions, the ambient light component $k_a\mathbf{H_a}$ was treated as zero. For the diffuse component, that is the body reflectance of the material, colorimetric values at normal to the camera sensor were used. Due to directional incident light, the measurements at normal to the camera sensor will have the maximum diffuse component and minimum specular component. The illumination light being directional (θ_L = 24.5°, 31.5° and 37.6°) the CIEXYZ values ($X_{d_{sample}}$,$Y_{d_{sample}}$,$Z_{d_{sample}}$) at the center pixel of the camera sensor were used as the body reflectance component $\mathbf{H_d}$. In theory the specular component of the light source will be maximum reflected from the surface of an object/material at $\theta_i = \theta_r$. Therefore, for the specular component $\mathbf{H_s}$ in the reflection model, we used the CIEXYZ values ($X_{s_{white}}$,$Y_{s_{white}}$,$Z_{s_{white}}$) corresponding to pixel position (p) at $\theta_i = \theta_r$ for the given illumination direction (θ_L). Inserting the diffuse and specular component values in Equation (7),

$$H_p = \begin{bmatrix} H_{pX} \\ H_{pY} \\ H_{pZ} \end{bmatrix} = k_d \begin{bmatrix} X_{d_{sample}} \\ Y_{d_{sample}} \\ Z_{d_{sample}} \end{bmatrix} \cos\theta_i + k_s \begin{bmatrix} X_{s_{white}} \\ Y_{s_{white}} \\ Z_{s_{white}} \end{bmatrix} \cos^{\alpha}(\theta_r - \theta_i) \quad (8)$$

Reflection coefficients k_d, k_s and roughness coefficient α were fitted and optimized in Equation (8) using the colorimetric data (CIEXYZ) calculated from the camera measurements performed at the 3 illumination directions (θ_L). Nelder-Mead downhill simplex algorithm [16] was used to optimize the coefficients using the function,

$$Total_{Err_{XYZ}} = \sum_{\theta_L=0}^{M} \sum_{P=0}^{N} \Delta XYZ \quad (9)$$

where,
$\Delta XYZ = \sqrt{(X_{mea} - X_{est})^2 + (Y_{mea} - Y_{est})^2 + (Z_{mea} - Z_{est})^2}$,
$X_{mea}, Y_{mea}, Z_{mea}$ are the CIEXYZ values used to fit the reflection

model using Equation (8),
$X_{est}, Y_{est}, Z_{est}$ are the CIEXYZ values estimated by the reflection model,
p is the total number of pixel values (N) and,
θ_L is the illumination directions (θ_L = 24.5°, 31.5° and 37.6°, that is M = 3). As the measurement data used to fit the reflection model is in the colorimetric colour-space, CIE X, Y and Z data corresponds to the same pixel in the image. We, therefore, use the Euclidean error (ΔXYZ) to minimize the total error. Table 2 shows the coefficients k_d, k_s and α fitted for the two samples (C and M) using Equation (8) and (9).

Table 2: Phong reflection model fitting parameters and LRMS error

Material	K_d	K_s	α	RMSE
C	0.6831	0.0527	1.033	0.10
M	1.4601	0.0766	1.9132	0.11

Results

Table 3: Colorimetric difference in $\Delta E_{a^*b^*}$ between camera measured and the Phong model estimated data

Material	θ_L	Average $\Delta E_{a^*b^*}$	Maximum $\Delta E_{a^*b^*}$
C	24.5°	1.15	1.59
	31.5°	1.36	2.15
	37.6°	1.39	2.36
M	24.5°	1.36	2.17
	31.5°	1.65	2.36
	37.6°	1.60	2.65

Figures 13, 14, show the plots for the camera measured and reflection model estimated CIE Y value for 2 incident light directions (θ_L=24.5°, 37.6°). From the plots it can be observed that the reflection model fitted to the data in the colorimetric space works well. In order to evaluate the accuracy of the model in colorimetric space, the CIEXYZ values measured by the camera and estimated by the reflection model were transformed into CIE $L^*a^*b^*$ values using the spectralon tile measurements made using a tele-spectro-radiometer. Colorimetric wise we get a good fit using the model with an average $\Delta E_{a^*b^*}$ of 1.3 for cyan (C) sample whereas 1.54 for magenta (M) sample in the reflection angle range of θ_r = $-60°$ to $+60°$ where the camera sensor is normal to the sample at $\theta_r = 0°$. Table 3 shows the average and maximum colorimetric differences for the sample materials in the same reflection angle range at the three illumination directions (θ_L). Figure 15 and 16 show the histogram plot for of the $\Delta E_{a^*b^*}$ for both the samples.

Conclusion and Discussion

We presented an image-based method to measure the reflectance of the sample material using the camera spectral sensitivity. Bentham monochromator was used to measure the camera spectral sensitivities. The FWHM for the monochromatic band-pass used was approximately 22nm. Due to limited access to the measurement setup a smaller exit slit on the monochromator could not be used.

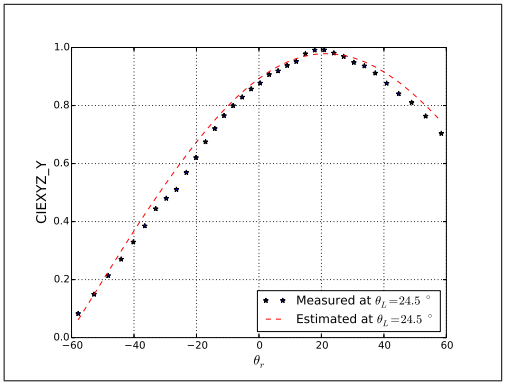

Figure 13. *CIEXYZ Y value of (C) sample measured and estimated at* θ_L = 24.5°.

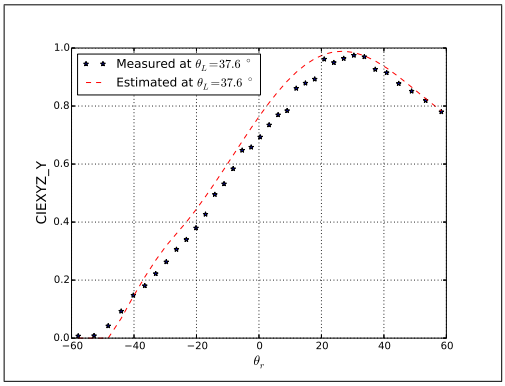

Figure 14. *CIEXYZ Y value of (M) sample measured and estimated at* θ_L = 37.6°.

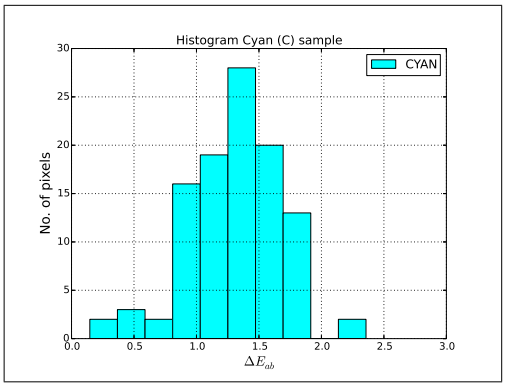

Figure 15. *$\Delta E_{a^*b^*}$ histogram of Cyan (C) sample.*

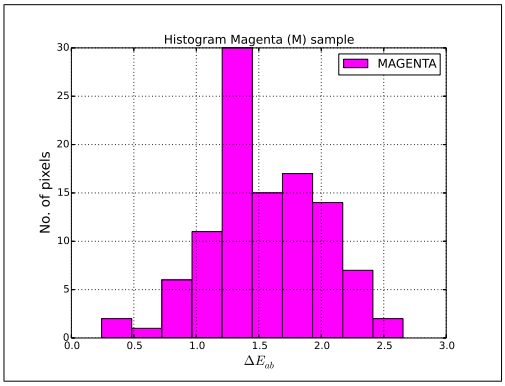

Figure 16. *$\Delta E_{a^*b^*}$ histogram of Magenta (M) sample.*

An important point to note in this study is that we estimated the camera spectral sensitivity with the assumption that the monochromatic bandpass used is narrow enough compared to the sensor sensitivity in the same wavelength region. However, looking at the sensitivity measurements (refer Figure 6) we can observe that this assumption does not hold true for all wavelengths considered in the measurement (i.e. 400 - 700 nm). This will possibly add to the error in the camera sensitivity measurements. If the monochromatic bandpass was narrower (say 5 nm) we should have obtained more sharper sensitivity curves compared to what we have obtained now. A transformation matrix $\hat{M}$ was estimated using the camera sensitivity measurements R and CIE 2° colour matching functions. The sensitivity measurements and transformation was evaluated using a ColourChecker test chart. Looking at the colorimetric difference we can conclude that the performance of the transformation is acceptable and can be used in the reflectance measurement setup.

As the measurement samples used were fairly diffuse, the colorimetric reflectance model was derived using the Phong model. Using the transformation matrix $\hat{M}$, the camera captured data was converted into the colorimetric space (CIEXYZ) and the reflection model was fitted in the CIEXYZ colourspace. The advantage of fitting the reflection model in the colorimetric space is that, the directional reflectance properties of the samples used can be simulated/estimated directly into the colorimetric space. This should support in visualisation of the colour data in the perceptual domain to help understand how we perceive directional colour.

From the results obtained we can conclude that the reflection model works satisfactorily and the sample colorimetric values can be estimated at multiple directions using the proposed model for the sample materials used in this study.

A point to note is that in this study, same measurement dataset is used to train and test the reflection models for both the samples. This can also be considered as one of the reasons to get a good fit between the estimated and measured data. As part of future work the model will be verified using a measurement dataset different than the training dataset. The measurement setup and reflection model will also be verified against measurements performed using a gonio-spectrometer. This should possibly help us validate the measurement setup against reference gonio-measurement instruments like spectro-spectrometers and multi-angle spectrophotometers.

Acknowledgments

We would like to thank and acknowledge the support of Professor Jon Yngve Hardeberg, Professor Philip John Green, Associate Professor Simon J R McCallum, Associate Professor Peter Nussbaum and Post Doctoral Researcher Steven Le Moan at the Norwegian Colour and Visual Computing Laboratory in discussions and suggestions regarding the experimental work and structure of this paper.

References

[1] G. Baba, "Gonio-spectrophotometry of metal-flake and pearl-mica pigmented paint surfaces," in *Proceedings of the fourth Oxford conference on spectrophotometry*, pp. 79–86, SPIE, 2003.

[2] J. Rong Lu, J. Koenderink, and A. M. L. Kappers, "Optical properties (bidirectional reflection distribution functions) of velvet," *Applied Optics*, vol. 37, pp. 5974 – 5984, September 1998.

[3] S. R. Marschner, S. H. Westin, E. P. F. Lafortune, K. E. Torrance, and D. P. Greenberg, "Image-based brdf measurement including human skin," in *10th Eurographics Workshop on Rendering*, pp. 139 – 152, 1999.

[4] A. S. Sole, I. Farup, and S. Tominaga, "An image-based multi-directional reflectance measurement setup for flexible objects," in *Measuring, Modeling and Reproducing Material Appearance 2015* (M. V. O. Segovia, P. Urban, and F. H. Imai, eds.), vol. SPIE 9398, pp. 93980J – 93980J–11, Proceedings of SPIE-IS& T Electronic Imaging, 2015.

[5] M. M. Darrodi, G. Finlayson, T. Goodman, and M. Mackiewicz, "Reference data set for camera spectral sensitivity estimation," *J. Opt. Soc. Am. A*, vol. 32, pp. 381–391, Mar 2015.

[6] J. E. Farrell, P. B. Catrysse, and B. A. Wandell, "Digital camera simulation," *Appl. Opt.*, vol. 51, pp. A80–A90, Feb 2012.

[7] J. Y. Hardeberg, *Acquisition and reproduction of colour images: colorimetric and multispectral approaches*. PhD thesis, Ecole Nationale Superieure des Telecommunications, 1999.

[8] M. M. Darrodi, G. Finlayson, T. Goodman, and M. Mackiewicz, "A ground truth data set for nikon camera's spectral sensitivity estimation," *Color and Imaging Conference*, vol. 2014, pp. 85 – 90, November 2014.

[9] J. Farrell, M. Okincha, and M. Parmar, "Sensor calibration and simulation," in *Digital Photography IV* (J. M. DiCarlo and B. G. Rodricks, eds.), vol. 6817, pp. 68170R–68170R–9, Proceedings of SPIE-IS& T Electronic Imaging, 2008.

[10] K. Hirai, D. Irie, and T. Horiuchi, "Photometric and geometric measurements based on multi-primary image projector," in *Colour and Visual Computing Symposium (CVCS), 2015*, pp. 1 – 5, August 2015.

[11] B. T. Phong, "Illumination for computer generated pictures," *Commun. ACM*, vol. 18, pp. 311–317, June 1975.

[12] J. F. Blinn, "Models of light reflection for computer synthesized pictures," in *Proceedings of the 4th Annual Conference on Computer Graphics and Interactive Techniques*, SIGGRAPH '77, (New York, NY, USA), pp. 192–198, ACM, 1977.

[13] R. L. Cook and K. E. Torrance, "A reflectance model for computer graphics," *ACM Trans. Graph.*, vol. 1, pp. 7–24, Jan. 1982.

[14] S. Tominaga, "Dichromatic reflection models for rendering object surfaces," *Journal of Imaging Science and Technology*, vol. 40,

no. 6, pp. 549 – 555, 1996.

[15] ISO17321-1, "Graphic technology and photography - colour characterisation of digital still cameras (dscs) - part 1: Stimuli, metrology and test procedures." ISO standard, November 2012.

[16] J. A. Nelder and R. Mead, "A simplex method for function minimization," *The Computer Journal*, vol. 7, pp. 308 – 313, January 1965.

Author Biography

Aditya Sole completed his bachelors from PVGs College of Engineering and Technology, Pune University, India in year 2005. In 2007 he completed his MSc in Digital Colour Imaging from London College of Communication, University of the Arts, London, UK. From 2008 till 2012 he worked as a Laboratory Engineer at the Norwegian Colour and Visual Computing Laboratory, Gjøvik University College, Gjøvik, Norway. Since 2012 he is working as a Project Manager and is a PhD student at the Norwegian Colour and Visual Computing, Gjøvik University College.

Paper III

A. Sole, I. Farup, P. Nussbaum and S. Tominaga, 'Evaluating an image-based bi-directional reflectance distribution function measurement setup', *Applied Optics*, vol. 57, no. 8, pp. 1918–1928, 2018

Evaluating an Image Based Multi-angle BRDF Measurement Setup

ADITYA SOLE[1,*], IVAR FARUP[1], PETER NUSSBAUM[1], AND SHOJI TOMINAGA[1,2]

[1] The Norwegian Colour and Visual Computing Laboratory, Department of Computer Science, Faculty of Information technology and Electrical engineering, Norwegian University of Science and Technology
[2] Graduate School of Advanced Integration Science, Chiba University, Chiba, Japan
[*] Corresponding author: aditya.sole@ntnu.no

Compiled January 31, 2018

We evaluate an image based multi-angle BRDF measurement setup by comparing it against measurements from two commercially available table top gonio-spectrophotometers. The image based setup uses an RGB camera to perform bidirectional measurements of the sample material. We use a conversion matrix to calculate luminance from the captured data. The matrix is calculated using camera spectral sensitivities that are measured with a monochromator. Radiance factor of the sample material is measured using commercially available tabletop gonio-spectrophotometer and compared against measurements made using the image based setup in the colorimetric domain. Our measurement setup is validated by comparing the measurements performed using a gonio-spectrophotometer. Uncertainty and error propagation is calculated and taken into account for validation. The sample material measured is wax based ink printed on packaging paper substrate commonly used in print and packaging industry. Results obtained show that the image based setup can perform bidirectional reflectance measurements with a known uncertainty. The gonio-spectrophotometer measurements lie within the uncertainty of the measurements performed by the image based measurement setup. The setup can be used to perform bi-directional reflectance measurements on samples with properties similar to the samples used in this article.

OCIS codes: *330.0330, 330.1710*

http://dx.doi.org/10.1364/ao.XX.XXXXXX

1. INTRODUCTION

The quality of an object is often judged by its total appearance. To describe the physical correlates to the total appearance of an object (whether it is food, textile, skin, chemicals, coatings, metals, paper, plastics) optical properties are measured. The overall appearance of an object/material is resulting from a combination of its chromatic attributes (colour described in terms of lightness, hue, and saturation) and its geometric attributes (like gloss, translucency and texture) [1].

In recent years, various technologies (like effect inks [2] or conventional inks printed on metallic foils [3]) have been introduced particularly in the packaging industry to create appearance effects. These inks, however, cannot be described well enough by conventional measurements using a single measurement geometry.

For such materials the reflection of light is not satisfactorily modelled as, e.g., a lambertian surface where the intensity of the light is proportional to the cosine of the reflection angle. They produce a desirable appearance by changing their perceived colour or lightness properties with a change in illumination and viewing direction [4]. In order to characterise and reproduce such a material, reflectance measurements are performed at different illumination and viewing directions [4]. Back in 2007, Takagi et al. [5] stated that to characterise the reflection properties of special effect coatings, measurements taken at as many as 1485 different measurement geometries are required. It is practically very difficult to perform these measurements and use such a huge data for processing. Krichner and Werner [6] demonstrated that a reduction in number of measurement geometries is essential and is possible with physical interpretation of the amount of light reflected at different measurement geometries. A recent study made by Ferrero et. al [7], to characterise the color shift of special effect coatings shows that a maximum of 10 geometries could be sufficient.

For traditional colour pigments that are printed on diffuse paper substrates, traditional measurement geometries recommended by CIE [8] are sufficient to characterise the materials in a way that correlates well with how the colour of the material

is perceived. In graphic arts and print industry, measuring instruments with 45°:0° geometry are widely used for reflectance measurement of materials. Sphere based geometries are mainly used in the paint, textile and plastic industries. For non-diffuse materials like metallic inks the incident light is specularly reflected. ASTM standards [9, 10] recommend the illumination and viewing directions for measurement of a few different types of the non-diffuse materials. Integrating sphere based measurement instruments are often used to measure non-diffuse samples. However, using an integrating sphere based instrument is not sufficient as it captures an average colorimetry of the sample and not the detailed angular variation of the reflected light. According to [4, 11], using the traditional single geometry measurement instruments are also non-sufficient to measure and characterise such non-diffuse materials. Measurements made at more than one illumination and viewing directions are therefore required to characterise such materials.

Instruments measuring at a few selected multiple fixed directions are termed as multi-angle spectrophotometer [12] whereas instruments that are used for measurements over a broad range of angles are called gonio-spectrophotometers. In this article, we adopt the terminology 'gonio-spectrophotometer' to describe any instrument that performs measurements at more than one illumination and viewing direction.

A number of gonio-spectrophotometers are commercially available and widely used to perform measurements at different illumination and viewing directions [13]. These instruments measure the sample material spectrally at different illumination and viewing directions. The measurement quantity obtained is the ratio of the reflected and incident power ($\Phi_r / \Phi i$). Using this measurement quantity the bidirectional reflectance distribution function (BRDF), f_r of the material can be computed. Spectral radiant power and the corresponding radiometric terms required to express a BRDF are well defined and can be referred in [14], and the BRDF is defined by Nicodemus et. al [15] as:

$$f_r(\theta_i, \phi_i, \theta_r, \phi_r, \lambda) = \frac{dL_r(\theta_i, \phi_i, \theta_r, \phi_r, \lambda)}{dE_i(\theta_i, \phi_r, \lambda)} \quad \textbf{(1)}$$

where, $L_r(\theta_i, \phi_i, \theta_r, \phi_r, \lambda)$ is the reflected radiance in the direction (θ_r, ϕ_r), and $E_i(\theta_i, \phi_r, \lambda)$ is the irradiance from the direction (θ_i, ϕ_i). The illumination and viewing direction are described relative to the surface normal, socalled 'anormal angle', in agreement with the ASTM E2175-01 [12] standard and the CIE 175 [16] technical report.

A gonio-spectrophotometer can measure at a broad number of illumination and viewing angles, but, are slow. One of the main reasons for this is that they require the sample material to be measured lying flat while the detector and the light source or the sample rotates to perform bidirectional measurements. The geometrical calibration for the detector and light source or sample surface rotation, and the spectral calibration of the incident light source contributes heavily to the measurement time of the instrument.

In order to overcome these drawbacks, image based measurement setups have been proposed and presented in the past [17] to perform bidirectional measurements of flexible thin materials like print and packaging paper or plastic. Our setup used in this study can perform measurements fast (in a single shot) and inline with production of such print and packaing materials which can be an advantage against gonio-spectrophotometers. Guarnera et. al [18] provided an overview of measuring instruments that are used for bidirectional measurements.

Sole et. al [19, 20] uses such a setup to measure thin flexible materials (printed packaging paper). The measured data is then used to train different reflection models (for example Cook-Torrance). In [21], Sole et al. trained two reflection models with measurement data captured using the image based measurement setup described in [19, 22]. One of the sample material was also measured using a Minolta CS1000 tele-spectro-radiometer (TSR) at 4 different viewing directions for a given illumination direction. Using the trained reflection models, CIEXYZ Y value for the sample material was estimated at these 4 viewing directions for the given illumination direction. These estimated CIEXYZ Y values were then compared with the TSR measured CIEXYZ Y values. It was observed that the measurements performed using the TSR were not precise in terms of geometrical conditions (illumination and viewing angles). Also the measurements used for training the reflection models and to test, were generated from the same setup.

Although several image-based setups have been proposed in the past, it is not well established how accurately they perform in comparison with gonio-spectrophotometers. In this article, we use an the existing image based measurement setup from [19] and compare the results with two commercially available gonio-spectrophotometers by transforming the results into a common domain. This is performed for printed packaging paper material samples. We use the terminology 'our measurement setup' when referring to the image based setup from [19]. Secondly, we investigate the accuracy of the image-based setup by means of a propagation-of-error analysis.

2. METHOD

In this article we evaluate image based measurement setup used in [19] using commercially available gonio-spectrophotometer for bidirectional measurements of thin flexible materials. 4 material samples (from print and packaging industry) named LightCyan (LC) and LightMagenta (LM), Cyan (C) and Magenta (M) are measured using our measurement setup and two commerically available gonio-spectrophotometers PerkinElmer's *LAMBDA1050* (referred as '*LAMBDA1050*') and Murakami's GCMS-3B Gonio-Spectrophotometric Color Measurement Systems (referred as '*GCMS*'). To evaluate our measurement setup, we use sample materials printed on matt coated paper with wax based inks using an OCE ColorWave600 plotter. Spectralon tile was measured with *LAMBDA1050* and captured with our measurement setup along with the samples. As the samples were solid colour patches printed on packaging paper material, they are homogeneous and flexible.

A. Measurements

Out of the four samples, two samples, LightCyan (LC) and LightMagenta (LM), were measured using *LAMBDA1050* while samples Cyan (C) and Magenta (M) were measured using *GCMS*. The spectralon tile (ST) was measured using *LAMBDA1050* along with LC and LM samples. Appendix describes both the gonio-spectrophotometers of their design and measurement output.

For *LAMBDA1050*, the measurement output is the ratio of reflected radiant flux to incident radiant flux ($\Phi_r / \Phi i$). Radiance factor (β_r) is calculated from the measured output using Equation (2) [23].

$$\beta_r(\lambda) = \frac{\Phi_r(\lambda)}{\Phi_i(\lambda)} \cdot \frac{\pi}{\omega_r \cos\theta_r} \quad \textbf{(2)}$$

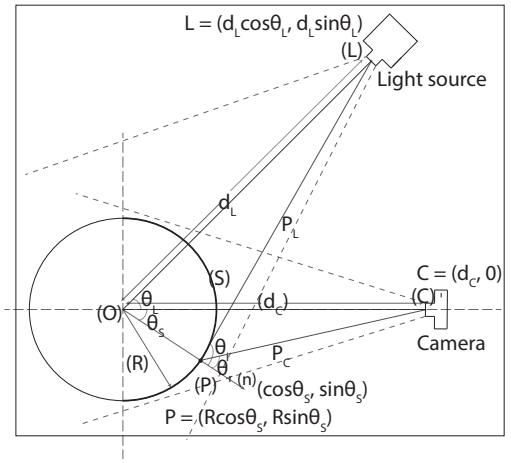

Fig. 1. Measurement setup in a vector plane [Image reproduced with permission [19]]

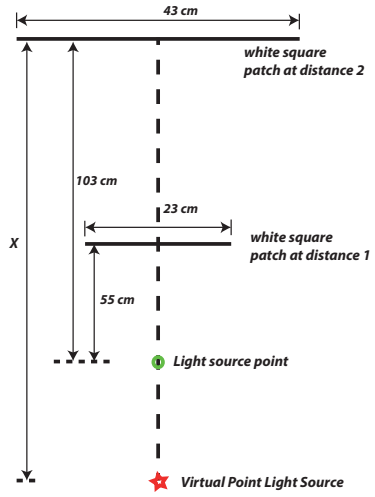

Fig. 2. Virtual point light source calculation

where, ω_r is the detector solid angle, and θ_r is the anormal viewing angle.

The measurement output of *GCMS* is the radiance factor (β_r). The BRDF can further be calculated using $f_r = \frac{\beta_r}{\pi}$ relation.

Our measurement setup uses a point light source and a commercially available digital camera as a detector. The light source and the detector is at a fixed position from the sample (for example light source at 45° and detector at 0°) and the measurement sample is curved onto a cylinder of known radius. Figure (1) shows the setup in a vector plane. As described in [19] and referring to Figure (1), point *C* is the detector position (digital camera position) approximately at the center of the curved sample at a distance d_C. *L* is a point light source illuminating the sample at a fixed angle $\theta° < \theta_L < 90°$ at a known distance d_L from the center of the curved sample. Assuming that the curved sample is homogeneous, light incident and reflected at any given point on the sample provides information with respect to the light source position (*L*), camera (*C*) and the surface normal vector (**n**) at point *P*. θ_i and θ_r are incident and reflection angles with respect to the normal **n** at a given point (*P*). Considering the setup in a vector plane, θ_i and θ_r are calculated as given in Equation (3)

$$\cos\theta_i = \frac{\mathbf{P_L}\cdot\mathbf{n}}{|\,P_L\,|},\ \cos\theta_r = \frac{\mathbf{P_C}\cdot\mathbf{n}}{|\,P_C\,|} \tag{3}$$

As the measurements are performed using a digital camera, each pixel in the captured image corresponds to point (*P*) on the curved sample surface. As each point (*P*) (on the sample) makes a corresponding incident (θ_i) and reflection (θ_r) angle with respect to the normal (**n**) at point (*P*), the information recorded by each pixel corresponds to a bidirectional measurement at point (*P*).

As discussed in [22], the captured image records the light information in digital values for each camera sensor. The measured camera spectral sensitivities ($r(\lambda)$, $g(\lambda)$, $b(\lambda)$) along with CIE 2° colour matching functions ($\overline{x}$, $\overline{y}$, $\overline{z}$) are used to calculate a 3×3 matrix, $\hat{M}$. Using $\hat{M}$, the captured RGB data can be converted into a colorimetric space (CIEXYZ).

Samples LC, LM and ST, were measured at three anormal incident ($\theta_i = 25°, 35°, 45°$) and 26 anormal reflection angles (ranging between $\theta_r = [+75°, -75°]$ at 5° intervals) using *LAMBDA1050*. A ratio of the reflected radiant flux to incident flux (Φ_r/Φ_i) in the range of 380 nm to 730 nm at 10 nm intervals was recorded. We calculate the radiance factor using equation (2). The distance between the sample and the detector was 91 mm, while the detector aperture area was 12.7 mm x 15.5 mm thus giving a solid angle (ω_r) of 0.0237 sr [24].

Similarly, samples C and, M were measured using *GCMS*. Spectral radiance factor is recorded in the range of 390 nm - 730 nm at 10 nm interval at anormal incident (θ_i) and reflection (θ_r) angles in the range of $[+80°, -80°]$ at 5° intervals.

In our measurement setup, sample is illuminated using a tungsten point light source, and was captured using a 16 bit Nikon D200 DSLR camera. As a point light source we use a film projector (consisting of a halogen tungsten lamp). As the projector uses a focusing lens, using inverse square law we calculate the origin of the point light source by illuminating a white patch at 2 distance intervals and measure the illuminated area of the white patch and distance between the projector and the illuminated surface. Figure 2 shows a schematic diagram of the setup and measurements. Referring to Figure 2, distance x is calculated as 103.2 cm. The homogeneity of the light source was checked by measuring the incident light at different parts of the given sample area. The incident beam was homogeneous with a variation of approximately 7.2% across an area of size 10cm x 5cm at the sample surface.

As a white reference, ST is used in the setup. Illumination and viewing angles are calculated for each pixel point (p) that corresponds to the given point (*P*) on the curved sample. As discussed in [19], for a given illumination direction (θ_L), the number of viewing directions that we can measure will depend on the sample curvature, resolution of the digital camera used as detector and the distance between the curved sample and the detector. Also, as we measure the curved sample at different illumination directions (θ_L), the area illuminated on the curved sample

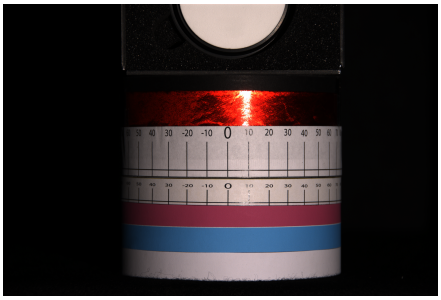

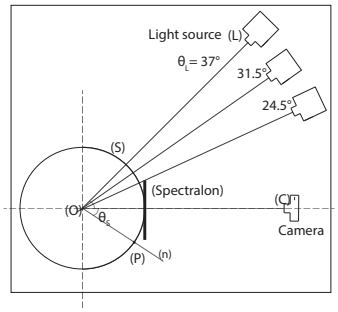

Fig. 3. LC and LM sample measurement at 3 different illumination directions (θ_L) and image captured at $\theta_L = 24.5°$

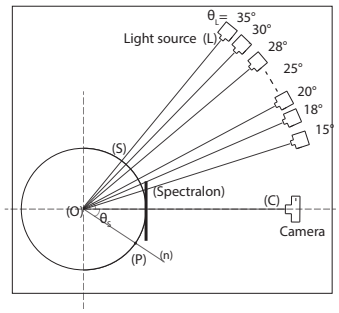

Fig. 4. Sample measurement at 7 different illumination directions (θ_L) and image captured at $\theta_L = 15°$

changes with change in θ_L. It is therefore important to consider the viewing angles in the area which is uniformly illuminated with all the illumination directions for further processing and comparison.

LC and LM samples were measured at three different illumination directions (θ_L = 24.5 °, 31.5 °, 37 °) using our measurement setup (refer Figure 3). Figure 3 shows the image captured at $\theta_L = 24.5°$. C and M samples were measured at seven different illumination directions (θ_L = 15 °, 18 °, 20 °, 25 °, 28 °, 30 °, and 35 °) (refer Figure 4). Figure 4 shows the image captured at $\theta_L = 15°$. As can be seen from the image along with these two samples, five additional samples were measured using our measurement setup, however, it was not possible to have them measured using any of the gonio-spectrophotometers. We therefore use two samples (M and C) in the analysis and comparison. Table 5 gives an overview of the measurement angles and the instruments with which the samples were measured. Figures 6 and 7 show θ_i and θ_r angles at which the samples were measured using both the gonio-spectrophotometers and our measurement setup. Please make a note that GCSM gonio-spectrophotometer measures at 1 ° near specular angles while at 5 ° intervals away from the specular direction.

The camera records a 16 bit raw RGB image. To correct for dark current noise we subtract a dark image (captured with camera lens cap on in a dark room) from the captured image. Five vertical pixels from the sample center for the given point (P) are averaged. Camera settings have been similar while measuring the camera spectral sensitivities and while measuring the samples.

In radiometric terms, the 16 bit raw RGB data recorded corresponds to the radiance exited from the curved sample surface (as we work at a constant exposure time, the RGB data recorded corresponds to radiance). To compare the measurements made using our measurement setup and gonio-spectrophotometers, we need to either calculate spectral radiance factor from the raw RGB data measurements, or vice versa.

Using the BRDF definition, the radiance exited from the sample surface can be calculated using the sample BRDF measured by the gonio-spectrophotometer. For a small homogeneous area, spectral radiance reflected from the sample surface in a given direction can be defined as given in Equation (4).

$$L_r(\theta_i, \phi_i, \theta_r, \phi_r, \lambda) = f_r(\theta_i, \phi_i, \theta_r, \phi_r, \lambda) \cdot E_i((\theta_i, \phi_i, \lambda) \quad \textbf{(4)}$$

where, $L_r(\theta_i, \phi_i, \theta_r, \phi_r, \lambda)$ is the spectral radiance exited from the sample, $E_i((\theta_i, \phi_i, \lambda)$ is the spectral irradiance at the sample, and f_r is the sample BRDF (obtained from the gonio-

Measurement device	Data recorded	Samples measured				
		ST	LC	LM	C	M
Measurement setup	*Camera RGB*	*3 + 7 direc* (θ_L)	*3 direc* (θ_L = 24.5°, 31.5°, 37°)		*7 direc* (θ_L = 15°, 18°, 20°, 25°, 28°, 30°, 35°)	
LAMBDA1050	*Spectral BRDF*	θ_i = 25°, 35°, 45°			-NM-	
		θ_r = [−75°, +75°] *at* 5° *interval*				
GCSM		-NM-			$\theta_i = \theta_r$ = [−80°, +80°] *at* 5° *interval*	
-NM- = Could not be measured						

Fig. 5. Overview of measurement angles and sample measurement

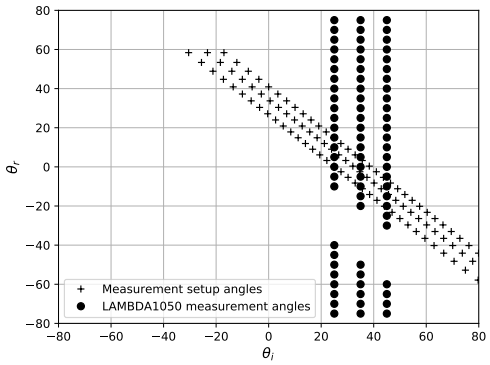

Fig. 6. θ_i and θ_r angles at which *LAMBDA1050* and our measurement setup measured

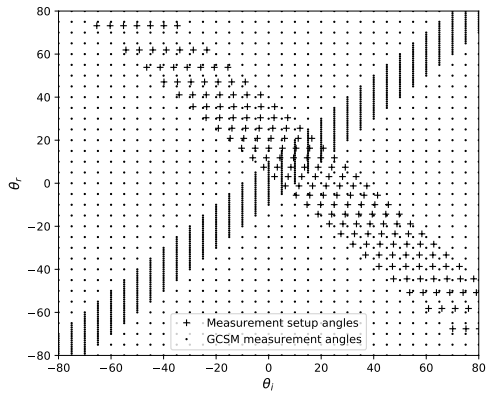

Fig. 7. θ_i and θ_r angles at which *GCMS* and our measurement setup measured

spectrophotometer measurements). Considering inplane measurements, we re-write Equation (4) using the inverse square law as,

$$L_r(\theta_i, \theta_r, \lambda) = f_r(\theta_i, \theta_r, \lambda) \cdot \frac{I_i(\lambda) \cdot \cos\theta_i}{\omega_s \cdot d^2} \tag{5}$$

where $L_r(\theta_i, \theta_r, \lambda)$ and $f_r(\theta_i, \theta_r, \lambda)$ are as described above in Equation (4) for inplane measurements, $I_i(\lambda)$ is radiant intensity incident normally on the sample, θ_i is anormal incident angle made by the light source relative to the normal at the sample surface, d is distance between sample surface and point light source, and ω_s is the solid angle at the curved sample surface made by the incident light.

In Equation (5), $f_r(\theta_i, \theta_r, \lambda)$ can be measured using a gonio-spectrophotometer. The incident spectral light intensity, $I_i(\lambda)$ (in our measurement setup), can be calculated using a reference white diffuser such as a Spectralon tile who's BRDF is known for a given θ_i and θ_r and assuming that this reference white diffuser is lambertian. Distance d, will be the distance between point (P) on the curved sample and the point light source in our measurement setup. ω_s will be the solid angle, defined as the ratio of illuminated surface area and square of the distance between the curved surface and light source. We calculate these terms as described below.

Incident spectral light intensity, $I_i(\lambda)$, is estimated using relative normalisation method [25]. The spectralon (ST) BRDF measured with *LAMBDA1050* at $\theta_i = 25°$ and $\theta_r = 0°$ is used for the same. Re-writing Equation (5), incident spectral light intensity can be calculated using Equation (6).

$$I_i(\lambda) = \frac{L_{r,spec(\theta_i=25°,\theta_r=0°,\lambda=380nm-730nm)} \cdot d^2}{f_{r,spec(\theta_i=25°,\theta_r=0°,\lambda=380nm-730nm)} \cdot \cos\theta_i} \tag{6}$$

where $L_{r,spec}(\theta_{i=25°}, \theta_{r=0°}, \lambda_{380nm-730nm})$ is the spectral radiance exited from the spectralon surface and $f_{r,spec}(\theta_{i=25°}, \theta_{r=0°}, \lambda_{380nm-730nm})$ is the spectral BRDF of the spectralon measured with *LAMBDA1050*, at the given incident ($\theta_{i=25°}$) and reflection ($\theta_{r=0°}$) angle. θ_i and d are the same as defined in Equation (5).

The *distance (d)*, is the distance P_L in our measurement setup vector space (refer Figure 1). d can therefore be calculated using the coordinate values for point P on the curved sample surface and point light source L. We solve for distance P_L (refer Equation (7)) where, d_L is the distance between point light source (L) and origin (O), R is the radius of the cylinder on which the sample is curved, θ_L is the illumination direction angle and θ_S is the angle made by point (P) on the curved sample surface with vector **OC**.

$$\begin{aligned} \mathbf{P}_L &= [P, D] \\ \mathbf{P}_L &= \mid P_L \mid = \sqrt{d_L^2 + R^2 - 2d_L R\cos(\theta_L - \theta_S)} \end{aligned} \tag{7}$$

The *solid angle,* ω_s, can be calculated using the illuminated area and distance between the illuminated sample area and the light source. The distance between the illuminated sample area and the light source is calculated using Equation (7) at each point (P) on the curved sample surface. As we use a film projector to illuminate the curved sample, the area illuminated by the point light source will correspond to the physical area on the curved surface covered by each camera pixel.

To calculate the physical area covered by each pixel on the curved sample surface, we ignore errors due to lens structure in the camera and assume that each pixel of the camera makes same solid angle (ω_r) with respect to the captured image and

the pixel location on the camera sensor. We capture an image of a white patch with the camera that is used in our measurement setup. Assuming the image of the white patch as a single pixel, the solid angle ω_r formed by the camera with respect to the area of the white patch is as given in Equation (8). A_{sq} is the physical area of the white patch (in mm) and d is the distance between the camera and the white surface (in mm).

$$\omega_r = \frac{A_{sq}}{d^2} = \frac{(20 \times 25)}{490^2} = 0.00208\ sr. \tag{8}$$

Dividing the solid angle with the total number of pixels gives us the solid angle (ω_{r_p}) for each pixel. As distance P_L is known for each point (P) on the curved sample surface, ω_s can be calculated using the surface area covered under each pixel. ω_s remained constant over the pixel position (corresponding to the point P on the sample surface) and therefore was taken into account while calculating $I_i(\lambda)$.

Referring the vector space in Figure 1, distance P_C between the detector and the sample surface is calculated using Equation (9). Note that P_C will change with the location on the sample surface as it is curved due to wrapping around a cylinder of radius R.

$$\begin{aligned} \mathbf{P}_C &= [P, C] \\ \mathbf{P}_C &= \mid P_C \mid = \sqrt{d_c^2 + R^2 - 2Rd_c \cos\theta_s} \end{aligned} \tag{9}$$

where d_C is the distance between the camera (C) and origin (O), R is the radius of the cylinder on which the sample is curved, and θ_S is the angle made by point (P) on the curved sample surface with vector **OC**. As we now know the distance between the camera and the sample surface and the solid angle each camera pixel makes, the physical area covered by each pixel can be calculated using the relation ($Area = \omega \cdot distance^2$).

To compare the measurements, for simplicity of calculations we convert the sample BRDF to camera RGB values. Referring Equation (4), we use the irradiance at the sample surface in our measurement setup to calculate the radiance at the sample surface for the incident (θ_i) and reflection (θ_r) directions at which the sample BRDF is measured using a gonio-spectrophotometer. The light incident on the sample surface, $I_i(\lambda)$, is calculated using Equation (6). The spectralon BRDF $f_{r,spec}(\theta_{i=25^\circ}, \theta_{r=0^\circ}, \lambda_{400-700})$ is measured using *LAMBDA1050* while the spectralon surface radiance $L_{r,spec}(\theta_{i=25^\circ}, \theta_{r=0^\circ}, \lambda_{400-700})$ is measured using a telespectroradiometer (TSR) in our measurement setup. The camera is replaced by the TSR in our measurement setup to measure the radiance. As the remaining parameters of the Equation (5) are known, we can calculate radiance at the sample surface.

As we compare measurements made using two methods, one being radiance L_r, a physical quantity, while other is camera RGB, a relative value, the measured data should be calibrated to the incident light intensity in the setup. We scale the incident light intensity using a camera coefficient g as given in Equation (10). $L_{r,spec}$ is the radiance measured at the spectralon surface at $\theta_{i=25^\circ}, \theta_{r=0^\circ}, \lambda_{400-700}$ by replacing the camera with a TSR in our measurement setup, while $\bar{g}(\lambda)$ is the spectral sensitivity of the camera green sensor.

$$g = \sum_{\lambda=400}^{700nm} \bar{g}(\lambda) \cdot L_{r,spec}(\lambda) \Delta\lambda_{10nm} \tag{10}$$

Using the BRDF measurements of the sample (measured using a gonio-spectrophotometer), and the scaled incident light intensity ($I_i(\lambda)/g$), the radiance at the sample surface (for the incident (θ_i) and reflection (θ_r) angles at which the BRDF is measured) is calculated using Equation (11).

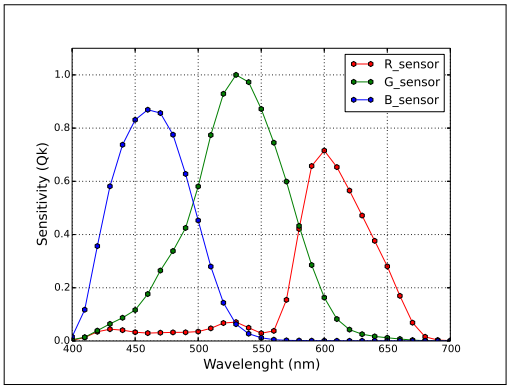

Fig. 8. Camera sensor sensitivity functions [22].

$$L_r(\theta_i, \theta_r, \lambda) = f_r(\theta_i, \theta_r, \lambda) \cdot \frac{I_i(\lambda)}{g} \cdot \frac{\cos\theta_i}{\omega_s \cdot d^2} \tag{11}$$

The radiance obtained, is then converted to camera RGB values using Equation (12), where $L_r(\theta_i, \theta_r, \lambda)$ is the radiance at the sample surface in our measurement setup calculated using Equation (11) (but for the incident and reflection angles used in gonio-spectrophotometer measurements) and ($\bar{r}$, $\bar{g}$, $\bar{b}$) are spectral sensitivities of camera used as a detector in our measurement setup.

$$\begin{pmatrix} Cal_R(\theta_i, \theta_r) \\ Cal_G(\theta_i, \theta_r) \\ Cal_B(\theta_i, \theta_r) \end{pmatrix} = \begin{pmatrix} \sum L_r(\theta_i, \theta_r, \lambda) \cdot \bar{r} \\ \sum L_r(\theta_i, \theta_r, \lambda) \cdot \bar{g} \\ \sum L_r(\theta_i, \theta_r, \lambda) \cdot \bar{b} \end{pmatrix} \tag{12}$$

A point to note here is that when measuring the sample material using a gonio-spectrophotometer, measurements are performed at fixed incidence (θ_i) and reflection (θ_r) angles, while the measurement setup uses a camera, thus capturing the reflected radiance from the sample surface per pixel. In our measurement setup, each pixel corresponds to the point (P) on the curved sample surface that makes an unique incident (θ_i) and reflection (θ_r) angle relative to the surface normal. Using a hight resolution camera, the θ_i and θ_r combination is high and different compared to the gonio-spectrophotometer measurements. It records approx. 1000 pixels (horizontally) for each sample.

Another point to note here is that total number of pixels will vary depending upon the radius of the cylinder on which the sample is curved, the distance between the sample and the camera, and the resolution of the camera used in our measurement setup. This data, therefore, being too dense, we use information captured at every 50^{th} pixel for comparison. Depending on the sample material being measured and the interval between the angles required, the pixel interval can be increased or decreased.

We interpolate camera RGB measurements that are calculated using gonio-spectrophotometer measurements using Equation (12) at the incident and reflection angles of our measurement setup. Interpolation is performed using a standard piecewise cubic spline interpolation.

B. Measurement error

Measurement setup has three main components: a camera (as a detector), a point light source (to illuminate the sample), and the sample to be measured (wrapped around a cylinder of known radius). We calculate the incident and reflection angle made by point (P) on the sample with respect to the light direction and the camera position from the curved sample. The incident and reflection angle calculations are therefore dependent on θ_L (light direction with respect to normal to the camera), cylinder radius (R) on which the sample is wrapped, distance (d_L) between curved sample and point light source, distance (d_c) between curved sample and camera, pixel position (d_p) on the camera with respect to point P on the curved sample surface and effective camera focal length (F_p). Also, our measurement setup uses a RGB camera as a detector. The camera used in the setup (Nikon D200) records raw RGB data for the radiance exited from the sample surface. We convert this data to CIE XYZ values using a conversion matrix ($\hat{M}$). As discussed in [22], $\hat{M}$ is derived using camera sensitivity measured with a monochromator and CIE 2° colour matching functions. Figure 8 shows the sensitivites (measured using the monochromator) of the camera used in our measurement setup. Calculating CIEXYZ values with $\hat{M}$ introduces error in the colorimetric values. It is therefore important to take into account the uncertainty (in terms of measurement error) in these calculations when comparing with the gonio-spectrophotometer measurements.

We derive error uncertainty in calculating incident (θ_i) and reflection (θ_r) angles using the procedure given by the Joint Committee for Guides in Metrology (JCGM) [26].

$$\Delta\theta_{S_{edge}} = \sqrt{\left(\frac{\partial\theta_{S_{edge}}}{\partial d_C}\cdot\Delta d_C\right)^2 + \left(\frac{\partial\theta_{S_{edge}}}{\partial R}\cdot\Delta R\right)^2}$$

$$\frac{\partial\theta_{S_{edge}}}{\partial d_C} = \frac{-1}{\sqrt{\left(1-\left(\frac{d_C}{R}^2\right)\right)}}\cdot\frac{1}{R} \tag{13}$$

$$\frac{\partial\theta_{S_{edge}}}{\partial R} = \sqrt{\left[\frac{-\Delta d_C}{R\cdot\sqrt{1-\left(\frac{d_C}{R}\right)^2}}\right]^2 + \left[\frac{d_C\cdot\Delta R}{R^2\cdot\sqrt{1-\left(\frac{d_C}{R}\right)^2}}\right]^2}$$

Equation (13) shows the uncertainty in calculating $\theta_{S_{edge}}$. Calculations of $\theta_{S_{edge}}$ can be referred in [19]. $\theta_{S_{edge}}$ is the θ_S angle at the edge of the curved sample when viewed from the camera field of view. In the same way, uncertainty in θ_i, θ_r, θ_S and F_P is derived and is approximated for the physical measurements Δd_L, Δd_C, $\Delta\theta_S$, ΔR and $\Delta\theta_L$. Equation (14) calculates the error in CIE Y calculation using values that are calculated using

- $\hat{M}$ and RGB values calculated using Equation (12) and,
- L_r calculated using Equation (11) and CIE 2° colour matching functions.

$$\Delta Y = \frac{\sqrt{(Y_{(\hat{M}-RGB)} - Y_{(L_r-CIE2^\circ)})^2}}{Y_{(L_r-CIE2^\circ)}} \tag{14}$$

The two samples LightCyan (LC) and LightMagenta (LM), and the spectralon tile (ST) were measured using *LAMBDA1050* at three anormal incident ($\theta_i = 25^\circ, 35^\circ, 45^\circ$) and 26 anormal reflection angles (ranging between θ_r= [+75°, −75°] at 5° intervals) while two samples Cyan (C) and Magenta (M) using *GCMS* in the range of θ_i=θ_r=[+80°, −80°] at 5° intervals. All the samples were measured using our measurement setup at different incident light directions (θ_L).

We interpolate measurements conducted with gonio-spectrophotometer at angles (θ_i and θ_r) measured at by our measurement setup. Point to note hear is that the measurements we interpolate here are camera RGB values converted (using Equation (12)) from the BRDF measurements performed by the gonio-spectrophotometers. CIEXYZ values were further calculated from the interpolated RGB measurements using the conversion matrix ($\hat{M}$). The spectralon tile measurements at θ_L=25° was used as reference white measurement with CIE Y value as 1.0.

To evaluate the setup we analyse the calculated CIE Y value (hereby referred as luminance value). Relative ΔY error is calculated for each sample between the gonio-spectrophotometer and measurement setup measurements using Equation (15).

$$Error_{\Delta Y} = \frac{\sqrt{(Y_{Gonio} - Y_{Setup})^2}}{Y_{Gonio}} \tag{15}$$

where, Y_{Gonio} is the luminance value calculated using measurements performed by the gonio-spectrophotometer and Y_{Setup} is the luminance value calculated using the measurements from our measurement setup of the respective sample material.

3. RESULTS

Table 1 shows the uncertainty derived and approximated for our measurement setup parameters. Table 2 shows the uncertainty in CIE Y calculations.

Table 1. Measurement uncertainty in our measurement setup parameters

	Setup parameters	Uncertiainty
Calculated	θ_i	±7.6°
	θ_r	±7.4°
	θ_S	±6.7°
	F_P	±1973 pixels
Approximated	R	±5 mm
	d_C	±10 mm
	d_p	±5 pixels
	d_L	±20 mm
	θ_L	±4°

Table 2. Error (ΔY) in CIE Y calculation

Sample	LC	LM	C	M
ΔY	0.11	0.12	0.18	0.13

The average $Error_{\Delta Y}$ for each sample material is calculated (refer Table 3). Figure 9 - 12 shows the calculated luminance for the samples against the reflection angles at respective incident

Table 3. $Error_{\Delta}Y$ **between luminance calculated using measurements from our measurement setup and gonio-spectrophotometer**

Instrument	θ_L	LC sample	LM sample
LAMBDA1050	24°	0.12	0.01
	34°	0.14	0.01
	44°	0.18	0.15
	Average	0.14	0.05
Instrument	θ_L	C sample	M sample
GCSM	15°	0.21	0.19
	18°	0.21	0.19
	20°	0.21	0.20
	25°	0.22	0.21
	28°	0.24	0.22
	30°	0.27	0.22
	35°	0.32	0.29
	Average	0.24	0.21

light direction along with the measurement uncertainty in calculating the angles and CIE Y values. Note that as the number of incident light directions (θ_L) used and samples measured being many when comparing against GCSM measurements, we show results for the meausred samples at one incident directions ($\theta_L = 35°$). For comparison with *LAMBDA1050* measurements we show results for both the samples (*LC*, *LM*) for one incident light direction ($\theta_L = 44°$).

Looking at the plots we can observe that the measurements performed using the gonio-spectrophotometers lie within a known uncertainty of our measurement setup for the samples used in this study.

4. DISCUSSION

Samples LM and LC were measured at three incident angles (θ_i) using *LAMBDA1050* and three light direction (θ_L) in our measurement setup. Due to measurement setup limitations and the limited measurements from *LAMBDA1050*, the measurement region of overlap in terms of θ_i and θ_r were limited (refer Figure 6). It was therefore possible to compare only a limited number of measurements for the LC and LM samples. Point to note here is that we perform a relative comparison using BRDF measurement of the spectralon tile (at θ_i=25°, θ_r=0°) to normalise both the measurements. Similar comparison is done for the C and M samples measured with *GCMS*. With *GCMS*, it was possible to measure the entire plane for incident and reflection angles at 5° interval (refe Figure 7). Same samples were measured at seven different incident light directions (θ_L) using our measurement setup in order to have a bigger overlap in the measurement region (with respect to θ_i and θ_r directions) compared to the measurements performed using *LAMBDA1050* for LC and LM samples. The average ΔY between the measurements was highest for the C sample compared to other samples. The measurement setup we evaluate in this article has different components. We calculated the error in incident and reflection

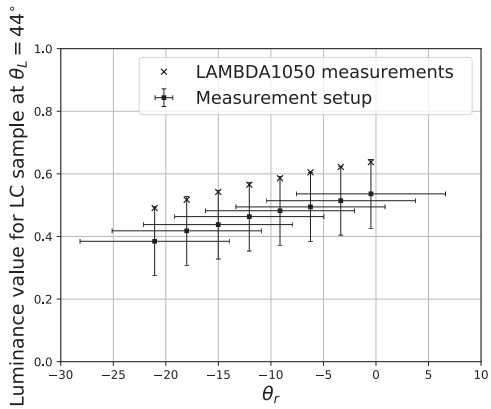

Fig. 9. Calculated luminance (Y) values for LC sample for measurements at $\theta_L = 44°$,using our measurement setup and *LAMBDA1050* against θ_r

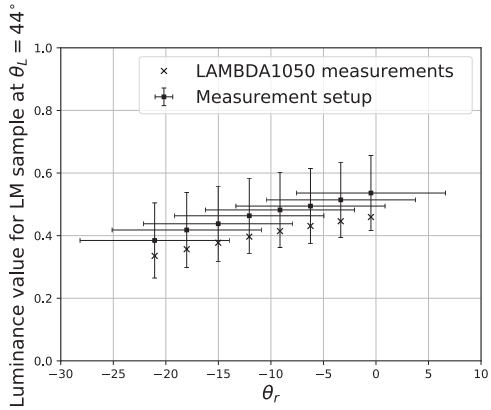

Fig. 10. Calculated luminance (Y) values for LM sample for measurements at $\theta_L = 44°$,using our measurement setup and *LAMBDA1050* against θ_r

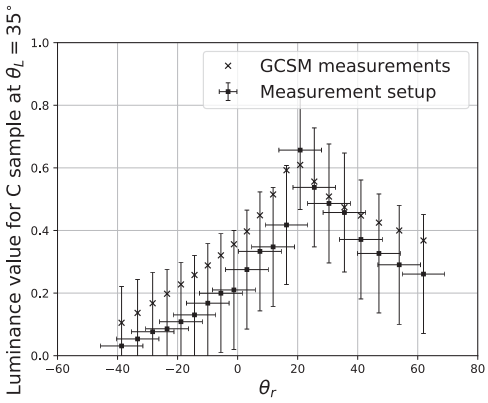

Fig. 11. Calculated luminance (Y) values for C sample for measurements at $\theta_L = 35^\circ$,using our measurement setup and *GSCM* against θ_r

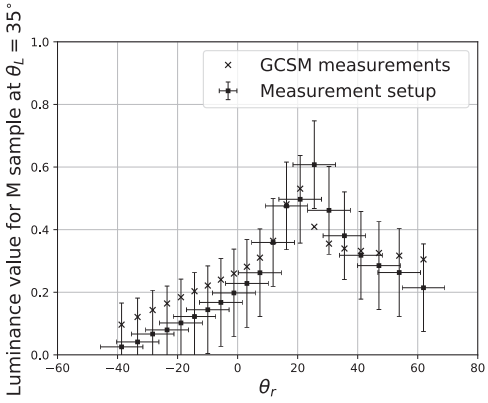

Fig. 12. Calculated luminance (Y) values for M sample for measurements at $\theta_L = 35^\circ$,using our measurement setup and *GSCM* against θ_r

angle calculations and, CIEXYZ calculations from the camera RGB.

Error in physical measurements (cylinder radius (R), distance between the curved sample and the detector (d_C), distance between the curved sample and the light source (d_L), and angles between d_C and d_L (θ_L)) contribute to the error in estimating the incident and reflection angles at point (P) on the curved sample surface. The uncertainty in estimating θ_i and θ_r is large. We observed that the uncertainty in calculating θ_i and θ_r angles is more sensitive to physical measurements d_C, d_L and θ_L compared to the radius (R) of the cylinder.

To calculate colorimetric values we use the conversion matrix ($\hat{M}$) along with camera measurements. $\hat{M}$ is calculated using least square error between the camera sensitivity functions and the CIE 2° colour matching functions. Depending on the colour of the sample being measured, conversion from camera RGB to CIEXYZ will introduce an error in the colorimetric values due to matrix ($\hat{M}$). We calculated this error by comparing the luminance (CIE Y) values calculated using a) the camera measurements and matrix ($\hat{M}$) and, b) radiance values and the colour matching functions.

Figures 9 – 12 show the comparison of measurements using the measurement uncertainty (in the form of error bars) of our measurement setup. An important point to understand from these plots is that as long as the measurements obtained from the gonio-spectrophotometer are within the uncertainty of our measurement setup, it should be possible to use our measurement setup to perform multi-angle BRDF measurements with a known uncertainty to measure materials similar to the sample material used in this study. Another point to consider is that we have not taken into account the measurement uncertainty of the gonio-spectrophotometers used in this study. Measurement uncertainty provided by the manufacturer of these instruments is usually for one incident and reflection angle and for one wavelength interval (for example θ_i= 45°, θ_r= 0°, λ=560 nm). To calculate the instrument uncertainty with the aim to compare with the camera setup, it would require a number of approximations to be made which would then add to the comparison error that would be difficult to eliminate. Also, it is expected that the gonio-spectrophotometers are much more accurate compared to our setup and therefore the uncertainty of our setup is calculated and analysed.

Looking at the results obtained for the samples used, luminance (CIE Y) measured using the gonio-spectrophotometer lies within the measurement uncertainty of our measurement setup For the LC sample measured at θ_L=44°, the error is maximum. Although similar observation can be made for C sample, the measurements are well within our measurement setup uncertainty. The possible reason for having a large error in the cyan samples is the camera sensor limitations in the blue spectrum. It is also observed that, as the incident light direction (θ_L) increases, we observe an increase in the error value between the measurements especially for LC and C samples but also for LM and M samples. Increasing θ_L contributes to the error due to geometrical calibration and uncertainty in physical measurements of the setup. Also, the sample being curved, bigger the θ_L, more are the incident and reflection directions for given point P on the sample surface.

From the plots (Figures 9 – 12) we can observe that the measurements performed using our measurement setup show lower CIE Y values compared to gonio-spectrophotometer measurements for LC and C samples. However, for LM sample our measurement setup measures a higher CIE Y compared

to the gonio-spectrophotometer measurements. For sample M, the measurements from our measurement setup and gonio-spectrophotometer do not follow a systematic curvature as seen for the other samples (LC, C and LM). The measurement setup measurements show a lower CIE Y value for reflection angles in an approximate range of -40° to 10° and a higher CIE Y value from approximately $\theta_r = 25^\circ$ to 40°.

The possible reason for such a systematic behaviour can be the error in calculating CIE Y value from camera RGB values using the conversion matrix $\hat{M}$. $\hat{M}$ is calculated using the camera spectral sensitivities and the CIE 2° colour matching functions. In the CIExyY colorimetric space, the camera sensitivity values will correspond to the points on the locus of the chromaticity diagram. The error in calculating CIE Y value from camera RGB will therefore depend on the colour sample being converted. These points needs a through investigation and will be future work for the authors.

From the achieved results can we question if this uncertainty is sufficiently low for a practical use of our measurement setup? The practical use will depend on a) the type of material being measured, b) the measurement accuracy required, and c) implications of the performed measurements. Given the measurement uncertainty, our measurement setup can be used by customers for fast measurements to understand bidirectional material properties and material visualisation. With the obatined uncertainty our measurement setup will not be suitable for precise measurements for applications like security, medical or measurement tracebility.

5. CONCLUSIONS

In this article, we evaluate an image based multi-angle measurement setup against commercially available table-top gonio-spectrophotometers for bidirectional measurements of flexible and homogeneous materials. We measure four samples using our measurement setup and two gonio-spectrophotometers at different incident and reflection directions.

Measurement setup can perform multi-angle BRDF measurements but with a large uncertainty. Gonio-spectrophotometer measurements lie within the measurement uncertainty of our measurement setup. The uncertainty in calculating θ_i and θ_r is large and more precise measurements of the physical parameters are required. Measurement setup can be used to measure (with known uncertainty) materials similar to the sample material used in this article. The setup can be used for fast multi-angle measurements however with a known uncertainty. Due to fast measurements using the setup, it can also help automate in-line multi-directional measurements during reproduction of packaging materials like the ones used in this study.

APPENDIX

PerkinElmer's *LAMBDA1050* gonio-spectrophotometer

PerkinElmer's LAMBDA1050 gonio-spectrophotometer contains ARTA accessory from OMT Solutions BV. The sample to be measured is illuminated with a monochromatic light. Light source used is a tungsten halogen light bulb. It is a double beam instrument, with the reference beam leading directly to the detector, thus measuring the incident radiant flux (Φ_i) in $watts$. It uses a double holographic grating monochromator to have a monochromatic light from the light beam incident on the sample. The sample is positioned on a rotating stage, and the angle of incidence (measured from the normal to the sample surface) is varied by rotating the sample using a motor The light reflected from the sample is detected with an integrating sphere detector of diameter 60 mm and consists of a photomultiplier tube as a detector. The detector revolves around the sample and can be positioned at angles relative to normal of sample surface, except for $\pm 10^\circ$ near the light source. The measurement output of this instrument is the ratio of reflected radiant flux to incident radiant flux. This instrument has been used previosuly [23] to study the angular variations in reflectance and fluroscence from paper that contain fluorescent whitening agents and fillers. Please refer *PerkinElmer's LAMBDA1050* manual [1] for details and specifications of *LAMBDA1050*.

Murakami's GCMS-3B Gonio-spectrophotometric Color Measurement System

Murakami's GCMS-3B Gonio-spectrophotometric Color Measurement System also has a double beam design wherein the radiant flux reflected from the sample material is continuously compared with against measurements made on a reference white diffuser plate. The light source is a tungsten halogen light bulb at a fixed position, while the detector (Silicon Photo-diode array) revolves around the sample within the range of anormal angles $\pm 80^\circ$ to the sample plane (when normal to the incident light). The sample to be measured is mounted on a flat plate which again rotates between anormal angles $\pm 80^\circ$ with respect to the incident light source normal to the sample plane. The light beam is divided into 2 identical beams using mirrors, lenses and heat filters to simultaneously illuminate the sample and the white reference plate. The instrument automatically corrects for the variation in intensity, and the area of illumination/viewing, due to the rotation of the plate and the detector. The measurement output of this device is radiance factor (β) measurement. As the reference white plate used in the measurement is assumed as a perfect reflecting diffuser, we can calculate the BRDF of the sample using $\beta = \pi \cdot f_r$ relation. Please refer to *Murakami's GCMS-3B Gonio-spectrophotometric Color Measurement System* manual[2] for details and specifications of this instrument.

ACKNOWLEDGMENT

We would like to thank and acknowledge support of Dr. Reiner Eschbach, Dr. Jean-Baptiste Thomas and Dr. Giuseppe Claudio Guarnera, at the Norwegian Colour and Visual Computing Laboratory in discussions and suggestions regarding the structure of this paper.

This work was supported by the MUVApp project N-250293, funded by the Research Council of Norway.

REFERENCES

1. C. Eugène, "Measurement of "total visual appearance": a cie challenge of soft metrology," in "12th IMEKO TC1 and TC7 Joint Symposium on Man, Science and Measurement," (Annecy, France, 2008), pp. 61 – 65.
2. G. Pfaff, *Special effect pigments: technical basics and applications* (Vincentz Network GmbH & Co KG, 2008).
3. P. Pjanic and R. D. Hersch, "Specular color imaging on a metallic substrate," in "Color and Imaging Conference," (Society for Imaging Science and Technology, 2013), pp. 61–68.

[1] Lambda 1050 uv/vis/nir spectrophotometer, http://www.perkinelmer.com/product/lambda-1050-uv-vis-nir-spectrophotometer-l1050?searchTerm=L1050&pushBackUrl=?searchName=L1050. Accessed:2017-03-09.

[2] Gcms-3 goniospectrophotometer system, http://www.aviangroupusa.com/pdf/GCMS3_Des.pdf. Accessed: 2017-03-09.

4. C. McCamy, "Observation and measurement of the appearance of metallic materials. part i. macro appearance," Color Research & Application **21**, 292–304 (1996).
5. A. Takagi, S. Sato, and G. Baba, "Prediction of spectral reflectance factor distribution of color-shift paint finishes," Color Research & Application **32**, 378–387 (2007).
6. E. Kirchner and W. Cramer, "Making sense of measurement geometries for multi-angle spectrophotometers," Color Research & Application **37**, 186–198 (2012).
7. A. Ferrero, A. Rabal, J. Campos, F. Martínez-Verdú, E. Chorro, E. Perales, A. Pons, and M. L. Hernanz, "Spectral brdf-based determination of proper measurement geometries to characterize color shift of special effect coatings," J. Opt. Soc. Am. A **30**, 206–214 (2013).
8. CIE15.2, "Colorimetry," CIE standard (2004).
9. ASTM-E2194, "Standard practise for multiangle color measurement of metal flake pigmented materials," ASTM Standard (2012).
10. ASTM-E2539, "Standard practise for multiangle color measurement of interference pigments," ASTM Standard (2012).
11. C. McCamy, "Observation and measurement of the appearance of metallic materials. part ii. micro appearance," Color Research & Application **23**, 362–373 (1998).
12. ASTM-E2175, "Standard practice for specifying the geometry of multiangle spectrophotometers," ASTM Standard (2013).
13. K. Kehren, "Optical properties and visual appearance of printed special effect colors," Ph.D. thesis, Technischen Universität Darmstadt, Darmstadt, Germany (2013).
14. J. Palmer and B. G. Grant, *The Art of Radiometry*, ISBN 978-0-8194-7245-8 (SPIE Press Bellingham, Washington USA, 2010).
15. F. E. Nicodemus, J. Richmond, J. J. Hsia, I. W. Ginsberg, and T. Limperis, "Geometrical considerations and nomenclature for reflectance," National Bureau of Standards (1977).
16. CIE175, "A framework for the measurement of visual appearance," Tech. rep., International Commission on illumination (2006).
17. S. Tominaga and N. Tanaka, "Estimating reflection parameters from a single color image," IEEE Computer Graphics and Applications **20**, 58–66 (2000).
18. D. Guarnera, G. Guarnera, A. Ghosh, C. Denk, and M. Glencross, "Brdf representation and acquisition," Computer Graphics Forum **35**, 625–650 (2016).
19. A. Sole, I. Farup, and S. Tominaga, "An image based multi-angle method for estimating reflection geometries of flexible objects," Color and Imaging Conference **2014**, 91–96 (2014-11-03T00:00:00).
20. A. S. Sole, I. Farup, and S. Tominaga, "An image-based multi-directional reflectance measurement setup for flexible objects," in "Measuring, Modeling and Reproducing Material Appearance 2015," , vol. SPIE 9398 M. V. O. Segovia, P. Urban, and F. H. Imai, eds. (Proceedings of SPIE-IS& T Electronic Imaging, 2015), vol. SPIE 9398, pp. 93980J – 93980J–11.
21. A. Sole, I. Farup, and P. Nussbaum, "Evaluating an image based multi-angle measurement setup using different reflection models," Electronic Imaging **2017**, 101–107 (2017).
22. A. Sole, I. Farup, and S. Tominaga, "Image based reflectance measurement based on camera spectral sensitivities," Electronic Imaging **2016**, 1–8 (2016).
23. N. Johansson and M. Andersson, "Angular variations of reflectance and fluorescence from paper-the influence of fluorescent whitening agents and fillers," in "Color and Imaging Conference," , vol. 2012 (Society for Imaging Science and Technology, 2012), vol. 2012, pp. 236–241.
24. N. Johansson, M. Neuman, M. Andersson, and P. Edström, "Influence of finite-sized detection solid angle on bidirectional reflectance distribution function measurements," Appl. Opt. **53**, 1212–1220 (2014).
25. H. Li, S.-C. Foo, K. E. Torrance, and S. H. Westin, "Automated three-axis gonioreflectometer for computer graphics applications," Optical Engineering **45**, 043605–043605 (2006).
26. J. C. for Guides in Metrology, "Evaluation of measurement data - guide to the expression of uncertainty in measurement," First edition 100, JCGM (2008).

Evaluating an image-based bidirectional reflectance distribution function measurement setup - errata

ADITYA SOLE,[1,*] IVAR FARUP,[1] PETER NUSSBAUM 1 AND SHOJI TOMINAGA [1]

[1] *The Norwegian Colour and Visual Computing Laboratory, Department of Computer Science, Faculty of Information technology and Electrical engineering, Norwegian University of Science and Technology*
[*] *aditya.sole@ntnu.no*

Abstract: Two typographical errors on page 1919 and 1923 in the journal paper " *Aditya Sole, Ivar Farup, Peter Nussbaum, and Shoji Tominaga, "Evaluating an image-based bidirectional reflectance distribution function measurement setup," Appl. Opt. 57, 1918-1928 (2018)*" are identified and have been corrected in this paper.

This erratum lists errors and their correction for the journal article [1] titled "*Evaluating an image-based bidirectional reflectance distribution function measurement setup*". Table 1 below lists the location of the error, the error, and the corresponding correction.

Location in [1]	**Error**	**Correction**
Page 1919 - Eq. (1)	$f_r(\theta_i, \phi i, \theta_r, \phi r, \lambda) = \frac{dL_r(\theta_i,\phi i,\theta_r,\phi r,\lambda)}{dE_i(\theta_i,\phi r,\lambda)}$	$f_r(\theta_i, \phi i, \theta_r, \phi r, \lambda) = \frac{dL_r(\theta_i,\phi i,\theta_r,\phi r,\lambda)}{dE_i(\theta_i,\phi i,\lambda)}$
Page 1923 - last line in the paragraph after Eq. (8).	ω_s remained constant over the pixel position (corresponding to the point P on the sample surface) and therefore was taken into account while calculating $I_i(\lambda)$.	ω_s remained constant over the pixel position (corresponding to the point P on the sample surface) and therefore was not taken into account while calculating $I_i(\lambda)$.

Table 1. Error and corresponding correction in article [1]

References

1. A. Sole, I. Farup, P. Nussbaum, and S. Tominaga, "Evaluating an image-based bidirectional reflectance distribution function measurement setup," Appl. Opt. **57**, 1918–1928 (2018).

Paper IV

A. Sole, I. Farup and T. Shoji, 'An image-based multi-directional reflectance measurement setup for flexible objects', in *Measuring, Modelling, and Reproducing Material Appearance 2015*, SPIE/IS&T Electronic Imaging 2015, 2015

An image-based multi-directional reflectance measurement setup for flexible objects

Aditya S. Sole, Ivar Farup, Shoji Tominaga

Aditya S. Sole, Ivar Farup, Shoji Tominaga, "An image-based multi-directional reflectance measurement setup for flexible objects," Proc. SPIE 9398, Measuring, Modeling, and Reproducing Material Appearance 2015, 93980J (13 March 2015); doi: 10.1117/12.2076592

SPIE.

Event: SPIE/IS&T Electronic Imaging, 2015, San Francisco, California, United States

Updated version 6 August 2019

An Image-Based Multi-Directional Reflectance Measurement Setup for Flexible Objects

Aditya S. Sole[a], Ivar Farup[a] and Shoji Tominaga[b]

[a]The Norwegian Colour and Visual Computing Laboratory, Gjøvik University College, Gjøvik, Norway;

[b]Graduate School of Advanced Integration Science, Chiba University, Chiba, Japan

ABSTRACT

This paper presents an image-based method to measure reflectance of a homogeneous flexible object material (usually used in packaging). A point light source and a commercially available RGB camera is used to illuminate and measure the radiance reflected from the object surface in multiple reflection directions. By curving the flexible object onto a cylinder of known radius we are able to record radiance at multiple reflection angles in a faster way. In order to estimate the reflectance and to characterise the material, a spectralon reference tile is used. The spectralon tile is assumed to be homogenous and has near lambertain surface properties. Using Lambert's cosine law, irradiance at a given point on the object surface is calculated. This information is then used to calculate a BRDF using Phong reflection model to describe the sample surface reflection properties. The measurement setup is described and discussed in this paper along with its use to estimate a BRDF for a given material/substrate. Results obtained indicate that the proposed image-based technique works well to measure light reflected at different planar angles and record information to estimate the BRDF of the sample materials that can be modelled using Phong reflection model. The object material properties, sample curvature and camera resolution decides the number of incident and reflection angles at which the bi-directional reflectance, or the material BRDF, can be estimated using this method.

Keywords: BRDF, Phong model, multi-angle reflection measurement, goniometric measurements

1. INTRODUCTION

Appearance of an object material is measured with the goal of objectively describing and quantifying human visual impressions with measurement values. Measurements help us communicate the appearance of the material in numerical terms. Material appearance can be described using surface reflectance properties. A Bidirectional Reflection Distribution Function (BRDF) of material will describe the surface reflectance properties of that material. BRDF completely describes the reflectance of an opaque surface at a given point.[1] The most appropriate way to measure the surface reflectance is by performing physical measurements of the reflected light.[1]

Physical reflectance measurements are performed (for example, in the packaging and car paint industry) to characterise and control reproduction of materials like printed packages and paints.[2,3] Different surface properties of these materials help produce desirable appearance of the material that varies with the direction of illumination and viewing. Many car paints used in car industry or gonio-chromatic materials used in print and packaging industry[2,4] produce a very desirable appearance by showing a shift or change in perceived colour depending upon illumination and viewing geometry. This change is achieved due to varying reflection at different viewing angles. Studies have shown that flexible materials like paper substrates (typically used in print and packaging industry) reflects light in an anisotropic manner.[5,6] The reflected light quantity is therefore dependent on incident light and viewing directions.

These substrates should therefore be measured with instrument measuring at more than one illumination and reflection angle combination[2,7] unlike the single geometry instruments (for example 0 °:45 °) traditionally used in

Further author information: (Send correspondence to Aditya S. Sole)
Aditya S. Sole: E-mail: adityas@hig.no, adityasole@gmail.com, Telephone: +47 611 35168
Ivar Farup: E-mail: ivar.farup@hig.no, Telephone: +47 611 35227
Shoji Tominaga: E-mail: shoji@faculty.chiba-u.jp, Telephone: +81 (0)90 2197 0543

Measuring, Modeling, and Reproducing Material Appearance 2015, edited by Maria V. Ortiz Segovia, Philipp Urban, Francisco H. Imai, Proc. of SPIE-IS&T Vol. 9398, 93980J · © 2015 SPIE-IS&T · CCC code: 0277-786X/15/$18 · doi: 10.1117/12.2076592

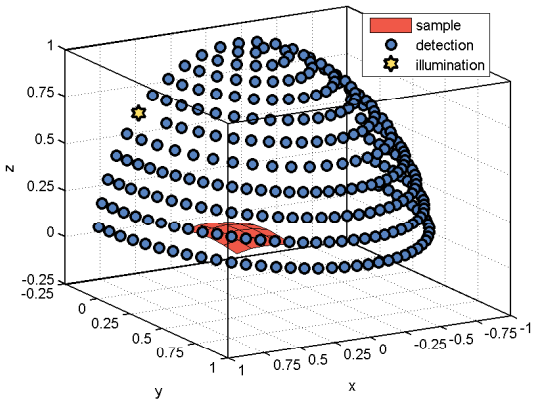

Figure 1: Gonio-metric measurements (Image taken from[3] and is licensed under CC BY-NC-ND).

the graphic arts and textile industry. Several commercial instruments available in the market (for example, X-rite MA98, BYK-Mac) can be used to perform multi-angle planar measurements. These instruments, however, are expensive and measure at a fixed illumination and reflection angles.[8] Gonio-spectro-photometers (mainly used in metrology institutes and research laboratories) can also be used to perform multi-angle plannar measurements. These instruments are more accurate and also measure gonio-metrically (refer figure 1). However, gonio-spectro-photometers are expensive and slow. There is, therefore a clear need to cover the bridge between the accurate (but slow) metrological instruments (like gonio-spectro-photometers) and user centric measurement methods/setups which should be fast and inexpensive.

In this paper we present an image based measurement setup, similar to ones proposed and used in measurement of velvets,[9] gloss[10] and human skin measurement,[1] to measure such materials at a faster speed. The measurement setup uses a point light source and a commercially available digital camera sensor (for example Nikon D200 DSLR camera) along with the sample to be measured. In the existing measurement setups (e.g. gonio-spectrometers, multi-angle spectrophotometers), the sample is usually flat on a surface and the light capturing sensor and/or light source rotate/move in the planar angles and azimuthal directions to illuminate and record the reflected light from the sample surface in different directions.[3] These setups therefore require considerable amount of time to record the reflectance at multiple angles. In order to avoid these moving parts (which are main cause of increase in measurement time) and thus reduce the measurement time, in the proposed setup, we keep the light source and the measurement sensor at fixed position from the sample (for example light source at 45° and sensor at 0°) and curve the measurement sample onto a cylinder[1,9–11] as shown in figure 2.

2. MEASUREMENT SETUP

Figure 2[12] shows the measurement setup we use for capturing the light reflected from a material substrate using an image based device. We, therefore, replace the flat surface measurement (using gonio-spectrometer) with a curved surface observation by a camera in our setup. The semi-circle (S) will be the curved substrate (for example packaging sample print) to be measured. The substrate is curved onto a cylinder of known radius (R). Point (C) is the sensor position (digital camera sensor) approximately at the center of the curved sample at a fixed distance d_C. L is a point light source illuminating the sample at a fixed angle $0^\circ < \theta_L < 90^\circ$ at a known distance d_L from the center of the curved sample.

Assuming that the curved sample is homogeneous, light incident and reflected at any given point on the sample will provide information with respect to the light source position (L), camera (C) and the surface normal vector ($\mathbf{n}$) direction. Figure 2 also shows the setup in a vector plane were θ_i and θ_r are incident and reflection

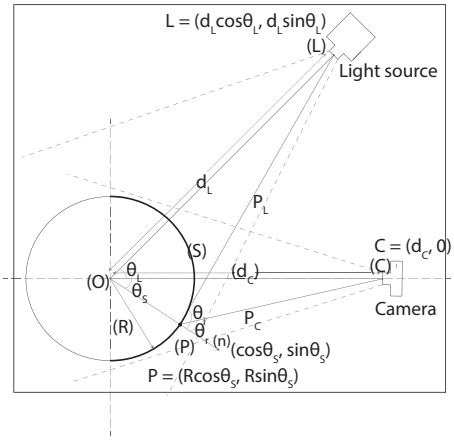

Figure 2: Measurement setup.

Table 1: θ_S calculation error.

Ruler points ($angles^\circ$)	-40	-30	-20	-10	0	10	20	30	40
Calculated angles ($angles^\circ$)	-41.90	-31.99	-22.05	-12.07	-2.12	7.7	17.7	27.68	37.7

angles with respect to the normal n at a given point P on the curved sample surface. Incident θ_i and reflection θ_r angles can be calculated as,[12]

$$\cos\theta_i = \frac{\mathbf{P}_L \cdot \mathbf{n}}{\mid P_L \mid} = \frac{d_L \cos(\theta_L - \theta_S) - R}{\sqrt{d_L^2 + R^2 - 2d_L R\cos(\theta_L - \theta_S)}},$$
$$\cos\theta_r = \frac{\mathbf{P}_C \cdot \mathbf{n}}{\mid P_C \mid} = \frac{d_C \cos\theta_S - R}{\sqrt{d_C^2 + R^2 - 2d_C R\cos\theta_S}}. \tag{1}$$

From Equation (1) it can be observed that when choosing a point on the curved sample surface to record the incident and reflected light, the θ_S angle changes with change in the location on the curved surface. θ_S can therefore be calculated using,[12]

$$\cos\theta_S = \frac{2d_C R d_A^2 \pm \sqrt{\left(-2d_C R d_A^2\right)^2 - 4\left(R^2 d_A^2 + F_L^2 R^2\right)\left(d_C^2 d_A^2 - F_L^2 R^2\right)}}{2R^2\left(d_A^2 + F_L^2\right)}. \tag{2}$$

In order to verify the θ_S calculation, an angular ruler was printed on a white paper substrate and measured using the setup. Figure 3 shows the captured image. The angular ruler can be observed at the bottom of the curved scene. The ruler points on the printed angular ruler indicate the θ_S angles, the corresponding pixel positions on the camera sensor, should measure/calculate using the Equation (1).[12] In order to minimize distortion due to lens, the object is positioned at the center of the image plane with sufficient distance from all the 4 corners. Unlike Marschner's[1] method, we perform manual physical measurements to determine the incident light position and camera. The pixel points corresponding to the angular ruler are located using second derivative[12] and the corresponding θ_S are calculated using Equation (2). Table 1 shows the calculated θ_S and the angular ruler points. We can observe an average error of 2.13° when calculating the reflection angles using Equation (2).[12] Figure 4 shows the error against the ruler points. The error can be corrected either by physically rotating the sample or subtracting the average error obtained from the calculated θ_S. For further calculation using θ_S the

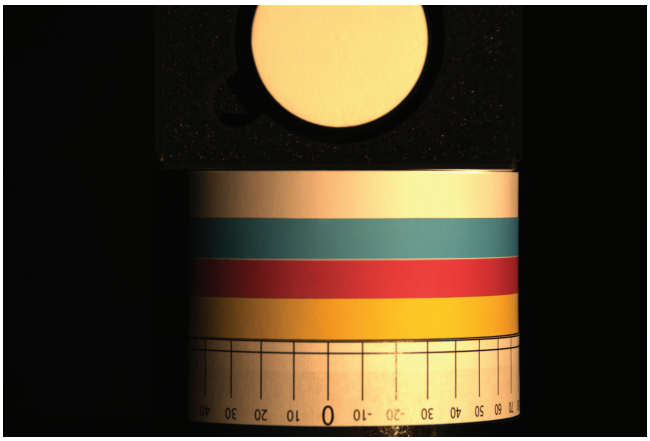

Figure 3: Captured image.

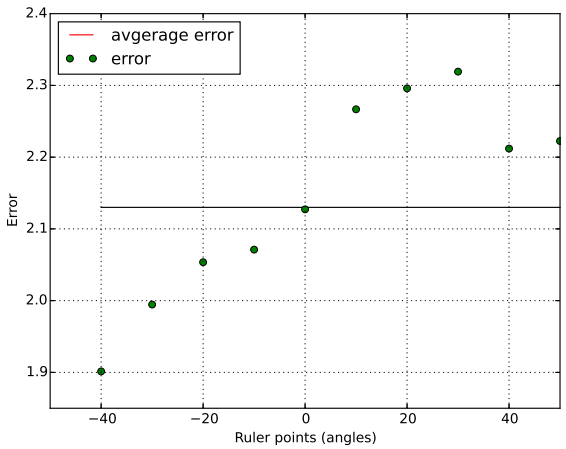

Figure 4: θ_S calculation error.

average error was subtracted from the calculated θ_S for the corresponding pixel points in the captured image. This corrected θ_S value was used for calculating θ_r and θ_r angles using Equation (1).

3. SAMPLE MEASUREMENT

A diffuse packaging print sheet (Matt coated white plotter sheet) was printed with solid colour patches to measure with the setup. Cyan and magenta colour patches were measured along with the paper white. These three materials are referred as material C (Cyan), M (Magenta) and W (Paper white) in the paper from here on. The sheet was wrapped around a cylinder of known radius (R=56mm). The image was captured using a Nikon D200 digital camera from a fixed distance (Cl=630mm). The curved sample on the cylinder was illuminated using a point light source at a distance (dL= approx. 1922mm). Figure (3) shows the captured image. The scene/curved sample was measured at three incident light directions (θ_L=29 °, 39 ° and 47 °). Spectralon tile was used as a reference to estimate the light incident on the curved sample and to normalise the image data.

The number of reflection angles at which the reflection information is to be recorded depends on the sample curvature.[12] As the curved sample is illuminated using a point light source at an incident light angle of θ_L=29 °, 39 °, 47 ° the illuminated areas on the curved sample is different for different θ_L. Therefore a part (horizontal) of the curved sample which is uniformly illuminated at all three incident (θ_L) angles is considered for the measurements.

Reference white measurement were recorded using the spectralon tile approximtely at θ_r=0 °. For each respective measurement, average of 100 pixel lines (along vertical axis) was used as the respective measurement.

Amount of light incident on the curved sample was calculated using the spectralon tile measurements. Assuming spectralon tile as lambertian we measure the light intensity at θ_r=0 ° on the spectralon tile (θ_i=θ_L). Using lambert's cosine law we estimate the light incident on the curved sample,

$$\begin{aligned} I_r &= I_i \cos\theta_i \\ I_i &= \frac{I_r}{\cos\theta_i} \end{aligned} \tag{3}$$

Where, I_i is the light incident on the sample, I_r is the amount of light reflected from the reference white tile (spectralon tile) and θ_i is the angle between point on the reference tile and incident light direction (θ_L).

4. BRDF CALCULATION USING PHONG REFLECTION MODEL

Bi-directional reflection distribution function (BRDF) describes the surface reflectance properties of a given opaque material.[13] The BRDF is defined[13] by,

$$f_r(\theta_i, \phi_i, \theta_r, \phi_r) = \frac{dL_r(\theta_i, \phi_i, \theta_r, \phi_r, E_i)}{dE_i(\theta_i, \phi_i)} \tag{4}$$

i and r denote incidence and reflection respectively. θ and ϕ together indicate the direction, E_i is incident irradiance, L_r is reflectance radiance and d is the differential quantity.

Modelling the reflection properties of material surfaces is important for material appearance measurement and simulation. Reflection models are widely used in computer graphics for generating realistic images.[14–16] In print and packaging applications, a reflectance model can be used for simulating the colour reproduction process.

The packaging print sheet printed with Magenta and Cyan solid inks showed fairly diffuse reflection properties with small amount of specular reflection on visual inspection. Phong reflection model was used to calculate the BRDF of these three material surfaces (materials C, M and W). Phong reflection model is an empirical model with two surface reflection components, diffuse reflection of rough surfaces and specular reflection of shiny surfaces.[14] Figure 5 shows the reflection geometry used for the Phong model, where **N** is the surface normal, **L** is the incident light vector, and **V** is the viewing vector. **R** and **Rv** are, respectively, **L** and **V** mirrored about **N**. A three-dimensional light reflection of the Phong model can be described[17] as

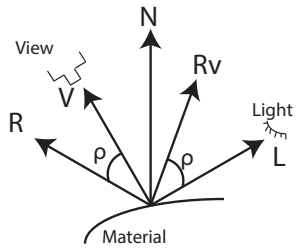

Figure 5: Vector diagram for Phong reflection model calculation.

$$Y(\theta,\lambda) = E_{amb}(\lambda) + (\cos\phi)\, S_d(\lambda)\, E(\lambda) + (\cos^{\alpha}\rho)\, S_s E(\lambda) \tag{5}$$

$Y(\theta,\lambda)$ is the radiance of light reflected from a surface and is a function of wavelenght (λ) and the geometric parameter θ, including the illumination direction angle, the viewing angle, and the phase angle. E_{amb} is the ambient light, $S_d(\lambda)$ is the surface-spectral reflectance of an object surface and $E(\lambda)$ is the spectral power distribution of the incident light. ϕ is the angle of incidence, ρ is the angle between the viewing vector $\mathbf{V}$ and the mirrored vector $\mathbf{R}$ of incident light vector (refer Figure 5), α is used as the measure of surface roughness and S_s is a constant value. The Phong model can be used with the measurement setup by inserting the model parameters with respect to the measurement setup. Referring Figure 2

$$\begin{aligned} \cos\phi &= \cos\theta_i \\ \cos^{\alpha}\rho &= \cos^{\alpha}(\theta_r - \theta_i) \end{aligned} \tag{6}$$

As the measurements were recorded using a colour camera. The camera output can be described as

$$\begin{bmatrix} R \\ G \\ B \end{bmatrix} = \int_{400}^{700} Y(\theta,\lambda) \begin{bmatrix} r(\lambda) \\ g(\lambda) \\ b(\lambda) \end{bmatrix} d\lambda \tag{7}$$

where $r(\lambda)$, $g(\lambda)$ and $b(\lambda)$ are the spectral sensitivity functions of the camera. Inserting Equation (6) in Equation (5), the camera colour output I at the spatial location p can be described as

$$I_p = \begin{bmatrix} R \\ G \\ B \end{bmatrix} = k_a \mathbf{I_a} + k_d \mathbf{I_d} (\cos\theta_i) + k_s \mathbf{I_s} (\cos^{\alpha}(\theta_r - \theta_i)). \tag{8}$$

$\mathbf{I_a}$ is the ambient light vectors, $\mathbf{I_d}$ is the diffuse component (object colour) vectors, $\mathbf{I_s}$ is the specular component (incident light) vectors. k_a, k_d, k_s, are the ambient, diffuse and specular reflection constants.

4.1 Colour Phong reflection model

In this paper we implement the Phong model using two methods. In the *first method* - Colour Phong reflection model, we use the object colour vector (body reflection) as the diffuse component $\mathbf{I_d}$ and the incident light as the specular component as defined in Equation (8). Diffuse component ($\mathbf{I_d}$) value for each material was selected from the non-specular region of the captured image. From the calculated incident and reflection angles and the known incident light direction (θ_L) an approximate pixel area (average of 2500 pixels) was selected from the non-specular area of the image. Specular component is the light incident ($\mathbf{I_i}$) on the material. Table 2 below shows the I_d value for each material (W,C and M). The ambient light term is treated as a constant $K_a\mathbf{I_a}$=k_{amb}. Equation (8) therefore can be written as

$$I_p = k_{amb} + k_d \begin{bmatrix} R^0 \\ G^0 \\ B^0 \end{bmatrix} cos\theta_i + k_s \mathbf{I_i} (\cos^{\alpha}(\theta_r - \theta_i)). \tag{9}$$

Table 2: Material body reflection component (I_d).

Material	Red (R^0)	Green (G^0)	Blue (B^0)
W	0.7612	0.5458	0.3500
C	0.3962	0.6601	0.6381
M	0.9473	0.2321	0.2204

Table 3: Phong model parameters fitted using Colour Phong reflection model (Section 4.1).

Material	ka	kd	ks	alpha	LRMSE
W	0.0566	0.5493	0.1691	0.8339	0.0193
C	0.0265	0.3307	0.0760	1.2109	0.0170
M	0.0034	0.4242	0.0785	0.8681	0.0174

$[R^0, G^0, B^0]^T$ is the normalised object body reflection (refer Table 2) of the respective material (W, C, M) and $\mathbf{I_i}$ is an identity vector $[1, 1, 1]^T$. We use Equation (9) as a color model for the Phong reflection model. Reflection constants (k_{amb}, k_d, k_s and α) were therefore fitted in Equation (9) using the data captured at three incident light directions (θ_L=29 °, 39 °, 47 °) and R, G and B sensors for the respective materials. The constants were further optimized using the Nelder-Mead downhill simplex algorithm[18] to find the minimum of a function with the given paramters. Root mean square (RMS) error between the measured data and the estimated data was used as the minimizing function. Table 3 shows the reflection constant fitted for the three materials (C, M and W) using Equation (9). Figures (6,7, and 8) shows the plots for the light intensity reflected from the three materials (C, M and W) and the light intensity estimated using Equation (9) for 2 incident light directions (θ_L=29 ,θ_L=47).

4.2 Monochrome Phong reflection model

As we have used a point light source and the materials measured using the setup being fairly diffuse, in the *second method* - Monochrome Phong reflection model, we use the incident light I_i in all the three components of the model. That is I_a=I_d=I_s=I_i. Also the ambient light term is treated as a constant $K_a I_i$=k_{amb}. Inserting this in Equation (8),

$$I_p = k_{amb} + I_i(k_d(\cos\theta_i) + k_s(\cos^\alpha(\theta_r - \theta_i))). \tag{10}$$

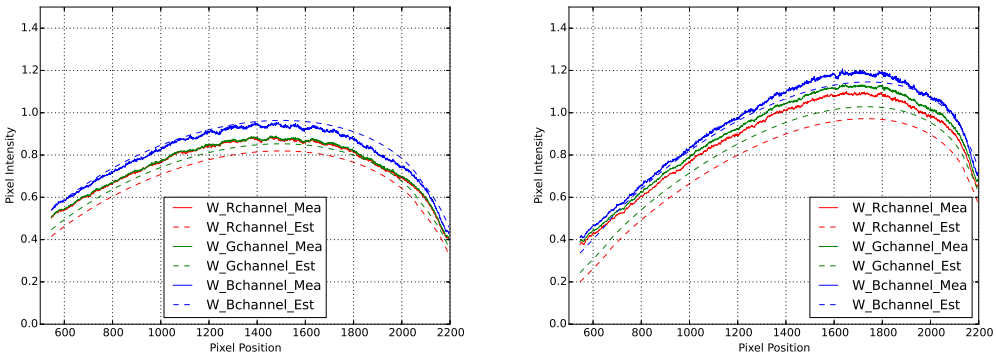

(a) θ_L=29 ° (b) θ_L=47 °

Figure 6: Reflected intensity I_p measured and estimated using Equation (9) for material W.

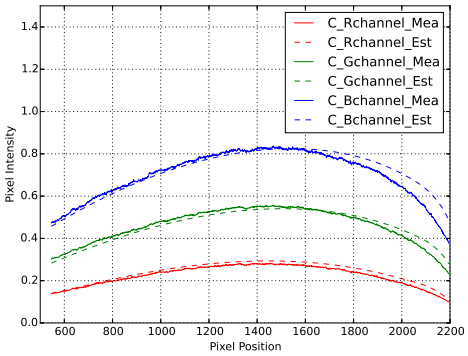

(a) θ_L=29 °

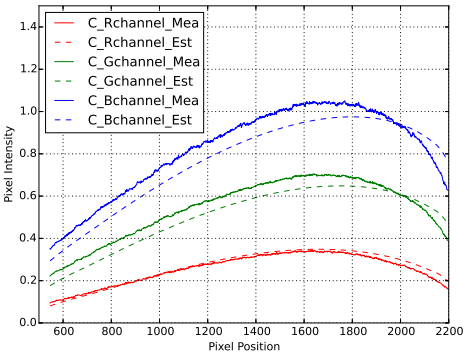

(b) θ_L=47 °

Figure 7: Reflected intensity I_p measured and estimated using Equation (9) for material C.

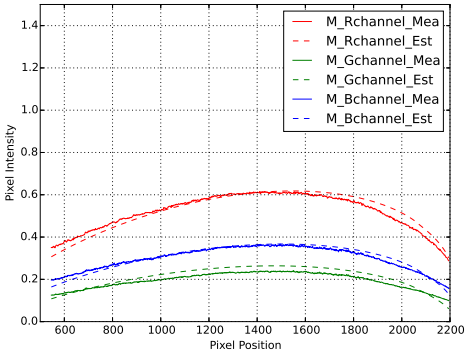

(a) θ_L=29 °

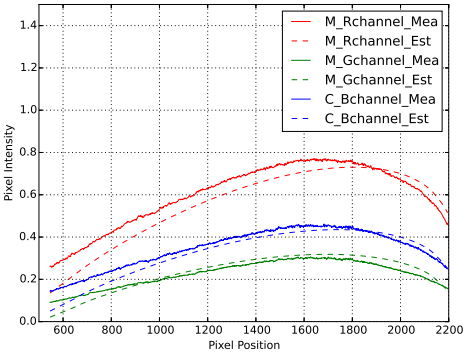

(b) θ_L=47 °

Figure 8: Reflected intensity I_p measured and estimated using Equation (9) for material M.

As the image is captured using an RGB sensor camera, in this method we model the above Equation (refer Equation 10) separately for R, G and B intensities, thus having different reflection constants k_{amb}, k_d, k_s and α for individual R, G and B sensor channels for the respective materials.

The reflection constants k_{amb}, k_d, k_s and α were fitted in Equation (10) using the data captured at three incident light directions (θ_L=29 °, 39 °, 47 °) for the materials W, C and M. Similar to the Colour model (refer Section 4.1), the constants were further optimized the Nelder-Mead downhill simplex algorithm.[18] Root mean square (RMS) error between the measured data and the estimated data (using Equation (10) was used as the minimizing function. Table 4 shows the reflection constants fitted for the three materials (C, M and W) for individual sensor channels (R,G,B) using the data captured with three different incident light directions (θ_L=29 °, 39 °, 47 °). Figures 9,10, and 11 show the plots for the light intensity reflected from the three materials (C, M and W) and the light intensity estimated using the above model for the three sensor channels (R, G, B) and for 2 incident light directions (θ_L=29 , θ_L=47). We believe that modelling the Phong parameters for individual sensors (R, G and B in this case) should help us simulate the material appearance with more control for highly specular and gonio-chromatic colours. Phong parameters of individual sensors should help simulate the gonio-chromatic appearance of homogenous material once the incident light intensity (I_i), direction (θ_L) and

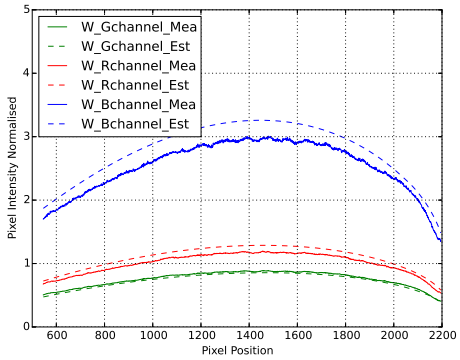

(a) θ_L=29 °

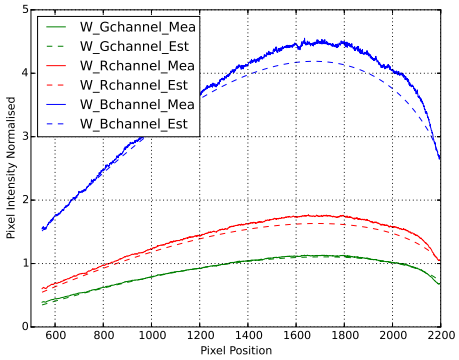

(b) θ_L=47 °

Figure 9: Reflected intensity I_p measured and estimated using Equation (10) for material W.

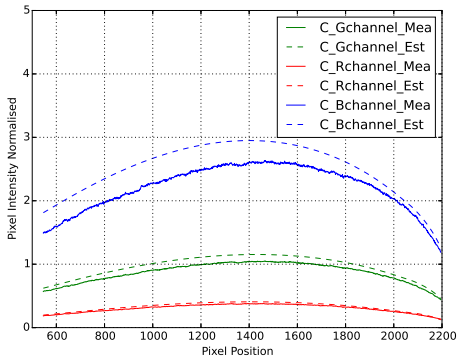

(a) θ_L=29 °

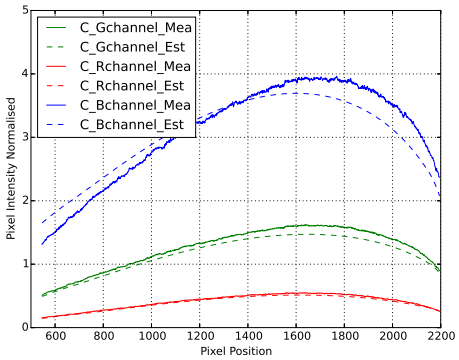

(b) θ_L=47 °

Figure 10: Reflected intensity I_p measured and estimated using Equation (10) for material C.

sample curvature is known with other parameters required to calculate incident (θ_i) and reflection (θ_r) angles as described in Equation (1).

5. CONCLUSION

In this paper we have presented a measurement setup which can be used to perform gonio-metric measurements of homogenous non-diffuse flexible object materials (for example packaging substrates) using an image based technique at a relatively faster speed. Phong reflection model was used to demonstrate BRDF measurement using the presented setup. Phong model was implemented using two methods (Colour Phong reflection model and Monochrome Phong reflection model).

In the Colour Phong reflection model, object colour was used as the diffuse component I_d of the light source and incident light I_i as the specular component I_s. Phong parameters (k_{amb}, k_d, k_s and α) were estimated using all the three camera sensors (R,G and B). Image data captured using three different incident light directions (θ_L) were used as training data for estimation. Root Mean Square (RMS) error was calculated between the measured and estimated reflected light intensity. The results (refer Table 3 and Figures 6,7, and 8) show that

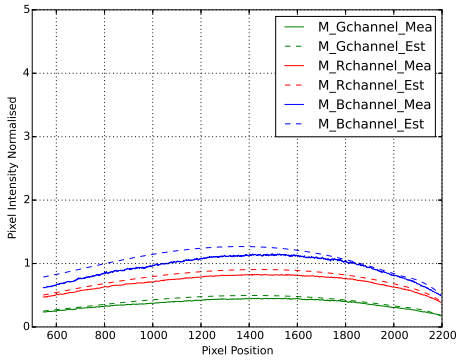

(a) θ_L=29 °

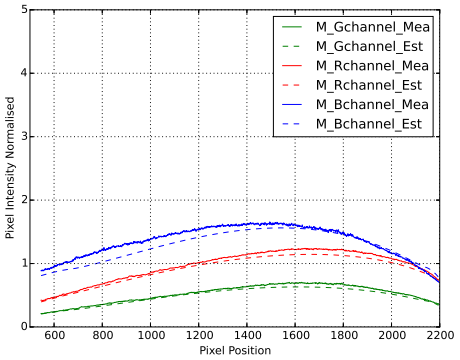

(b) θ_L=47 °

Figure 11: Reflected intensity I_p measured and estimated using Equation (10) for material M.

Table 4: Phong model parameters fitted using the Monochrome Phong reflection model (Section 4.2).

	Sensor channels	ka	kd	ks	alpha	LRMSE
Material W	**Green**	0.0982	0.4633	0.1719	0.9882	0.0073
	Red	0.2498	0.6093	0.2805	1.0204	0.0681
	Blue	0.3115	1.4458	0.7364	1.0624	0.0907
Material C	**Green**	0.1704	0.474	0.3072	1.124	0.0498
	Red	0.0746	0.1494	0.1345	1.2157	0.0185
	Blue	0.4371	0.6363	0.8319	1.0734	0.0979
Material M	**Green**	0.0727	0.1811	0.1543	1.2918	0.0203
	Red	0.1853	0.4019	0.2114	1.1212	0.0489
	Blue	0.235	0.0416	0.4305	1.2728	0.0377

the measurement setup and the Phong reflection model works well to estimate the BRDF of the sample material used. To compare and evaluate the performance of the measurement setup it would be ideal to measure these sample materials with a gonio-spectrophotometer and evaluate the performance of setup presented above against these measurements. Due to limited access to such an instrument this evaluation could not be performed in this paper.

In the Monochrome Phong reflection model, we have used the incident light I_i as both the diffuse light component and the specular light component in the Phong reflection model. Also, the material image being captured using three sensors (R, G and B), the Phong parameters were estimated separately for R, G and B intensities for the respective sample material. Modelling the Phong parameters for individual sensors and using the incident light as the diffuse and specular light component, in the model, the material appearance could be simulated using the incoming light information. This approach should specifically help simulate/visualise material appearance for highly non-diffuse and gonio-chromatic homogenous materials. Similar to first method, RMS error was calculated between the measured and estimated reflected light intensity. The results (refer Table 4 and Figures 9,10, and 11) show that thought the RMS values are high (especially for blue sensor channel), which may be due to the fluorescence in the sample material used),the measurement setup and the Phong reflection model can be used to estimate the sensor dependent BRDF of the sample material used in this paper.

ACKNOWLEDGMENTS

We would like to thank and acknowledge the support of Dr. Peter Nussbaum from the Norwegian Colour and Visual Computing Laboratory, Gjøvik University College, Norway and Mr. Johansson Niklas from Digital Print Center, Mid Sweden University, Sweden for there participation in discussions. We would also like to thank Mr. Ping Zhao from the Norwegian Colour and Visual Computing Laboratory, Gjøvik University College, Norway for discussions on camera characterisation.

REFERENCES

1. S. R. Marschner, S. H. Westin, E. P. F. Lafortune, K. E. Torrance, and D. P. Greenberg, "Image-based brdf measurement including human skin," in *10th Eurographics Workshop on Rendering*, pp. 139 – 152, 1999.
2. C. S. McCamy, "Observation and measurement of the appearance of metallic materials. part 1. macro appearance." Journal, 1996.
3. K. Kehren, *Optical Properties and Visual Appearance of Printed Special Effect Colors*. PhD thesis, Technischen Universität Darmstadt, Darmstadt, Germany, April 2013.
4. *Appearance Measurements of Goniochromatic Colours*, (Edinburgh, UK), 3rd International Conference on Appearance, April 2012.
5. M. Neuman, P. Edström, M. Andersson, L. G. Coppel, and O. Norberg, "Angular variations of color in turbid media - the influence of bulk scattering on goniochromism in paper," pp. 407 – 413, 2010.
6. M. Neuman and P. Edström, "Anisotropic reflectance from turbid media. ii measurements," *Journal of Optical Society, America* **27**, pp. 1040–1045, 2010.
7. C. S. McCamy, "Observation and measurement of the appearance of metallic materials. part ii. micro appearance," 1998.
8. G. Baba, "Gonio-spectrophotometry of metal-flake and pearl-mica pigmented paint surfaces," in *Proceedings of the fourth Oxford conference on spectrophotometry*, pp. 79–86, SPIE, 2003.
9. J. J. K. Rong Lu and A. M. L. Kappers, "Optical properties (bidirectional reflection distribution functions) of velvet," *Applied Optics* **37**, pp. 5974 – 5984, September 1998.
10. A. Jonathan, A. P., and H. Heo, "A micro-goniophotometer and the measurement of print gloss," *Journal of Imaging and Science Technology* **48**(5), pp. 458 – 463, 2004.
11. S. Tominaga and N. Tanaka, "Estimating reflection parameters from a single color image," *IEEE Computer Graphics and Applications* **20**(5), pp. 58 – 66, 2000.
12. A. Sole, I. Farup, and S. Tominaga, "An image based multi-angle method for estimating reflection geometries of flexible objects," *Color and Imaging Conference* **2014**, pp. 91–96, Novemeber 2014-11-03T00:00:00.
13. F. E. Nicodemus, J. Richmond, J. J. Hsia, I. W. Ginsberg, and T. Limperis, "Geometrical considerations and nomenclature for reflectance." National Bureau of Standards, 1977.
14. B. T. Phong, "Illumination for computer generated pictures," *Commun. ACM* **18**, pp. 311–317, June 1975.
15. J. F. Blinn, "Models of light reflection for computer synthesized pictures," in *Proceedings of the 4th Annual Conference on Computer Graphics and Interactive Techniques*, *SIGGRAPH '77*, pp. 192–198, ACM, (New York, NY, USA), 1977.
16. R. L. Cook and K. E. Torrance, "A reflectance model for computer graphics," *ACM Trans. Graph.* **1**, pp. 7–24, Jan. 1982.
17. S. Tominaga, "Dichromatic reflection models for rendering object surfaces," *Journal of Imaging Science and Technology* **40**(6), pp. 549 – 555, 1996.
18. N. J. A and R. Mead, "A simplex method for function minimization," *The Computer Journal* **7**, pp. 308 – 313, January 1965.

Paper V

A. Sole, I. Farup and P. Nussbaum, 'Evaluating an image based multi-angle measurement setup using different reflection models', *Electronic Imaging*, vol. 2017, no. 8, pp. 101–107, 2017, ISSN: 2470-1173

https://doi.org/10.2352/ISSN.2470-1173.2017.8.MAAP-280

Evaluating an image based multi-angle measurement setup using different reflection models

Aditya Sole, Ivar Farup, and Peter Nussbaum;
The Norwegian University of Science and Technology, Gjøvik, Norway,

Abstract

Image based measurement setups are widely used for multi-directional reflectance measurements of materials. Different reflection models are used to estimate the material reflectance.

In this paper we use two commonly known simple reflection models to evaluate an image based measurement setup proposed in our previous studies. Sample material is measured at multiple incident and viewing directions using the setup. The captured data is divided into training and test set to evaluate the setup. Two reflection models are trained using the training dataset. To evaluate the measurement setup, one of the sample materials is measured at few incident and viewing directions using a light source and a Tele-Spectro-Radiometer (TSR). This measured data is then compared with the reflectance estimated by the two reflection models.

Results shows that image based multi-directional reflectance measurements can be performed using measurement setup proposed in our previous work. The data captured using the setup can be used to fit different reflections models for the sample materials used in this setup.

Introduction

Image based instruments that are relatively cheap and fast, are being increasingly used in multi-angle reflectance measurements of the material [1, 2, 3]. The multi-angle data captured can be further processed (for example to estimate the material BRDF). Where the need is to acquire fast and cheap measurements, image based instruments can be a good alternative compared to the expensive, time consuming, but precise instruments (like Goniospectrometers). These measurements can then be used to train reflection models to calculate the BRDF and simulate or reproduce the material appearance. A number of reflection models are proposed till now which mainly aim towards fulfilling the needs of the computer graphics field to simulate material appearance in a given scence/situation. One of the main aims of the computer graphics field is to accurately measure the appearance of materials and simulate/reproduce synthetically the real object using simple methods/techniques [4]. A Bidirectional Reflection Distribution Function (BRDF) is a distribution function that describes the surface reflectance properties of opaque and homogenous materials [5] as given in Equation (1).

$$f_{BRDF}(\theta_i, \phi_i; \theta_r, \phi_r, \lambda) = \frac{dL_r(\theta_i, \phi_i, \theta_r, \phi_r, E_i)}{dE_i(\theta_i, \phi_r)} \tag{1}$$

Here, i and r denote incidence and reflection respectively. θ and ϕ together indicate the direction, E_i is incident irradiance, L_r is radiance and d is the differential. Guarnera [4] presented an overview of the BRDF models used to represent surface/material reflection characteristics. As discussed in [4], BRDF models can be classified into Physically-based models and Phenomenological models. Physically-based models are based on physics and optics and are described using micro-facets of varying size and orientations. One of the very well known and widely used physical models is the Cook-Torrance [6] model. Phenomenological models are approximations of the reflectance data using measured data and fitting of the same using analytical models. Some of the commonly known phenomenological models are the Phong [7], Ward [8], Lafortune [9], etc.

In our previous studies [3] we presented a measurement setup which can perform multi-angle reflectance measurements of homogenous, flexible materials in a fast and relatively cheap way. In this setup, we mount the flexible sample onto a cylinder of known radius and measure using a RGB camera [10, 3]. The captured RGB data is converted into the colorimetric space CIEXYZ using the conversion matrix $\hat{M}$. Matrix $\hat{M}$ is derived using the camera spectral sensitivity (measured using a monochromator) and the CIE 2° colour matching functions by minimising the error using least square technique [11]. This data can be used further as training data to train different reflection models (like Cook-torrance or Ward model) to estimate the sample BRDF and simulate the material appearance.

The objectives of the work presented in this paper are:

- to estimate the surface reflectance properties of the sample materials used in the experimental setup using the image based multi-angle measurement setup proposed in previous studies [3],
- to train different reflection models using the colorimetric data captured with the image based multi-angle measurement setup and evaluate the setup against measurements obtained using a TSR,
- test the trained reflection models to predict the sample material reflectance at different illumination and viewing directions.

Background

In order to evaluate the measurement setup we used 2 reflections models; Cook-Torrance (hereby referred as CT in this paper) and Ward to fit the measurement data obtained in the measurement setup by using the RGB camera [3]. The trained model parameters were then used to estimate the BRDF measurement at different incident and viewing directions. CT model is a physical model that describes the intensity and spectral composition of the light reflected from the object/material. CT model as described in

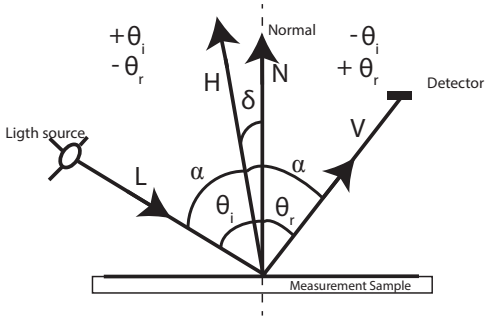

Figure 1. *Angles and vectors used in reflection equations.*

[6] is given in Equation (2).

$$I_r = I_{ia}R_a + \sum_l I_{il}(\mathbf{n}\cdot\mathbf{l})\omega_l(sR_s + dR_d) \tag{2}$$

Where, I_r is the total reflected intensity reaching the viewer, I_{ia} is the ambient light intensity, R_a is the ambient reflection component, I_{il} is the incident light intensity for incident light **l**, **n** is the normal vector as the given pixel point (P), **l** is the incident light vector, ω_l is the incident light solid angle, s and d are the specular and diffuse component co-efficients dependent on the material being simulated/reproduced, R_s and R_d are the specular and diffuse component of the model. The ambient R_a and diffuse R_d component of the model reflect light equally in all directions and therefore are independent of the location of the observation, whereas, the specular R_s component is dependent on the location of observation. For the specular component R_s, the angular spread is described assuming that the surface consist of microfacets, whose, normal is in the **h** direction and contributes in the specular component of reflection. Vector **h** is the half angle vector between the viewing vector **v** and incident light vector **l** such that $\mathbf{l}\cdot\mathbf{h} = \mathbf{v}\cdot\mathbf{h}$. The specular component is given as

$$R_s = \frac{FDG}{\pi(\mathbf{n}\cdot\mathbf{l})(\mathbf{n}\cdot\mathbf{v})} \tag{3}$$

where, F is the Fresnel term that describes how light is reflected from each microfacet. G is the geometrical attenuation factor accounting for the shadow and masking and D is the Beckmann distribution. **n** is the vector normal at the given pixel point (P), **v** is the viewing vector and **l** is the illumination vector. G and D are given as

$$G = \min\left\{1, \frac{2(\mathbf{n}\cdot\mathbf{h})(\mathbf{n}\cdot\mathbf{v})}{(\mathbf{v}\cdot\mathbf{h})}, \frac{2(\mathbf{n}\cdot\mathbf{h})(\mathbf{n}\cdot\mathbf{l})}{(\mathbf{v}\cdot\mathbf{h})}\right\}$$
$$D = \frac{1}{m^2\cos^4\alpha}e^{-[(\tan\delta)/m]^2} \tag{4}$$

where α is the angle between **n** and **h** (refer Figure 1), m is the root mean square slope of the facet in the material (or roughness co-efficient) and **h** is the half angle vector between **v** and **l**.

Ward model [8] is a phenomenological model with the aim to fit measured reflectance data with a simple empirical formula.This model represents both isotropic and anisotropic reflection and uses a gaussian distribution for the specular peaks. As the samples used in this work are isotropic samples we use the isotropic Ward model. The isotropic Ward model is given as

$$\rho_{bd_{iso}}(\theta_i,\phi_i;\theta_r,\phi_r) = \frac{\rho_d}{\pi} + \frac{\rho_s}{\sqrt{\cos\theta_i\cos\theta_r}}\frac{e^{\left[-\tan^2\delta/\alpha^2\right]}}{4\pi\alpha^2} \tag{5}$$

here $\rho_{bd_{iso}}$ is the bidirectional reflectance distribution for the given isotropic sample material, ρ_d is the diffuse reflectance, ρ_s is the specular reflectance, δ is the angle between vectors $\hat{n}$ and $\hat{h}$ as shown in Figure 1, α is the standard deviation (RMS) of the surface slope and $1/4\pi\alpha^2$ is the normalisation factor.

Method

Sample measurement

Wax based inks printed on a matt coated white plotting paper were used as test sample material to capture using the image based multi-angle reflectance measurements. We used the OCE ColorWave 600 to print 7 different colour samples on matt coated white plotting paper. These samples were measured using the measurement setup [3] at 10 different illumination directions (θ_L = 5°, 10°, 15°, 18°, 20°, 22°, 25°, 28°, 30°, and 35°). A tungsten point light source was used to illuminate the samples and Nikon D200 DSLR camera as measurement sensor. Figure 2 shows the captured image of the sample at θ_L = 15°. Spectralon tile was used as reference white in the scene. The incident (θ_i) and refection (θ_r) angles at given pixel points (P) were calculated for all the illumination directions (θ_L). Raw images of the samples were captured. No white balance or gamma corrections are performed on the captured RGB data. The captured R, G and B intensities are transformed into CIEXYZ colour space using the transformation matrix $\hat{M}$ derived using the camera spectral sensitivity (measured using a monochromator) and the CIE 2° colour matching functions by minimising the error using least square technique [11].

Training of the BRDF models

As the print samples are reproduced from wax inks, as can be seen in the captured image (refer Figure 2), the samples show some specularity but overall are diffuse. We train two BRDF models (CT and Ward) using the camera measurements of these samples. These samples are measured at 10 different incident light directions (θ_L). Figure 3 and 4 show plots of the CIE Y for the corresponding viewing angles (θ_r) for the samples Cyan and Pantone 10309C measured at $\theta_L = 25°$ and 28°. To train the 2 models we use measurement data (hereby referred as training dataset) of 5 of these 10 incident light directions (particularly 5°, 15°, 20°, 25° and 30°). Figure 1 shows the sign convention followed for the measurement angles in this paper. The same sign convention is followed in the image based multi-angle measurement setup and the TSR measurements performed.

Cook-Torrance model

Assuming that the samples are homogeneous, uniform and non-florescent, to train the CT model, we insert the measurement setup parameters in Equation (2). The camera colorimetric output

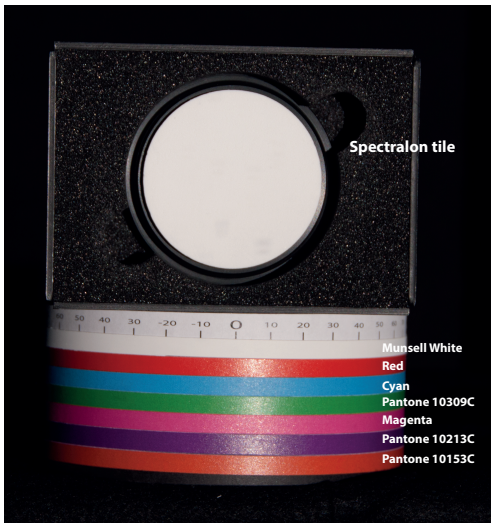

Figure 2. *Captured image of the samples.*

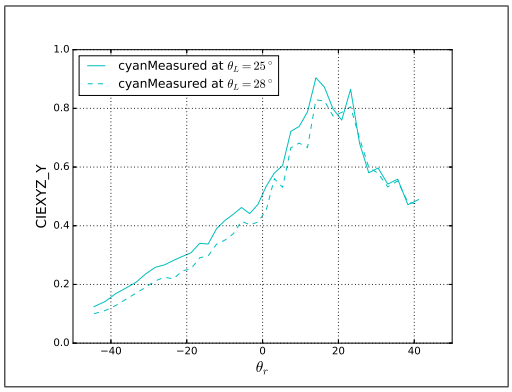

Figure 3. *CIEXYZ Y value, Cyan sample.*

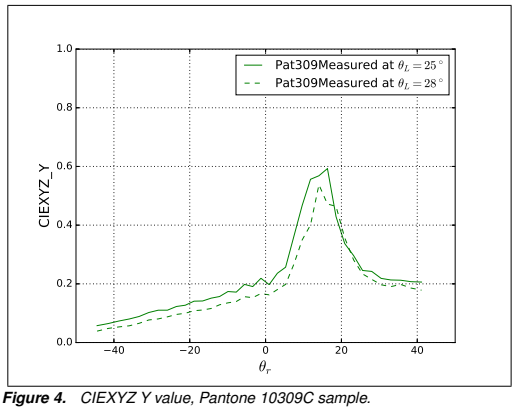

Figure 4. *CIEXYZ Y value, Pantone 10309C sample.*

$I_{(X,Y,Z)}$ at pixel points (P) will be,

$$I_P = \begin{bmatrix} I_{P_X} \\ I_{P_Y} \\ I_{P_Z} \end{bmatrix} = I_{ia}R_a + I_i(\mathbf{n}\cdot\mathbf{l})(sR_s + dR_d) \tag{6}$$

To simplify the optimisation of the CT model, we use $s+d=1$. Therefore,

$$I_P = \begin{bmatrix} I_{P_X} \\ I_{P_Y} \\ I_{P_Z} \end{bmatrix} = I_{ia}R_a + I_i\cos\theta_i \left(k_sR_s + (1-k_s)\begin{bmatrix} R_{d_X} \\ R_{d_Y} \\ R_{d_Z} \end{bmatrix} \right) \tag{7}$$

Where, R_s is as defined in Equation (3), F is assumed as 1, D and G are as defined in Equations (4), $I_{ia}R_a$ = ambient light (assumed as zero as the measurements are performed in dark conditions), I_i = incident light intensity, θ_i = angle between the incident light direction and normal to the sample surface, θ_r = angle between the viewing direction and normal to the sample surface, k_s =specular coefficients of the sample material, R_s=specular reflectance component, $R_{d_{X,Y,Z}}$=spectral diffuse reflectance component, $\delta = \mathbf{n}\cdot\mathbf{h} = \cos((\theta_i - \theta_r)/2)$ at the given pixel point (P) in the used measurement setup, $\mathbf{n}\cdot\mathbf{l} = \cos\theta_i$, $\mathbf{n}\cdot\mathbf{v} = \cos\theta_r$. As the area on the sample measured by the pixel being very small we absorb the solid angle ω_l term in the coefficients K_s and $R_{d_{X,Y,Z}}$.

Ward model

As the training dataset is the colorimetric data obtained from camera output in terms of RGB intensities, we train the Ward model using the intensity measurements rather than as reflectance. Also the measurements being planner, angle (ϕ) can be ignored. Inserting the measurement setup parameters in Equation (5)

$$I_P(\theta_i;\theta_r) = \begin{bmatrix} I_{d_X} \\ I_{d_Y} \\ I_{d_Z} \end{bmatrix} = I_i\cos\theta_i \left(\begin{bmatrix} R_{d_X} \\ R_{d_Y} \\ R_{d_Z} \end{bmatrix} \frac{1}{\pi} + \frac{k_s}{\sqrt{\cos\theta_i\cos\theta_r}} \frac{e^{\left[-\tan^2\delta/m^2\right]}}{4\pi m^2} \right) \tag{8}$$

where, I_i = incident light intensity, θ_i and θ_r as explained in the CT model, k_s =specular coefficients of the sample material, $R_{d_{X,Y,Z}}$=spectral diffuse reflectance component, $\delta = \cos((\theta_i - \theta_r)/2)$ at the given pixel point (P) in the used measurement setup.

Reflection coefficients k_s, $R_{d_{X,Y,Z}}$ and m are fitted and optimised using the training dataset. Nelder-Mead down-hill simplex algorithm [12] was used to optimise the coefficients using the ΔE_{00} colorimetric difference as the error function. In order to calculate the ΔE_{00} colorimetric difference, the CIEXYZ values were converted to CIELAB colour space using the same point light source that was used in the image based multi-angle measurement setup. The spectralon tile was measured using a Minolta CS1000 TSR for a given incident light directions. Assuming the spectralon tile as a perfect diffuser, these measurements were then used as the reference white in the CIELAB calculations. Table 1 provides the optimized co-efficient obtained for the 7 samples using both the models.

Physical measurements using a TSR

To validate the image based multi-angle measurement setup against physical measurements (e.g. performed using gonio- or

multiangle measurement setup using spectrometers), we measured one of the sample material (Cyan) using the Minolta CS1000 TSR at 4 different viewing directions (θ_r) for a given incident direction (θ_i). The cyan sample is measured at $\theta_i = 40^\circ$ and $\theta_r = -10^\circ, 0^\circ, 10^\circ$ and, 30°. Spectralon tile was measured along with the patch to normalise the radiance measurements and to calculate the spectral reflectance. The obtained spectral reflectances were converted to CIEXYZ colour space using the point light source (used in the image based multi-angle measurement setup) as the light source and transformed colour matching functions $\hat{C}$ obtained using the matrix $\hat{M}$ and the CIE 2° colour matching functions as derived in [11]. The obtained CIE Y value was then compared with the CIE Y value estimated using the trained CT and Ward model for the same incident and viewing directions. To estimate the CIEXYZ value using the BRDF models, we used the co-efficients $R_{d_X}, R_{d_Y}, R_{d_Z}, k_s$ and, m (refer Table 1) that are optimised using the camera measured training dataset. These co-efficients are implemented in Equations (7) and (8) for $\theta_i = 40^\circ$ and $\theta_r = -10^\circ, 0^\circ, 10^\circ$ and, 30°.

Table 1: Coefficients for the 7 samples optimised using the CT and Ward model

Material	R_{d_X}	R_{d_Y}	R_{d_Z}	k_s	m
CT model					
Munsell white	1.175	1.131	2.215	0.042	0.393
Red	0.303	0.229	0.112	0.029	0.119
Cyan	0.517	0.519	1.465	0.068	0.230
Pantone 10309C	0.181	0.256	0.304	0.029	0.133
Magenta	0.499	0.374	0.651	0.079	0.222
Pantone 10213C	0.428	0.407	0.508	0.0	0.759
Pantone 10153C	0.426	0.324	0.219	0.095	0.252
Ward model					
Munsell white	1.508	1.451	3.5	0.663	0.45
Red	0.537	0.351	0.251	0.061	0.122
Cyan	0.951	1.022	2.756	0.163	0.249
Pantone 10309C	0.377	0.514	0.579	0.061	0.134
Magenta	0.864	0.596	1.286	0.174	0.225
Pantone 10213C	0.265	0.188	0.607	0.085	0.143
Pantone 10153C	0.817	0.591	0.561	0.119	0.197

Results

We measured 7 sample materials at 10 different illumination directions (θ_L). We used the measurement data captured at 5 illumination directions as training data set to train the two models. In order to test the performance of the trained models we use the measured data from the remaining 5 illumination directions (particularly 10°, 18°, 22°, 28° and 35° hereby referred to as test dataset) and compared the data estimated by the trained models at these illumination directions.

We use the ΔE_{00} colorimetric difference [13] to compare the estimated and measured data. Table 2 shows the average, maximum and minimum colorimetric difference ΔE_{00} obtained using the test dataset, between the camera measurements and the estimated data for all the samples. Figure 5 shows the histogram plot for the colorimetric difference calculated between the measured and estimated CIEXYZ values for the training dataset of all the samples. The average ΔE_{00} obtained using the Ward model is 1.14 while with CT model is 1.17 with maximum number within the range of 0 to 2.0. From the histogram plot it can be observed that both the models perform well with the image based measurement setup for the samples used in this paper.

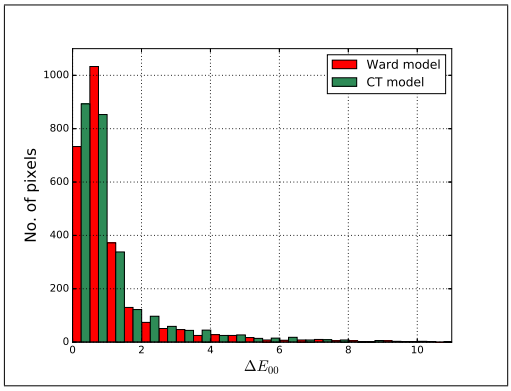

Figure 5. *ΔE_{00} histogram calculated for all the samples measured and estimated at the test dataset illumination angles using CT and Ward model.*

Table 2: Colorimetric difference (ΔE_{00}) between camera measured data and data estimated data using CT and Ward model for all the samples

Material	Avg.ΔE_{00}	Max.ΔE_{00}	Min.ΔE_{00}
CT model			
Munsell white	0.61	3.37	0.06
Red	1.22	9.41	0.03
Cyan	0.91	3.65	0.11
Pantone 10309C	1.11	9.10	0.03
Magenta	1.45	7.47	0.07
Pantone 10213C	1.14	8.76	0.15
Pantone 10153C	1.75	10.86	0.14
Ward model			
Munsell white	0.75	2.16	0.11
Red	1.14	9.61	0.07
Cyan	0.91	3.66	0.12
Pantone 10309C	1.06	9.32	0.02
Magenta	1.44	8.18	0.04
Pantone 10213C	0.99	8.06	0.06
Pantone 10153C	1.69	11.63	0.07

For discussions in this paper, we look at two samples (Cyan and Pantone 10309C) out of these 7 samples measured at one illumination angle (at $\theta_L = 28^\circ$) from the test dataset. Figure 6 and 7 show the plots for the Cyan and Pantone 10309C sample, measured and estimated CIE Y data, using these two models for $\theta_L = 28^\circ$. From the plots it can be observed that both the models work well with the measurement data captured using this setup. In order to evaluate the models colorimetrically, we calculate the ΔE_{00} between the measured data and the estimated data for all the samples. For the viewing range of -40° to $+40^\circ$ where

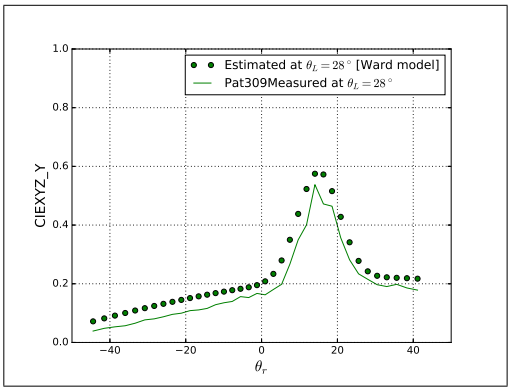

Figure 6. *CIEXYZ Y value, Pantone 10309C sample, measured and estimated at $\theta_L = 28^\circ$ using Ward model.*

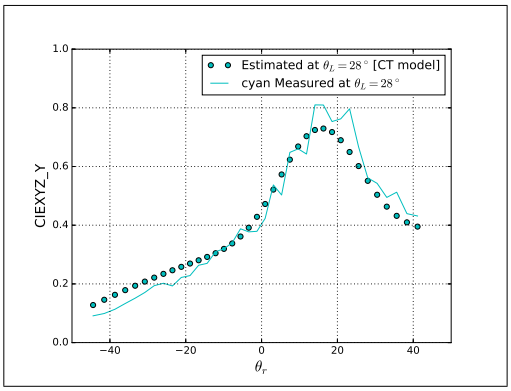

Figure 7. *CIEXYZ Y value, Cyan sample, measured and estimated at $\theta_L = 28^\circ$ using CT model.*

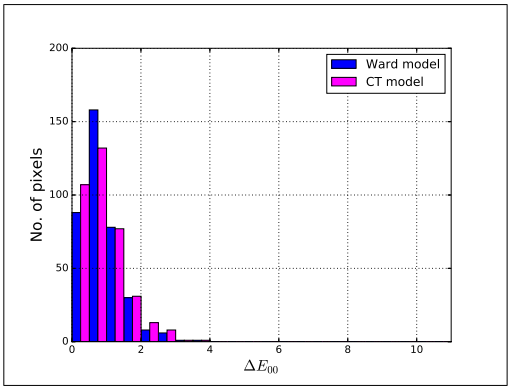

Figure 8. *ΔE_{00} histogram calculated for the Cyan sample CIEXYZ values, measured and estimated at the test dataset illumination angles using CT and Ward model.*

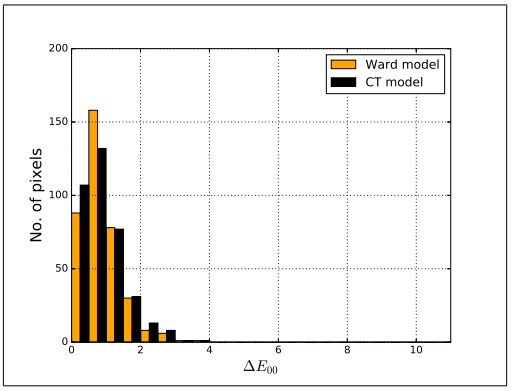

Figure 9. *ΔE_{00} histogram calculated for Pantone 10309C sample CIEXYZ values, measured and estimated at the test dataset illumination angles using CT and Ward model.*

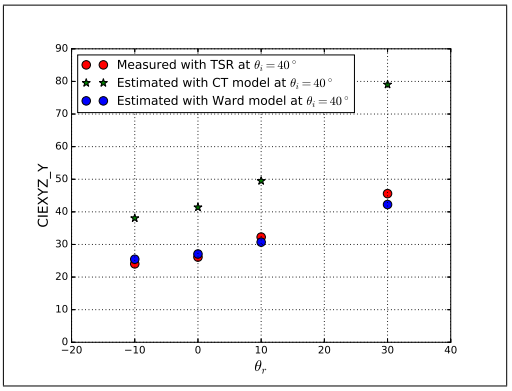

Figure 10. *CIE Y values measured using TSR and estimated using the trained CT and Ward model.*

the camera sensor is normal to the sample at $\theta_r = 0^\circ$, the colorimetric difference obtained shows that we can expect an ok fit using both the models. Figure 8 and 9 show the histogram plots for the colorimetric difference ΔE_{00} between the measured and CT/Ward model estimated CIE Y values for the Cyan and Pantone 10309C sample. The trained models were compared with the physical measurements performed using the manual gonio-setup. Figure 10 shows the plots for the measured CIE Y data (using the TSR setup) and the estimated CIE Y data (using both the trained models) for the Cyan sample at $\theta_i = 40^\circ$ and the viewing directions at which the physical measurements were performed.

Discussions

In this paper we used two BRDF models to evaluate an image based multi-angle measurement setup. In total 7 samples were measured using the image based setup at 10 different illumination directions (θ_L). The samples are print samples of process and spot colours commonly used in package print industry. Wax based inks were used as they show some specularity and can also be processed further to reproduce 2.5D or 3D prints/objects. As

the selected samples showed some specularity but overall were diffuse, we used CT and Ward model. Both the models are simple and easy to implement for the type of samples used in this paper.

Specular and diffuse reflection coefficients along with the roughness coefficient were optimised for both the models using the training dataset. The ΔE_{00} obtained between the test dataset and the estimated values shows that the error can perhaps be reduced further with 1) more careful geometrical and colorimetric calibration of the measurement setup, 2) using optimised illumination direction (θ_L) to train the BRDF models (either increasing the measurement data of reducing to the minimum possible illumination directions that will be sufficient to train the models). The histogram plots for the ΔE_{00} obtained for the complete test dataset gives an understanding that the data captured using the image based measurement setup can, 1) be used to train different BRDF models, 2) estimate the colorimetric output of the material for simulation/reproduction purposes. Measurement data acquired from 5 out of the 10 illumination directions (θ_L) was used as training data set to train both the models and the remaining were used to test the performance of the models. The measured data was divided in half for training and testing purposes. There was no specific reason to choose measurement data from 5 angles as training dataset and the remaining as test dataset.

One sample (Cyan) was measured using a TSR at 4 different viewing directions for a given incident light direction. Using the optimised coefficients for the Cyan sample, the CIE Y value was estimated at the incident and viewing directions used in the TSR measurements. These estimated CIE Y values were compared with the TSR measurements. Looking at the plots (referring to Figure 10) we can see that the ΔY between the measurements (TSR) and the estimated CIE Y value follow the curvature/slope but increases for the last measurement at $\theta_r = 30^\circ$. This can also be observed in the ratio between ΔY and the *CIEY* value. One possible reason for this error could be that we have trained the CT model with measurement data obtained from the image based setup which uses a point light source to illuminate a curved sample. So the measurements obtained have varying illumination and viewing directions for the given pixel points. If we translate the TSR measurement angles to the image based measurement domain, we see that it corresponds to grazing angles in the image based measurement setup with a very low CIE Y corresponding value used to train the model. This also corresponds well with the TSR measurements which has a low CIE Y value at these angles. Another point to note is that the physical measurements performed using the TSR are not very accurate with respect to the incident and viewing direction angles.

Conclusion

Looking at the results obtained, we can conclude that both the models perform satisfactorily using the measurement data captured using the image based multi-angle measurement setup. The CIE Y values estimated using the Ward model performed well compared to the CT model in terms of the colorimetric difference ΔE_{00} obtained. The Ward model also estimates the data very well compared to the TSR measurements.

Future work

As part of the future work it would be important to evaluate the image based measurement setup with gonio-measurements obtained from a gonio-spectrometer setup or multi-angle instruments, where more precise angular measurements can be performed. It would also be important to evaluate the optimal measurement data (training dataset) that can be used to train the models. With respect to the image based measurement setup, using only 1 incident illumination angle (θ_L) would be ideal to train different reflection models.

Acknowledgments

We would like to thank and acknowledge the support of Senior researcher Shoji Tominaga from Chiba University, Post Doctoral Researcher Jean-Baptiste Thomas, Giuseppe Claudio Guarnera, Thomas Simon and Tomas Majtner at the Norwegian Colour and Visual Computing Laboratory in discussions and suggestions regarding the experimental work and structure of this paper.

This work was supported by the MUVApp project N-250293, funded by the Research Council of Norway.

References

[1] J. Rong Lu, J. Koenderink, and A. M. L. Kappers, "Optical properties (bidirectional reflection distribution functions) of velvet," *Applied Optics*, vol. 37, pp. 5974 – 5984, September 1998.

[2] S. R. Marschner, S. H. Westin, E. P. F. Lafortune, K. E. Torrance, and D. P. Greenberg, "Image-based brdf measurement including human skin," in *10th Eurographics Workshop on Rendering*, pp. 139 – 152, 1999.

[3] A. S. Sole, I. Farup, and S. Tominaga, "An image-based multi-directional reflectance measurement setup for flexible objects," in *Measuring, Modeling and Reproducing Material Appearance 2015* (M. V. O. Segovia, P. Urban, and F. H. Imai, eds.), vol. SPIE 9398, pp. 93980J – 93980J–11, Proceedings of SPIE-IS& T Electronic Imaging, 2015.

[4] D. Guarnera, G. Guarnera, A. Ghosh, C. Denk, and M. Glencross, "Brdf representation and acquisition," *Computer Graphics Forum*, vol. 35, no. 2, pp. 625–650, 2016.

[5] F. E. Nicodemus, J. Richmond, J. J. Hsia, I. W. Ginsberg, and T. Limperis, "Geometrical considerations and nomenclature for reflectance." National Bureau of Standards, 1977.

[6] R. L. Cook and K. E. Torrance, "A reflectance model for computer graphics," *ACM Trans. Graph.*, vol. 1, pp. 7–24, Jan. 1982.

[7] B. T. Phong, "Illumination for computer generated pictures," *Commun. ACM*, vol. 18, pp. 311–317, June 1975.

[8] G. J. Ward, "Measuring and modeling anisotropic reflection," *SIGGRAPH Comput. Graph.*, vol. 26, pp. 265–272, July 1992.

[9] E. P. F. Lafortune, S.-C. Foo, K. E. Torrance, and D. P. Greenberg, "Non-linear approximation of reflectance functions," in *Proceedings of the 24th Annual Conference on Computer Graphics and Interactive Techniques*, SIGGRAPH '97, (New York, NY, USA), pp. 117–126, ACM Press/Addison-Wesley Publishing Co., 1997.

[10] A. Sole, I. Farup, and S. Tominaga, "An image based multi-angle method for estimating reflection geometries of flexible objects," *Color and Imaging Conference*, vol. 2014, pp. 91–96, Novemeber 2014-11-03T00:00:00.

[11] A. Sole, I. Farup, and S. Tominaga, "Image based reflectance measurement based on camera spectral sensitivities," *Electronic Imaging*, vol. 2016, no. 9, pp. 1–8, 2016.

[12] J. A. Nelder and R. Mead, "A simplex method for function minimization," *The Computer Journal*, vol. 7, pp. 308 – 313, January 1965.

[13] CIE15.2, “Colorimetry.” CIE standard, 2004.

Author Biography

Aditya Sole completed his bachelors from PVGs College of Engineering and Technology, Pune University, India in year 2005. In 2007 he completed his MSc in Digital Colour Imaging from London College of Communication, University of the Arts, London, UK. From 2008 till 2012 he worked as a Laboratory Engineer at the Norwegian Colour and Visual Computing Laboratory, Gjøvik University College, Gjøvik, Norway. Since, 2012 he is working as a Project Manager and is a PhD student at the Norwegian Colour and Visual Computing.

Title: Evaluating an image based multi-angle measurement setup using different reflection models

Control ID: 2593216

Equation 1 should read as follows:

$$f_{BRDF}(\theta_i, \phi_i; \theta_r, \phi_r, \lambda) = \frac{dL_r(\theta_i, \phi_i; \theta_r, \phi_r; E_i)}{dE_i(\theta_i, \phi_i)}$$

Equation 8 should read as follows:

$$I_P = \begin{bmatrix} I_{P_X} \\ I_{P_Y} \\ I_{P_Z} \end{bmatrix} = I_i \cos\theta_i \left(\begin{bmatrix} R_{d_X} \\ R_{d_Y} \\ R_{d_Z} \end{bmatrix} \frac{1}{\pi} + \frac{k_s}{\sqrt{\cos\theta_i \cos\theta_r}} \frac{e^{[-\tan^2\delta/m^2]}}{4\pi m^2} \right)$$

Figure 9 in the paper should be replaced with the following figure:

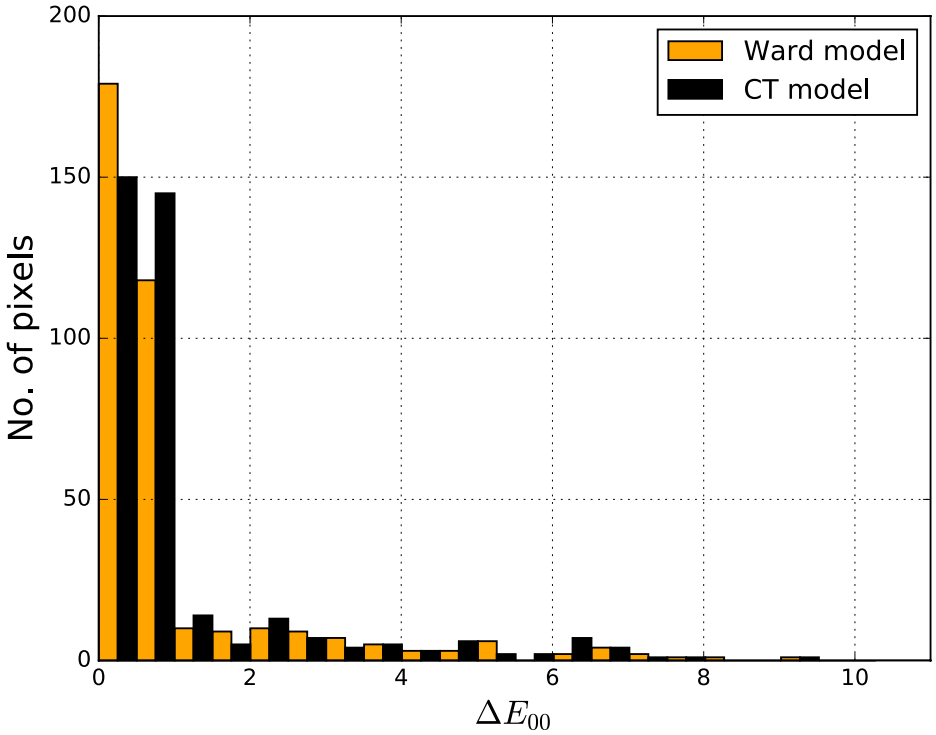

ΔE_{00} histogram calculated for Pantone 10309C sample CIEXYZ values, measured and estimated at the test dataset illumination angles using CT and Ward model.

Paper VI

A. Sole, I. Farup, P. Nussbaum and S. Tominaga, 'Bidirectional reflectance measurement and reflection model fitting of complex materials using an image-based measurement setup', *Journal of Imaging*, vol. 4, no. 11, 136:1–16, 2018

Journal of Imaging

MDPI

Article

Bidirectional Reflectance Measurement and Reflection Model Fitting of Complex Materials Using an Image-Based Measurement Setup

Aditya Sole *, Ivar Farup, Peter Nussbaum and Shoji Tominaga

The Norwegian Colour and Visual Computing Laboratory, Department of Computer Science, Faculty of Information Technology and Electrical Engineering, Norwegian University of Science and Technology, 2815 Gjøvik, Norway; ivar.farup@ntnu.no (I.F.); peter.nussbaum@ntnu.no (P.N.); shoji.tominaga@ntnu.no (S.T.)

* Correspondence: aditya.sole@ntnu.no; Tel.: +47-941-655-42

Received: 8 October 2018; Accepted: 16 November 2018; Published: 20 November 2018

Abstract: Materials with a complex visual appearance, like goniochromatic or non-diffuse, are widely used for the packaging industry. Measuring optical properties of such materials requires a bidirectional approach, and therefore, it is difficult and time consuming to characterize such a material. We investigate the suitability of using an image-based measurement setup to measure materials with a complex visual appearance and model them using two well-established reflection models, Cook–Torrance and isotropic Ward. It was learned that the complex materials typically used in the print and packaging industry, similar to the ones used in this paper, can be measured bidirectionally using our measurement setup, but with a noticeable error. Furthermore, the performance of the reflection models used in this paper shows big errors colorimetrically, especially for the goniochromatic material measured.

Keywords: BRDF measurement; goniochromatic material; colorimetry

1. Introduction

Non-diffuse materials like metallic inks, varnish coatings, and effect paints are widely used in the industry such as for print and packaging to produce a desirable visual appearance of a product. The visual appearance of a material plays an important role in purchase decisions made by the customers.

In traditional printing that uses diffuse material, the color pigments used will absorb part of the incident light, while the rest is diffusely scattered. The perceived color from such pigments is therefore independent of the measurement geometry, and the traditional single geometry 0°:45° measurements are sufficient to characterize these pigments [1]. Non-diffuse materials like metallic ink used in the print industry contain metal flakes that specularly reflect the light incident on it. Pearlescent pigments (pearl interference pigments) usually consist of thin metal oxide layers on transparent mica platelets. The multi-layered structure of these pearlescent pigments contributes to the variation in visual appearance depending on the illumination and viewing direction. They contain a base layer plus multiple layers of metal oxides with varying refractive indices [2]. The change in visual appearance of these pearlescent pigments with respect to the illumination and viewing direction can be controlled by varying the thickness of the metal oxide layer(s) [3,4]. Colour appearance attributes (like hue, chroma, and brightness) of these pigments are therefore dependent on both illumination and viewing directions. Such materials are called 'goniochromatic' [5,6] and are also used in car paint and the cosmetics industry, apart from the print and packaging industry.

Because of the directional properties, bi-directional measurements are needed [5] to characterize such materials. ASTM standards [7,8] provide a measurement geometry guide to measure such materials. Instruments performing bidirectional spectral measurements are commercially available and are termed goniospectrophotometers. A goniospectrophotometer usually measures the ratio of the reflected to incident power (ϕ_r/ϕ_i) over a broad range of illumination and viewing directions. The obtained measurement is then used to compute the bidirectional reflectance distribution function (BRDF) [9], f_r, of a material.

Image-based goniospectrophotometers have been proposed and presented in the past [10–13] to perform bidirectional reflectance measurements in a fast and relatively inexpensive way. However, they are less accurate when compared with slow and expensive techniques similar to the ones used for standardization in metrology. Sole et al. [14] used and evaluated such a measurement setup by measuring fairly diffuse flexible packaging paper samples. The measurements obtained can be used to fit a reflection model (BRDF for an opaque homogeneous material), which will describe the material reflectance properties mathematically for computer graphics rendering or simulating visual appearance attributes.

Many reflection models have been proposed and presented in the past to measure and understand the bidirectional reflectance properties of a given material. Bidirectional reflectance properties of a material are described using a distribution function called the bidirectional reflectance distribution function (BRDF), defined by Nicodemus et al. [9] as:

$$f_r(\theta_i, \phi_i; \theta_r, \phi_r, \lambda) = \frac{dL_r(\theta_i, \phi_i, \theta_r, \phi_r, E_i)}{dE_i(\theta_i, \phi_i)} \quad (1)$$

where $L_r(\theta_i, \phi_i, \theta_r, \phi_r, \lambda)$ is the spectral reflected radiance in the direction (θ_r, ϕ_r), $E_i(\theta_i, \phi_i, \lambda)$ is the spectral irradiance from the direction (θ_i, ϕ_i), and d is the differential. Following the ASTM E2175-01 [15] standard and the CIE 175 [16] technical report, the illumination and viewing directions defined above are in relation to the surface normal, called 'anormal' angles.

An overview of different reflection models was provided by Guarnera et al. [17]. Models can be classified into physical-based and phenomenological models. As described in [17], physical models describe the material physically using micro-facets of different sizes and orientations, while phenomenological models are approximations obtained by fitting the measured data using analytical models. Two well-established models, Cook–Torrance (CT) [18] and isotropic Ward (Ward) [19] have been extensively used to study different sample materials.

To fit such reflection models for isotropic materials, it would be ideal to use in-plane measurement data that will cover all the possible combinations of incident (θ_i) and viewing (θ_r) directions. A virtual gonioreflectometer simulation software was used in [20] to assess different sets of measurement geometries. It was demonstrated that the measurements made at equispaced-angular grid points led to inefficient sampling and were sub-optimal for the different loss functions used. It was proposed that for accurate sampling, a greater number of measurements should be made in the specular region compared to non-specular areas with the understanding that the diffuse part BRDF of the material varies less with the change in illumination and viewing directions compared to the specular part.

In the situation where we use the measurement setup (used in [14]), a greater number of illumination directions (θ_L) would result in a higher number of incident and viewing direction combinations, thus giving a dense sampling and possibly a better estimation of the material BRDF. Measuring the samples at a number of θ_L directions, however, adds to the measurement setup complexity. It would therefore be ideal to use a minimum sampling dataset ((that is, a dataset obtained by illuminating the curved samples using a single illumination direction (θ_L)) to estimate the material BRDF successfully. Nielsen et al. [21] presented a novel method to map BRDF space and to optimize for the best sampling direction. They used the MERLdatabase to test the method and concluded that when using an image-based measurement setup, two illumination directions are enough to characterize the BRDF of a given material. Aittala et al. [22] presented a two-shot method to capture spatially-varying BRDF of a textured material using a mobile camera.

Modeling complex materials present a challenge due to their optical properties, and measuring them bidirectionally using goniospectrophotometers is a time-consuming task. Image-based goniospectrophotometers, similar to the one used by Sole et al. [23,24], can be used for bidirectional measurements, as they can be fast, but might need multiple shots to model such materials due to their goniochromatic and non-diffuse reflectance properties.

In this paper, we investigate the suitability of the image-based measurement setup used in [23–25] to measure such complex materials and model them using well-established reflection models. This setup is well explained in [14,23–25], and we would request the reader to refer to these articles for more details. We use the terminology 'our measurement setup' when referring to this image-based measurement setup. Two reflection models, CT and Ward, are fitted using the measured data, and their performance is compared against a commercially-available goniospectrophotometer (GCMS). Second, we simplify the measurement procedure, when using our measurement setup, by finding the optimal sampling data to fit the reflection models, CT and Ward, for the materials measured in this paper.

2. Method

2.1. Measurement Samples

Three flexible packaging sample materials, a fairly diffuse chromatic packaging print paper sample generated using an OCE ColorWave 600 plotter, referred to as "Red", one metallic gold thin card board commonly used for decorative purposes in packaging, referred to as "Gold", and a goniochromatic sample (a packaging paper printed using effect pigments and varnish coating), referred to as "Blue-Green", were measured using our measurement setup and the GCMS instrument. Looking at the surface properties, the Red and Blue-Green sample were less homogeneous and appeared rougher compared to the Gold sample, which was smoother and uniform.

These samples showed fairly diffuse (Red) to highly specular reflectance properties (Gold and Blue-Green). The Blue-Green sample was non-diffuse and also goniochromatic in nature. It showed a shift in chromaticity with the change in the viewing direction. Figure 1 shows the spectral shift obtained with the change in illumination and viewing direction for the Blue-Green sample. Figure 2 shows the spectral reflectance of all three samples measured using specular included ($di:8^\circ$) and excluded ($de:8^\circ$) measurement geometry. $di:8^\circ$ and $de:8^\circ$ are sphere-based reflectance measurement geometries, as defined in [1], where the sample to be measured is irradiated by an integrating sphere, so that the sample gets irradiated uniformly from all directions within the hemisphere, and the radiation reflected from the sample surface is received at 8° off the sample normal. The difference between specular included ($di:8^\circ$) and excluded ($de:8^\circ$) measurement is that in specular excluded ($de:8^\circ$) geometry, the radiation reflected in the direction of the receiver from the mirror angle is blocked using a black-trap. No difference was observed in the spectral reflectance curve of the Red sample when comparing the specular included and excluded measurements. However, the same was not the case for the Gold and Blue-Green samples. Along with these samples, a Munsell White N9/sheet (MW) that was produced according to the ANSI standards was measured as a reference white.

2.2. BRDF Measurement and Reflection Model Fitting

All three samples were measured using our measurement setup and the GCMS goniospectrophotometer. The measurement output of the GCMS was the radiance factor (β_r). It records the spectral radiance factor in the range of 390 nm–730 nm at 10-nm intervals at anormal incident (θ_i) and reflection (θ_r) angles in the range of $[+80^\circ, -80^\circ]$ at 5° intervals. Please refer to Appendix B in [14] for more details about the GCMS instrument.

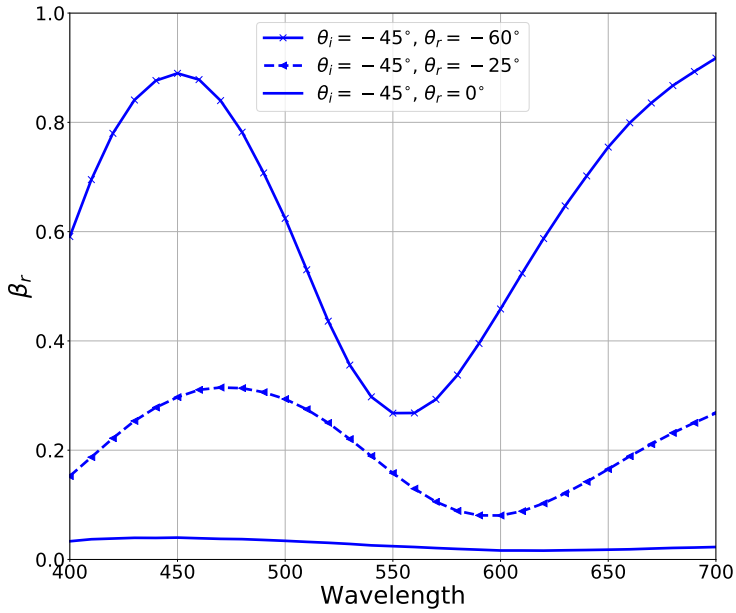

Figure 1. Color shift obtained from the spectral radiance factor measurements of the Blue-Green sample surface using the GCMSinstrument at $\theta_i = -45°$ and $\theta_r = -65°, -25°$ and $0°$. Please note: f_r can be further calculated using the $f_r = \frac{\beta_r}{\pi}$ relation [26].

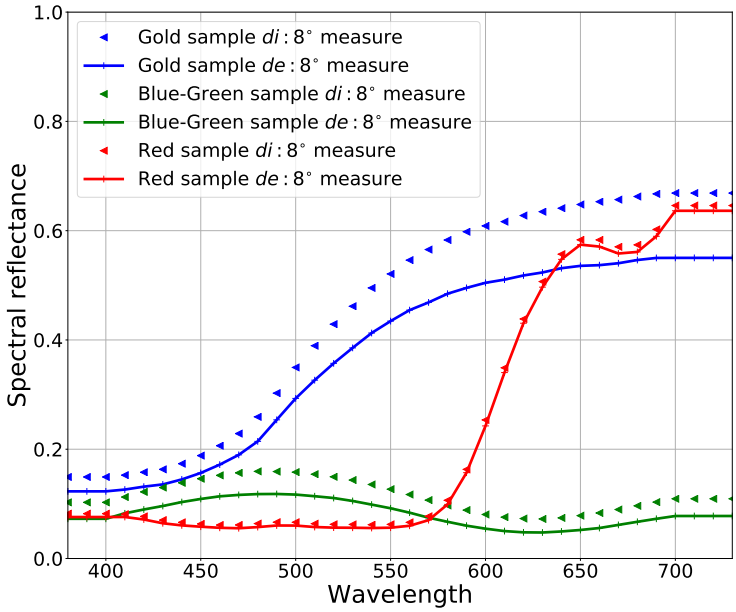

Figure 2. Spectral reflectance measurements using the X-rite SP64 spectrophotometer (with specular included and excluded measurement geometry).

In our measurement setup, the samples were wrapped around a cylinder of known radius and were illuminated and measured respectively using a tungsten point light source and a

commercially-available digital camera (Nikon D200). The detector and the point light source were at a fixed position from the sample curved onto a cylinder of known radius (for example, light source at 45° and detector at 0°). Each point, P, on the curved sample surface made a corresponding incident (θ_i) and viewing (θ_r) angle depending on the illumination direction (θ_L) of the point light source in the setup. Figure 3 shows the setup in a vector plane. Our measurement setup was well explained in [14,23–25], which can be referred to for more details. As discussed in [27], the captured image records the radiance ($L_r(\theta_i, \theta_r)$) exited from the sample surface in digital values for each camera sensor. It saves a 16-bit raw image without any white balance or gamma correction.

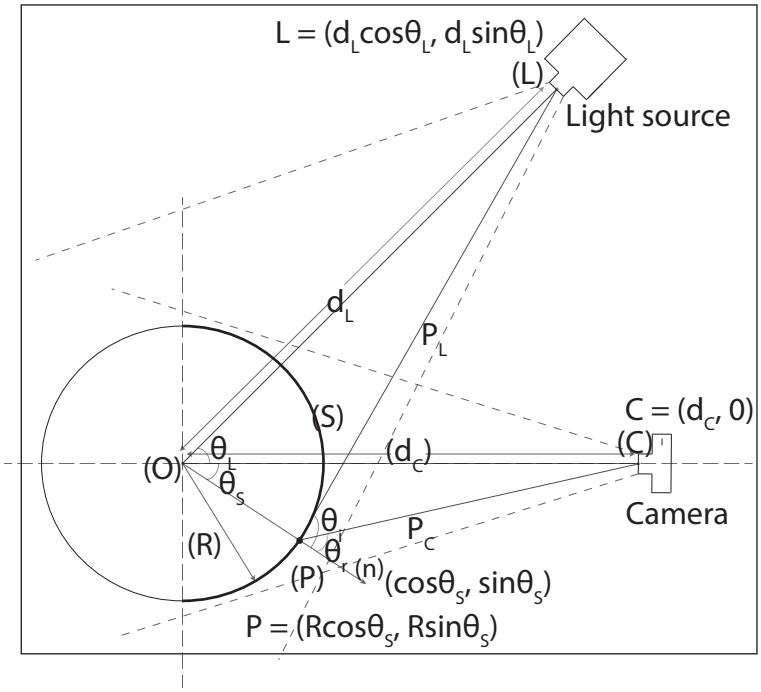

Figure 3. Measurement setup in a vector plane (reprinted with permission of IS&T: The Society for Imaging Science and Technology, sole copyright owners of CIC22: Twenty-second Color and Imaging Conference) [23].

Each pixel in the captured image corresponds to point (P) on the curved sample surface. Five vertical pixels from the sample center for the given point (P) were averaged. Incident (θ_i) and viewing (θ_r) angles at point (P) on the curved sample surface can be calculated using the respective illumination direction (θ_L) information [23]. Please note that even with a single illumination direction (θ_L), that is a single position of the point light source, a whole range of incident (θ_i) and viewing (θ_r) angles was obtained in a single measurement due to the curvature of the sample and the spatial nature of the imaging sensor. MW and the samples were measured at six illumination directions ($\theta_L = -20°$, $-25°$, $-30°$, $-35°$, $-40°$, $-45°$) (see Figure 4).

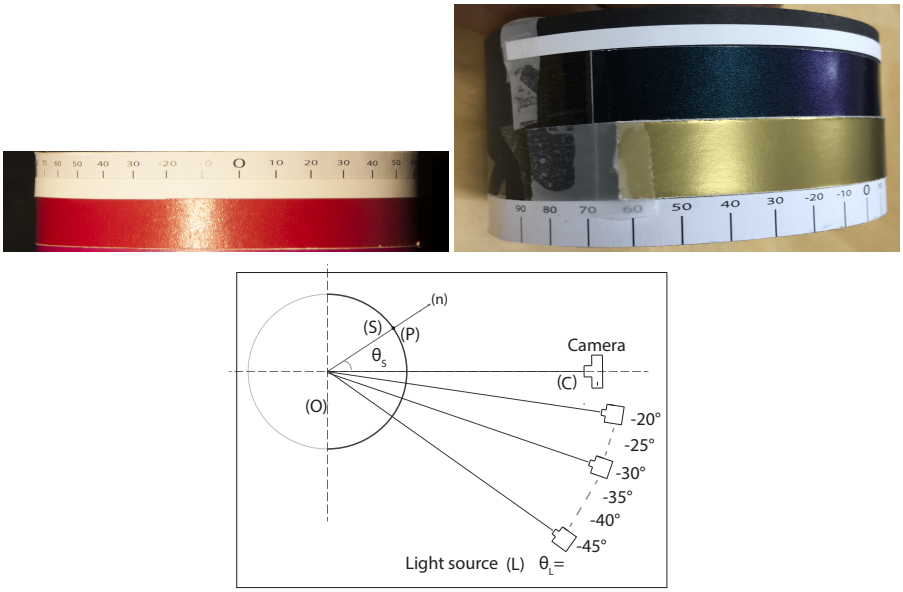

Figure 4. Sample measurement at six different illumination directions (θ_L) and image captured at $\theta_L = -20°$.

Being non-diffuse, for the samples Gold and Blue-Green, it was not possible to record the complete dynamic range in a single exposure image. Both samples were therefore captured at multiple exposures by controlling the shutter speed in the range of 1/2–1/100 s. A high dynamic range image (a radiance map) (HDR) was generated using Debevec and Malik's [28] algorithm. As the obtained HDR image was a radiance map and in order to compare the measurements with the measurements obtained using GCMS, we calculated the radiance factor at the sample surface by using the MW radiance measurements from the same HDR image. As defined in [29] and discussed in [26], the radiance factor (β_r) at the material surface is the ratio of the radiance of that material surface in a given direction to that of a perfect reflecting diffuser (PRD) when both are identically irradiated. The generalized definition of β_r will therefore be as defined in [26] and given in Equation (2).

$$\beta_r(\theta_i, \phi_i, \theta_r, \phi_r, \lambda) = \frac{L_r(\theta_i, \phi_i, \theta_r, \phi_r, \lambda)}{L_r^{PRD}(\theta_i, \phi_i, \theta_r, \phi_r, \lambda)} \quad (2)$$

where L_r and L_r^{PRD} is radiance at the sample and PRD surface, and θ and ϕ are the polar and azimuth angles, respectively. Indexes i and r are incident and reflected radiation. λ denotes the wavelength. As defined in [30], PRD is an ideal isotropic diffuser with reflectance equal to unity. It is known that PRD does not exist in the real world, as it is not possible to have a material with such characteristics. In practice, commercially-available reflection standards (such as a Spectralon tile) that have a traceable calibration to a transfer standard at the material supplier are used [26]. As the samples were wrapped around a cylinder and illuminated using a point light source in our measurement setup, using a flat Spectralon tile (similar to how it was used in [25]) will not be precise, as both the wrapped sample and flat Spectralon tile will not be irradiated identically. The Spectralon tile being physically inflexible, the curved sample and the Spectralon tile will be irradiated identically only at a single illumination and viewing direction, thus requiring further assumptions about the homogeneity of the light source used. We therefore use a Munsell White N9/ sheet produced according to ANSI standards to calculate the radiance factor at the sample surface.

As the samples and the MW are wrapped around the cylinder (see Figure 4), one below the other, vertically, any given point (P) on the MW surface will have the same incident (θ_i) and viewing angle

(θ_r) (with respect to the point light source and the detector) as at point (P) on the sample surface. We assume the MW as a PRD, and using the definition of radiance factor (β_r) (see Equation (2)), we calculated β_r at the sample surface using Equation (3).

$$\beta_r(\theta_i;\theta_r) = \frac{L_{rSample}(\theta_i,\theta_r)}{L_{rMW}(\theta_i,\theta_r)} \tag{3}$$

In Equation (3), $L_{rSample}$ and L_{rMW} is the in-plane radiance measurement at the sample surface and the MW surface, respectively. Both surfaces were irradiated identically using the point light source in the measurement setup. The Red sample being a diffuse sample, a single exposure image was sufficient to calculate β_r using MW measurements and Equation (3).

Figure 5 shows the incident and viewing directions at which the samples were measured using GCMS and our measurement setup. Each diagonal line represents the illumination direction (θ_L) used in our measurement setup. GCMS measures at 1° near specular angles, while at 5° intervals away from the specular direction.

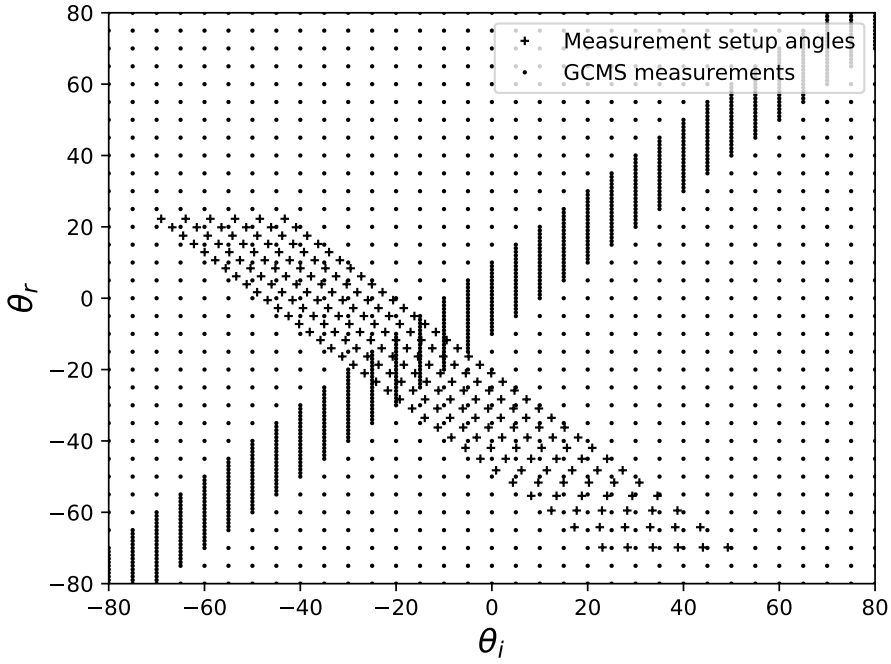

Figure 5. θ_i and θ_r angles at which measurements are performed using our measurement setup and GCMS.

Measurements made using GCMS and our measurement setup had different dimensions. GCMS measurement dimensions were $n \times m \times 35$, where n and m are the incident (θ_i) and reflection (θ_r) angles at the sample surface. The measurement unit was a spectral radiance factor in the range of 390 nm–730 nm at 10-nm intervals; whereas, measurements performed using our measurement setup were per pixel, where each pixel corresponds to the curved sample surface point (P), thus making a unique incident and reflection angle relative to the surface normal. The measurement data obtained consisted of 3 channels (R, G, and B). As we used a high resolution camera, the measurement points (P) (or the θ_i and θ_r angle combinations) were many (approximately 1000 pixels horizontally) and different compared to the GCMS measurements. Please note that the measurement setup measurements are sampled at every 20 pixels for visual representation in Figure 5.

In order to compare both measurements, we converted the radiance factor measurements performed with our measurement setup into a camera color domain (camera RGB domain) using Equation (4).

$$\begin{aligned} \beta_{R_{setup}} &= k \cdot f_{r_{Rsetup}} \cdot \sum_{\lambda=400nm}^{700nm} \bar{r}(\lambda) \cdot I_i(\lambda), \\ \beta_{G_{setup}} &= k \cdot f_{r_{Gsetup}} \cdot \sum_{\lambda=400nm}^{700nm} \bar{g}(\lambda) \cdot I_i(\lambda), \\ \beta_{B_{setup}} &= k \cdot f_{r_{Bsetup}} \cdot \sum_{\lambda=400nm}^{700nm} \bar{b}(\lambda) \cdot I_i(\lambda), \\ k &= \frac{100}{\sum_{\lambda 400nm}^{700} \bar{g}(\lambda) \cdot I_i(\lambda)} \end{aligned} \tag{4}$$

where k is a normalizing coefficient, $f_{r_{RGBsetup}}$ is the sample radiance factor obtained from Equation (3) for each camera channel. $\bar{r}$, $\bar{g}$, and $\bar{b}$ are the spectral sensitivities of the camera used as a detector, and $I_i(\lambda)$ is spectral light intensity normally incident on the sample. Spectral camera sensitivities ($\bar{r}$, $\bar{g}$, $\bar{b}$) were measured using a monochromator as described in [27]. $I_i(\lambda)$ was estimated using the relative normalization method described in [31] and implemented in [14].

Similarly, we converted measurements performed using GCMS to the camera RBG domain using Equation (5).

$$\begin{aligned} \beta_{R_{GCMS}} &= k \cdot \sum_{\lambda=400nm}^{700nm} f_{r_{GCMS}}(\lambda) \cdot \bar{r}(\lambda) \cdot I_i(\lambda), \\ \beta_{G_{GCMS}} &= k \cdot \sum_{\lambda=400nm}^{700nm} f_{r_{GCMS}}(\lambda) \cdot \bar{g}(\lambda) \cdot I_i(\lambda), \\ \beta_{B_{GCMS}} &= k \cdot \sum_{\lambda=400nm}^{700nm} f_{r_{GCMS}}(\lambda) \cdot \bar{b}(\lambda) \cdot I_i(\lambda), \\ k &= \frac{100}{\sum_{\lambda 400nm}^{700} \bar{g}(\lambda) \cdot I_i(\lambda)} \end{aligned} \tag{5}$$

In Equation (5), k, $\bar{r}$, $\bar{g}$, $\bar{b}$, and $I_i(\lambda)$ are similar to those used in Equation (4). $f_{r_{GCMS}}$ is the sample radiance factor measured using the GCMS goniospectrophotometer.

To compare sample measurements from both the instruments directly, we can interpolate the camera RGB measurements calculated using GCMS measurements in Equation (5) at the incident and reflection angles of our measurement setup using a standard piece-wise cubic spline interpolation method. The sample measurements obtained can be used to train different reflection models.

Both the CT and Ward model consist of a diffuse and a specular reflection component along with a roughness parameter that controls the width of the specular component. Considering the diffuse and non-diffuse reflectance properties of the Red and Gold sample, we trained the CT and Ward model by optimizing the diffuse (K_d) and specular reflection coefficient (K_s) individually for each channel (R, G, B), while only a single roughness (m) parameter across all three channels, as shown in Equations (6) and (7) respectively.

$$\beta_p = \begin{bmatrix} \beta_{p_R} \\ \beta_{p_G} \\ \beta_{p_B} \end{bmatrix} = \begin{bmatrix} K_{s_R} \\ K_{s_G} \\ K_{s_B} \end{bmatrix} \cdot R_s + \begin{bmatrix} K_{d_R} \\ K_{d_G} \\ K_{d_B} \end{bmatrix}$$

$$R_s = \frac{F \cdot D \cdot G}{\pi(\mathbf{n} \cdot \mathbf{l})(\mathbf{n} \cdot \mathbf{v})} \tag{6}$$

$$G = \min\left\{1, \frac{2\,(\mathbf{n} \cdot \mathbf{h})\,(\mathbf{n} \cdot \mathbf{v})}{(\mathbf{v} \cdot \mathbf{h})}, \frac{2\,(\mathbf{n} \cdot \mathbf{h})\,(\mathbf{n} \cdot \mathbf{l})}{(\mathbf{v} \cdot \mathbf{h})}\right\}$$

$$D = \frac{1}{m^2 \cos^4 \alpha} e^{-[(\tan \alpha)/m]^2}$$

$$\beta_p = \begin{bmatrix} \beta_{p_R} \\ \beta_{p_G} \\ \beta_{p_B} \end{bmatrix} = \begin{bmatrix} K_{d_R} \\ K_{d_G} \\ K_{d_B} \end{bmatrix} \cdot \frac{1}{\pi} + \begin{bmatrix} K_{s_R} \\ K_{s_G} \\ K_{s_B} \end{bmatrix} \cdot \frac{1}{\sqrt{\cos \theta_i \cos \theta_r}} \cdot \frac{e^{\left[-\tan^2 \alpha / m^2\right]}}{4\pi m^2} \tag{7}$$

where R_s, D, G, and F are as defined in Equation (6) and [18]. F is assumed to be one; θ_i = the angle between the illumination direction and normal to the sample surface; θ_r = the angle between the viewing direction and normal to the sample surface; $k_{s_{R,G,B}}$ = the specular reflection coefficient of the sample material per channel; R_s = the specular reflectance component, K_d = the diffuse reflection coefficient; $\alpha = \mathbf{n} \cdot \mathbf{h} = \cos((\theta_i - \theta_r)/2)$ at the given pixel point (P) in the used measurement setup; $\mathbf{n} \cdot \mathbf{l} = \cos \theta_i$; and $\mathbf{n} \cdot \mathbf{v} = \cos \theta_r$.

For the Blue-Green sample, we optimized the roughness coefficient (m) individually for each channel (RGB) along with the specular (K_s) and diffuse (K_d) component, as defined in Equations (8) and (9). G is same as defined in Equations (6).

$$\beta_p = \begin{bmatrix} \beta_{p_R} \\ \beta_{p_G} \\ \beta_{p_B} \end{bmatrix} = \begin{bmatrix} K_{s_R} \cdot R_{s_R} \\ K_{s_G} \cdot R_{s_G} \\ K_{s_B} \cdot R_{s_B} \end{bmatrix} + \begin{bmatrix} K_{d_R} \\ K_{d_G} \\ K_{d_B} \end{bmatrix}$$

$$R_{s_{RGB}} = \frac{F \cdot D_{RGB} \cdot G}{\pi(\mathbf{n} \cdot \mathbf{l})(\mathbf{n} \cdot \mathbf{v})} \tag{8}$$

$$D_{RGB} = \frac{1}{m_{RGB}^2 \cos^4 \alpha} e^{-[(\tan \alpha)/m_{RGB}]^2}$$

$$\beta_p = \begin{bmatrix} \beta_{p_R} \\ \beta_{p_G} \\ \beta_{p_B} \end{bmatrix} = \begin{bmatrix} K_{d_R} \\ K_{d_G} \\ K_{d_B} \end{bmatrix} \cdot \frac{1}{\pi} + \begin{bmatrix} K_{s_R} \\ K_{s_G} \\ K_{s_B} \end{bmatrix} \cdot \frac{1}{\sqrt{\cos \theta_i \cos \theta_r}} \cdot \begin{bmatrix} \frac{e^{\left[-\tan^2 \alpha / m_R^2\right]}}{4\pi m_R^2} \\ \frac{e^{\left[-\tan^2 \alpha / m_G^2\right]}}{4\pi m_G^2} \\ \frac{e^{\left[-\tan^2 \alpha / m_B^2\right]}}{4\pi m_B^2} \end{bmatrix} \tag{9}$$

The Nelder–Mead down-hill simplex algorithm [32] was used to optimize the coefficients using the RMS error (β_{Err}) as defined in Equation (10).

$$\beta_{Err} = \sqrt{(\beta_{R_{Pmea}} - \beta_{R_{Pest}})^2 + (\beta_{G_{Pmea}} - \beta_{G_{Pest}})^2 + (\beta_{B_{Pmea}} - \beta_{B_{Pest}})^2} \quad (10)$$

$\beta_{pR_{mea}}$, $\beta_{pG_{mea}}$, and $\beta_{pB_{mea}}$ are the radiance factor measurements in the camera RGB domain obtained using Equations (4) and (5) for the three channels, while $\beta_{pR_{est}}$, $\beta_{pG_{est}}$, $\beta_{pB_{est}}$ are the radiance factor measurements (again in the camera RGB domain) of the sample calculated using the fitted CT and Ward models.

2.3. Optimal Sampling Dataset

When collecting the sampling dataset using our measurement setup, it was important to use the best and least possible illumination directions (θ_L) to fit the reflection models successfully. This would help towards reducing the measurement complexity and performing fast measurements. We, therefore, fit both the models using the sampling dataset collected from all combinations (63 in total) of the six illumination directions (θ_L), respectively. The obtained model parameters were then used to estimate the bidirectional reflectance measurements in the camera RGB domain (β_{RGB}).

3. Results

Figure 6 shows the measured (using GCMS) and predicted (using the fitted reflection models) camera RGB G-channel data.

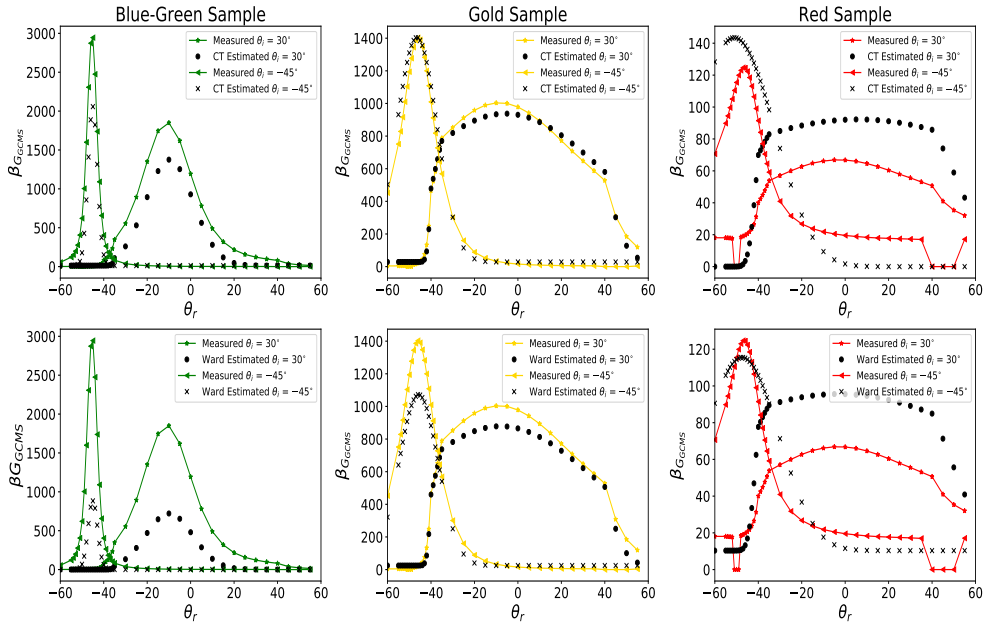

Figure 6. G-channel camera RGB data measured using GCMS and estimated using models fitted with the data set captured with $\theta_L = -25°$ using our measurement setup.

The relative error (ΔErr_P) was calculated, using Equation (11), between camera RGB data that were calculated using the measured data and predicted using the fitted reflection models for the respective channel.

$$\Delta Err_P = \frac{\sum_p \mid \beta_{P_{mea}} - \beta_{P_{est}} \mid}{\sum_p \beta_{P_{mea}}} \quad (11)$$

In Equation (11), $\beta_{P_{mea}}$ is camera RGB data calculated from measurements, and $\beta_{P_{est}}$ is camera RGB data estimated using the fitted reflection models.

Using measurements made with our measurement setup, we fit both the reflection models, CT and Ward, with sampling data obtained from all the possible combinations (63 in total) of the incident light directions ($\theta_L = -20^\circ - -45^\circ$), respectively.

Figure 7 shows box-and-whisker plots for average relative error (ΔErr_P) calculated using Equation (11) for the G-channel between camera RGB data calculated from GCMS measurements and data estimated using both the reflection models fitted with different combinations of sampling data. The box-and-whiskers plots show that the error variation was reduced to some extent when a bigger sampling dataset was used (from a single illumination direction (θ_L) to two θ_L directions) to fit the models. However, in many cases, the optimization algorithm converged to a local minimum instead of a global minimum when finding the reflection model parameters using the cost function given in Equation (10). This can also be seen in the results shown in Figure 7.

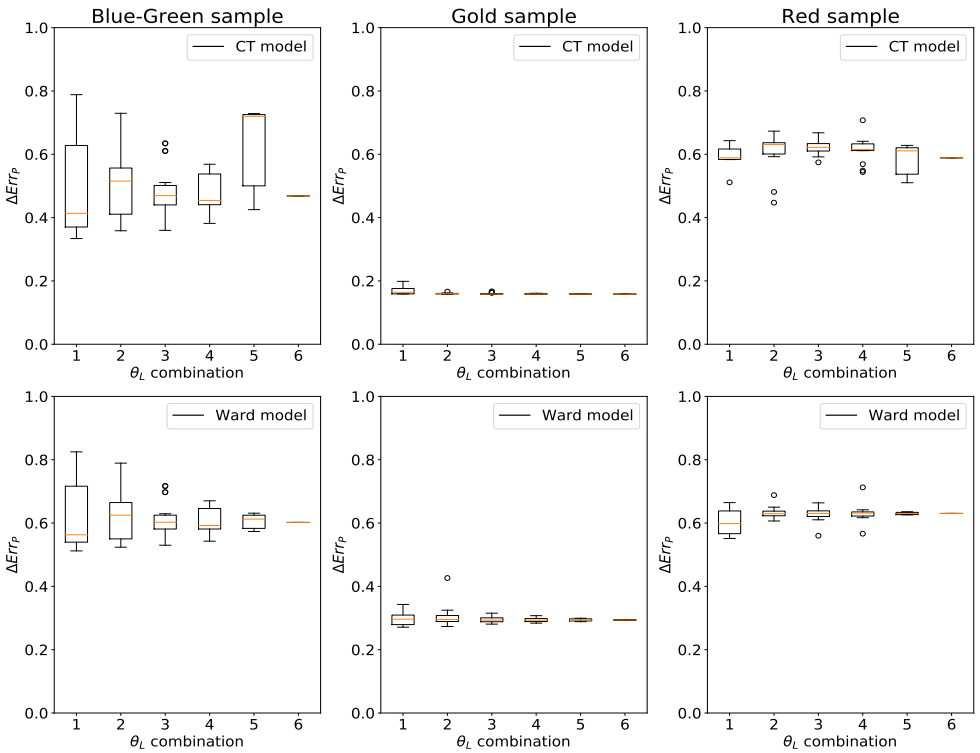

Figure 7. Box-and-whisker plots showing ΔErr_P between G-channel camera RGB data calculated from GCMS measurements and data estimated using both models of all the samples. The orange line in the boxes shows the median error value obtained between the θ_L combinations used for model fitting. Circle dots are large ΔErr_P error obtained (approximately three-times the range of error variation (boxes) obtained). CT, Cook–Torrance.

One of the objectives of our measurement setup being bidirectional reflectance measurement of goniochromatic materials, we colorimetrically evaluated the setup by calculating CIE1976 $u'v'$ uniform chromaticity coordinates [1] from the obtained camera RGB data. We converted the obtained camera RGB data to the CIEXYZ colorimetric space using a transformation matrix ($\hat{M}$). $\hat{M}$ was calculated using the camera spectral sensitivities and CIE 2° color matching functions, as described

in [27]. The obtained CIEXYZ values were then transformed into CIE1976 $u'v'$ uniform chromaticity coordinates using Equation (12).

$$u' = \frac{4 \cdot X}{X + 15 \cdot Y + 3 \cdot Z'}, \quad v' = \frac{9 \cdot Y}{X + 15 \cdot Y + 3 \cdot Z} \tag{12}$$

Figure 8 shows the CIE1976 $u'v'$ values from measured (using GCMS) and predicted (using the fitted reflection models) values for all the samples. The total number of measurements being many, we present below CIE1976 $u'v'$ plots for all the samples measured (with GCMS) and predicted using reflections models fitted with the dataset captured with our measurement setup at a single illumination direction ($\theta_L = -45°$).

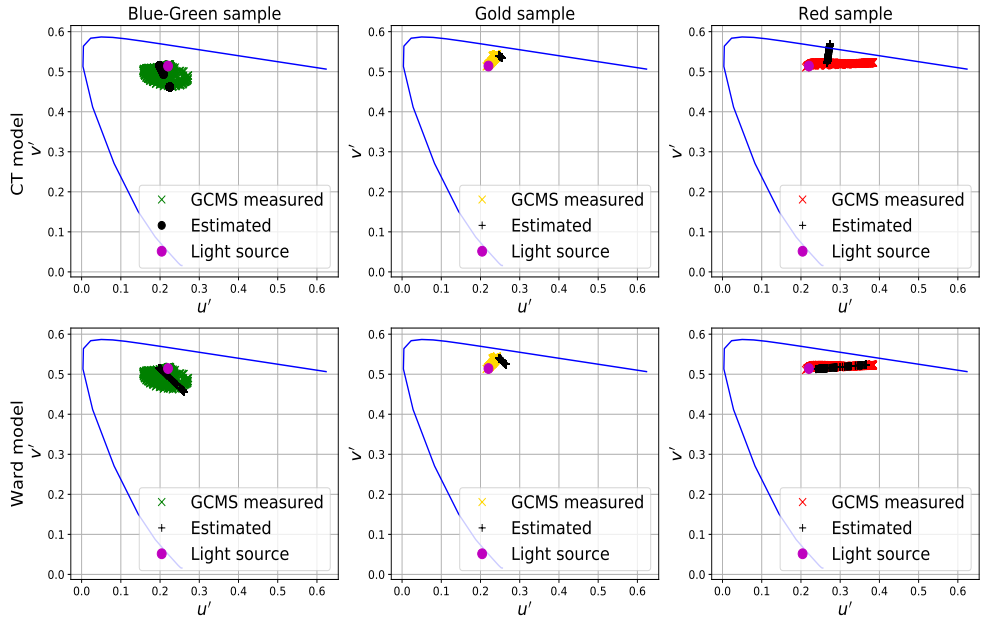

Figure 8. CIE1976 $u'v'$ uniform chromaticity coordinates calculated using Equation (12) for all the samples measured with GCMS and estimated from reflection models trained using the dataset obtained from our measurement setup with one illumination direction ($\theta_L = -45°$).

The relative error ($\Delta E_{u'v'}$) was calculated using Equation (13) between CIE1976 $u'v'$ coordinates obtained from the measured and predicted camera RGB data.

$$\Delta E_{u'v'} = \left(\frac{\sqrt{\left(u'_{mea} - u'_{est}\right)^2}}{u'_{mea}} + \frac{\sqrt{\left(v'_{mea} - v'_{est}\right)^2}}{v'_{mea}} \right) \tag{13}$$

where u'_{mea} and v'_{mea} are the CIE1976 $u'v'$ coordinates obtained from the measured β_r data and u'_{est} and v'_{est} were obtained from β_r estimated using the reflection models. Figure 9 shows box-and-whisker plots for the average relative error calculated using Equation (13) for all the samples. Samples were measured using GCMS and predicted using both reflection models fitted with the datasets obtained using all (63) combinations of θ_L directions in our measurement setup.

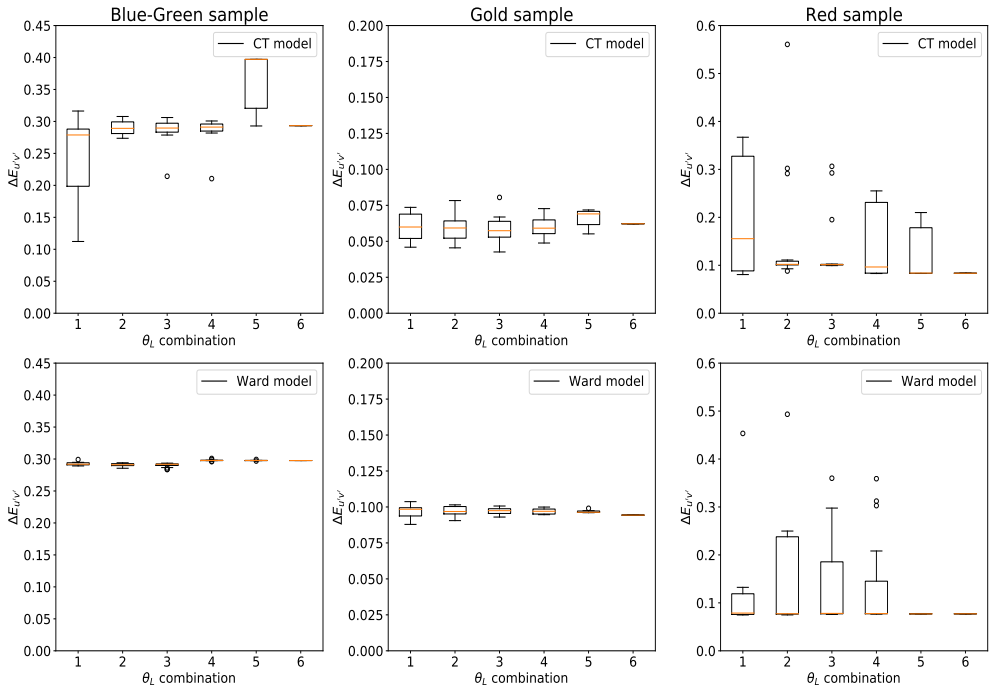

Figure 9. Box-and-whisker plots showing average $\Delta E_{u'v'}$ between camera RGB data calculated from GCMS measurements and data estimated using both models of all the samples. The orange line in the boxes shows the median error value obtained between the θ_L combinations used for model fitting. Circle dots are large $\Delta E_{u'v'}$ error obtained (approximately three-times the range of error variation (boxes) obtained).

The median error remained fairly constant for all three samples with the increase in the number of measurements to fit the reflection models. Adding more illumination directions did not improve the fitting performance colorimetrically. Modeling goniochromatic materials using the CT and Ward model was difficult given the nature of these models, and it would be more appropriate to use a mixture of BTFand BRDF models.

4. Discussion

This paper investigates the suitability of measuring materials with a complex visual appearance bidirectionally using our measurement setup. The setup is evaluated against measurements made using a commercially available goniospectrophotometer (GCMS). Two well-established reflection models are fitted using sampling data obtained from our measurement setup. Figure 6 shows the G-channel camera RGB data measured and estimated using the GCMS instrument and the fitted reflection models, respectively. It can be seen that the performance of the CT model was better compared to the Ward especially for the Blue-Green material and Gold sample. Estimated BRDF values match well with the measurements for the Gold sample for non-grazing illumination and viewing directions.

Box-and-whisker plots shown in Figure 7 show a similar result, with the performance of CT being better for all the samples. The variation in the error value was much higher (maximum error value (ΔErr_p) of 0.8), for the Blue-Green sample G-channel measurements when we used a minimum sampling dataset (that is, the dataset collected using a single θ_L in our measurement setup). The median relative error obtained was around 0.4 (using the CT model), which is a fairly big error.

The error was even higher for the Ward model (median relative error of almost 0.6). Similar results were obtained for the Red sample with a median relative error around 0.6 for both, CT and Ward, reflection models. For the Gold sample, the median relative error was approximately 0.2 for both the reflection models, which is much smaller compared to the Blue-Green and Red sample. Using a bigger sampling dataset for any of the samples or the reflection models did not reduce the error variation significantly. In many cases, the optimization algorithm did converge to a local minimum instead of a global minimum, thus adding to the uncertainty in fitting the models.

Overall, the relative error was large for Blue-Green and Red material compared to Gold. Some of the possible reasons for having less error for the Gold sample are the material being smoother and uniform. Furthermore, the Gold sample can be called uni-modular, which shows a big change in intensity compared to hue and chroma for different illumination (θ_i) and viewing (θ_r) directions.

The CIE 1976 $u'v'$ chromaticity coordinates were calculated from the camera RGB data for colorimetric evaluation. The performance of both models was similar for the Blue-Green and Gold samples, but with less variation in the relative $\Delta E_{u'v'}$ error when using the Ward model. Colorimetrically, the performance was not good for either of the models for the Blue-Green sample. Variation in the relative error ($\Delta E_{u'v'}$) was small with the Ward model compared to CT for the Gold and Blue-Green samples. Colorimetrically, both models struggled to predict the Blue-Green sample. One of the possible reasons for this is that we had constant diffuse reflection components ($K_{d_{RGB}}$) trained using the measured data, while the Blue-Green sample showed a shift in color depending on the viewing direction. Another observation made using the analysis was that the sample measurements showed retro-reflection, which cannot be modeled using CT and Ward. Furthermore, the relative error (ΔErr_p) obtained was maximum at the grazing angles, which the models struggled to predict.

The samples also being non-diffuse (similar to the Gold sample) added the further complexities of a dynamic range and the need to capture a high dynamic range image. Capturing an HDR image adds to measurement error and uncertainty, as the accuracy of the radiance map will depend on the fusion algorithm. The need to capture an HDR image also reduces the measurement speed and limits the use of such a measurement setup to measure the BRDF of complex materials.

A Munsell White sheet (MW) was used as a reference white standard when calculating the radiance factor from the measurements obtained using our measurement setup. MW is a white paper material reproduced by following the ANSI specifications according to the Munsell color system. In practice, commercially-available reflection standards such as a Spectralon tile are used in reference instruments or commercially-available goniospectrophotometers like GCMS. The tiles are spectrally calibrated with high accuracy, and double beam measurements are performed to record the bidirectional radiance factor on the sample surface, resulting in a very precise measurement. The MW sheet is not as precise as a Spectralon tile as a reference white standard and can contribute to measurement error. As discussed in detail in [26], performing absolute calibration would be the most appropriate method to obtain accurate radiance factor measurements. This, however, is difficult to implement in the industry, where performing measurements in a fast and inexpensive way is expected. When performing measurements using our measurement setup, using a Spectralon tile that can be curved onto the cylinder along with the material to be measured would be one of the methods to perform BRDF calculations. This way, it would be possible to follow the definition to have both the sample and the Spectralon tile irradiated identically. It was not possible to obtain a Spectralon tile that could be used in this way, and therefore, we attempted in this paper to use a Munsell white N9/sheet that was produced according to the ANSI standards. Furthermore, if we use a flat Spectralon tile, it would only be valid for a single incident (θ_i) and viewing (θ_r) angle combination in our measurement setup, and we would have to make further assumptions about the homogeneity of the light source. With the MW, this was avoided. Using MW as a reference white standard in our measurement setup is a known source of error, which needs to be addressed in future work.

There are many factors that contribute to the total error when fitting both models. Some of the error sources with respect to our measurement setup were identified in [14]. HDR image capture

will further add to the setup error when measuring complex materials along with the reference white standard to be used for radiance factor calculations. This will need further study, measurements and analysis.

5. Conclusions

Complex materials with different reflectance properties are measured using our measurement setup. The setup is evaluated using two well-established reflections models. The measurement procedure, when using our measurement setup, is simplified by evaluating optimal sampling data that can be used to fit the reflection models for the complex materials measured. A commercial goniospectrophotometer is used to evaluate the performance of the model fitting and to investigate the feasibility to use our measurement setup to measure complex materials.

Though the error obtained is fairly big, the estimated BRDF of the non-diffuse and goniochromatic material measured look similar to the GCMS measurements, especially at the non-grazing angles. Colorimetrically, both models struggle with the Blue-Green sample. The Gold sample showed less relative error compared to the Red and Blue-Green samples, possibly due to its surface properties being smoother and homogeneous compared to the Red and Blue-Green samples. Using more sampling data (in terms of illumination directions (θ_L)) did not reduce the median error significantly, though the error variation was reduced to some extent. We learned that the complex materials typically used in the print and packaging industry, similar to the ones used in this paper, can be measured using our measurement setup, but with a noticeable error.

Author Contributions: Supervision, I.F. and P.N.; Writing—original draft, A.S.; Writing—review & editing, A.S., I.F., P.N. and S.T.

Funding: This work was supported by the MUVAppProject N-250293, funded by the Research Council of Norway.

Acknowledgments: We would like to thank and acknowledge support of Reiner Eschbach, Jean-Baptiste Thomas, and Giuseppe Claudio Guarnera, at the Norwegian Colour and Visual Computing Laboratory, in discussions and suggestions regarding the structure of this paper.

Conflicts of Interest: The authors declare no conflict of interest.

References

1. *Colorimetry*; CIE15.2; CIE Standard; CIE Publication: Paris, France, 2004.
2. Maile, F.J.; Pfaff, G.; Reynders, P. Effect pigments—Past, present and future. *Prog. Org. Coat.* **2005**, *54*, 150–163. [CrossRef]
3. Klein, G.A. *Industrial Color Physics*; Springer Series in Optical Sciences; Springer: New York, NY, USA, 2010.
4. Tomić, I.; Dedijer, S.; Novaković, D.; Jurič, I. Artificial neural networks for optimizing camera-based color measurements of prints enhanced with pearlescent pigments. *Color. Technol.* **2018**, *134*, 364–372. [CrossRef]
5. McCamy, C. Observation and measurement of the appearance of metallic materials. Part I. Macro appearance. *Color Res. Appl.* **1996**, *21*, 292–304. [CrossRef]
6. Eugène, C. MEASUREMENT OF "total visual appearance": A CIE challenge of soft metrology. In Proceedings of the 12th IMEKO TC1 and TC7 Joint Symposium on Man, Science and Measurement, Annecy, France, 3–5 September 2008; pp. 61–65.
7. *Standard Practise for Multiangle Color Measurement of Interference Pigments*; ASTM-E2539; ASTM Standard; American Society for the Testing of Materials: West Conshohocken, PA, USA, 2012.
8. *Standard Practise for Multiangle Color Measurement of Metal Flake Pigmented Materials*; ASTM-E2194; ASTM Standard; American Society for the Testing of Materials: West Conshohocken, PA, USA, 2012.
9. Nicodemus, F.E.; Richmond, J.; Hsia, J.J.; Ginsberg, I.W.; Limperis, T. *Geometrical Considerations and Nomenclature for Reflectance*; National Bureau of Standards; US Department of Commerce: Washington, DC, USA, 1977.
10. Rong Lu, J.; Koenderink, J.; Kappers, A.M.L. Optical properties (bidirectional reflection distribution functions) of velvet. *Appl. Opt.* **1998**, *37*, 5974–5984.

11. Marschner, S.R.; Westin, S.H.; Lafortune, E.P.F.; Torrance, K.E.; Greenberg, D.P. Image-Based BRDF Measurement Including Human Skin. In Proceedings of the Eurographics Workshop, Granada, Spain, 21–23 June 1999; pp. 139–152.
12. Tominaga, S.; Tanaka, N. Estimating reflection parameters from a single color image. *IEEE Comput. Gr. Appl.* **2000**, *20*, 58–66. [CrossRef]
13. Matusik, W.; Pfister, H.; Brand, M.; McMillan, L. A Data-Driven Reflectance Model. *ACM Trans. Gr.* **2003**, *22*, 759–769. [CrossRef]
14. Sole, A.; Farup, I.; Nussbaum, P.; Tominaga, S. Evaluating an image-based bidirectional reflectance distribution function measurement setup. *Appl. Opt.* **2018**, *57*, 1918–1928. [CrossRef] [PubMed]
15. *Standard Practice for Specifying the Geometry of Multiangle Spectrophotometers*; ASTM-E2175; ASTM Standard; American Society for the Testing of Materials: West Conshohocken, PA, USA, 2013.
16. *A Framework for the Measurement of Visual Appearance*; CIE175; Technical Report; International Commission on Illumination: Vienna, Austria, 2006.
17. Guarnera, D.; Guarnera, G.; Ghosh, A.; Denk, C.; Glencross, M. BRDF Representation and Acquisition. *Comput. Gr. Forum* **2016**, *35*, 625–650. [CrossRef]
18. Cook, R.L.; Torrance, K.E. A Reflectance Model for Computer Graphics. *ACM Trans. Gr.* **1982**, *1*, 7–24. [CrossRef]
19. Ward, G.J. Measuring and Modeling Anisotropic Reflection. *SIGGRAPH Comput. Gr.* **1992**, *26*, 265–272. [CrossRef]
20. Langovoy, M.; Schmähling, F.; Wübbeler, G. Numerical comparison of sampling strategies for BRDF data manifolds. *Measurement* **2016**, *94*, 578–584. [CrossRef]
21. Nielsen, J.B.; Jensen, H.W.; Ramamoorthi, R. On Optimal, Minimal BRDF Sampling for Reflectance Acquisition. *ACM Trans. Gr.* **2015**, *34*. [CrossRef]
22. Aittala, M.; Weyrich, T.; Lehtinen, J. Two-shot SVBRDF capture for stationary materials. *ACM Trans. Gr.* **2015**, *34*, 110:1–110:13. [CrossRef]
23. Sole, A.; Farup, I.; Tominaga, S. An image based multi-angle method for estimating reflection geometries of flexible objects. In *Color and Imaging Conference*; Society for Imaging Science and Technology: Springfield, VA, USA, 2014; Volume 2014, pp. 91–96.
24. Sole, A.S.; Farup, I.; Tominaga, S. An image-based multi-directional reflectance measurement setup for flexible objects. In *Measuring, Modeling and Reproducing Material Appearance 2015*; Segovia, M.V.O., Urban, P., Imai, F.H., Eds.; International Society for Optics and Photonics: Bellingham, WA, USA, 2015; Volume 9398, p. 93980J. [CrossRef]
25. Sole, A.; Farup, I.; Nussbaum, P. Evaluating an image based multi-angle measurement setup using different reflection models. *Electron. Imaging* **2017**, *2017*, 101–107. [CrossRef]
26. Höpe, A.; Hauer, K.O. Three-dimensional appearance characterization of diffuse standard reflection materials. *Metrologia* **2010**, *47*, 295. [CrossRef]
27. Sole, A.; Farup, I.; Tominaga, S. Image based reflectance measurement based on camera spectral sensitivities. *Electron. Imaging* **2016**, *2016*, 1–8. [CrossRef]
28. Debevec, P.E.; Malik, J. Recovering High Dynamic Range Radiance Maps from Photographs. In Proceedings of the 24th Annual Conference on Computer Graphics and Interactive Techniques, Los Angeles, CA, USA, 11–15 August 2008; ACM Press/Addison-Wesley Publishing Co.: New York, NY, USA, 1997; pp. 369–378. [CrossRef]
29. Palmer, J.; Grant, B.G. *The Art of Radiometry*; SPIE Press Bellingham: Washington, DC, USA, 2010; ISBN 978-0-8194-7245-8.
30. CIE. *International Lightning Vocabulary 4th edn CIE Publication 17.4*; CIE Publication: Paris, France, 1987.
31. Li, H.; Foo, S.C.; Torrance, K.E.; Westin, S.H. Automated three-axis gonioreflectometer for computer graphics applications. *Opt. Eng.* **2006**, *45*, 043605. [CrossRef]
32. Nelder, J.A.; Mead, R. A Simplex Method for Function Minimization. *Comput. J.* **1965**, *7*, 308–313. [CrossRef]

Paper VII

A. Sole, G. C. Guarnera, I. Farup and P. Nussbaum, 'Measurement and rendering of complex non-diffuse and goniochromatic packaging materials', *Manuscript submitted for publication*, 2019

Contents lists available at ScienceDirect

Computers & Graphics

journal homepage: www.elsevier.com/locate/cag

Measurement and rendering of complex non-diffuse and goniochromatic packaging materials

ARTICLE INFO

Article history:

Keywords: BRDF measurement, Rendering, Goniochromatism, Genetic Algorithm, Retro-reflection, Visual appearance

ABSTRACT

Realistic renderings of materials with complex optical properties, such as goniochromatism and non-diffuse reflection, are difficult to achieve. In the context of the print and packaging industries, accurate visualisation of the complex appearance of such materials is a challenge, both for communication and quality control.

In this paper, we characterise the bidirectional reflectance of two homogeneous print samples displaying complex optical properties. We demonstrate that in-plane retro-reflective measurements from a single input photograph, along with genetic algorithm based BRDF fitting, allow to estimate an optimal set of parameters for reflectance models, to use for rendering. While such a minimal set of measurements enables visually satisfactory renderings of the measured materials, we show that a few additional photographs lead to more accurate results, in particular for samples with goniochromatic appearance.

1. Introduction

Materials like non-diffuse metallic-paints, varnish coatings, and effect paints have complex optical properties that produce fascinating appearance in manufactured products. Metallic paints contain metal flakes, causing the incident light to be specularly reflected. Materials like effect paints, containing pearlescent pigments, are made using thin metal oxide layers on transparent mica platelets [1]. The multi-layered structure of pearlescent pigments helps increasing changes in visual appearance of a material, with respect to the incident and viewing directions [1], including angle dependent spectral reflectance [2]. These materials, often referred as "goniochromatic" [3, 4], are commonly used in the print and packaging industry.

Such materials are produced using different printing techniques (*e.g.* offset, gravuer, screen printing [2]) and contribute to some of the main challenges in the printing line, including:

1. performing fast and easy process control measurements;
2. synthetically reproduce and match visual properties of such goniochromatic packaging materials for customer approval and quality control;
3. communicate material appearance across production and quality control departments in a print production line.

The visual appearance of goniochromatic print and packaging materials typically require Bidirectional Reflectance Distribution Function (BRDF) measurements, in order to properly characterise and communicate the properties during print production. Commercially available devices, such as multi-angle spectrophotometers and goniospectrophotometers, could be used to perform such bidirectional measurements [2]. However, such devices prove to be slow and relatively expensive, therefore not suited for inline measurements in the production process.

Image-based measurements [5] could represent an efficient, fast and a practical method to accurately estimate bidirectional reflectance, also in the context of the print and packaging industries, able to satisfy the needs of control and inline quality evaluation. Furthermore, back-scattering measurements often provide enough information to analytically characterise the reflectance properties of a given material [6, 7, 8], while additional measurements can improve the initial estimates [9].

Building upon the above, in this paper we measure the BRDF of print samples using a small set of salient measurement taken with a simple, low cost image-based setup, easy to integrate

in inline quality evaluation for print and packaging industries. These measurements are used to estimate the optimal set of parameters of a commonly used BRDF model [10], by means of a Genetic Algorithm (GA) based BRDF fitting method. We demonstrate that even for print samples showing goniochromatic optical properties, typically challenging to capture, we are able to obtain visually satisfactory renderings.

The main contributions of this paper are:

1. the use of common BRDF models to successfully represent the appearance of non-diffuse, goniochromatic print samples described in this paper;
2. retro-reflective in-plane measurements as a key to successfully represent the appearance of non-diffuse packaging print samples;
3. a GA BRDF fitting method, rather than the commonly used Nelder-Mead down-hill simplex algorithm, to obtain the optimal set of BRDF model parameters.

Along with the print samples, we use an additional non-diffuse sample, "Blue Metallic Paint" (BMP), from the MERL dataset [11]. The BMP material is used to asses the performance of in-plane BRDF measurements as opposite to a full measurement dataset, to faithfully represent the appearance of materials with visual characteristics comparable to the print samples measured. Finally, we compare measurements taken using our setup with the ones of a commercially available goniospectrophotometer.

2. Background and related work

The reflectance properties of an opaque material can be described using the BRDF, defined by Nicodemus et al. [12] as

$$f_r(\mathbf{l},\mathbf{v}) = \frac{dL_r(\mathbf{v})}{dE_i(\mathbf{l})} = \frac{dL_r(\mathbf{v})}{L_i(\mathbf{l})\cos\theta_i d\omega_i} \tag{1}$$

In Equation (1), $\mathbf{l}$ and $\mathbf{v}$ are incident and viewing direction unit vectors, E_i is incident spectral irradiance, L_i is incident spectral radiance (flux per unit area, per unit solid angle (ω_i)), L_r is the reflected spectral radiance and d is the differential. The unit of a BRDF is inverse steradian $[1/sr]$. There exist a variety of possible designs for BRDF measurement setups [5]; measured data can be left in tabular form, or represented in a compact way by means of BRDF models, either phenomenological or physically based, depending upon the specific needs of the application. For a recent survey on the taxonomy of BRDF measurement setups and reflectance models, we refer the reader to a recent survey by Guarnera *et al.* [5].

A number of image-based measurement setups, which make use of one or more cameras as sensors, have been proposed [13, 14, 15, 16, 17], since they allow to perform bidirectional measurements in a fast and relatively inexpensive way. The setup presented in [17] used image-based measurements to measure anisotropic materials like velvet by wrapping it around a cylinder in different orientations. An image-based measurement setup similar to the one from [17] was used in [18] to investigate the suitability of an image-based measurement setup to measure the reflectance of isotropic packaging materials, representing their BRDF using well-know reflectance models, such as Cook-Torrance [19] and isotropic Ward [20]. Three flexible packaging materials, with different optical properties ranging from fairly diffuse to goniochromatic, were measured using their setup and a commercially available goniospectrophotometer; both their setup and the goniospectrophotometer cannot measure retro-reflectance. For BRDF fitting, the Nelder-Mead down-hill simplex algorithm [21] was used, along with a RMS-based error cost function. Their results show a large relative error, in particular for the goniochromatic print sample, due to the optimisation algorithm converging to local minima in most cases. In [18] both BRDF models used have 3 free parameters (in the Cook-Torrance model this is enforced using a constant Fresnel term $F = 1$). Phenomenological and physically-based models with a higher yet reasonable amount of free parameters, could provide better generalisation properties for packaging materials.

The Lafortune model [22], is a generalisation of cosine lobe based models, such as Phong [23]. It allows increased flexibility, thanks to the weighted dot product, and follows both reciprocity and energy conversation principles of a BRDF. The generalisation is achieved using a 3×3 matrix, in which the direction vectors are defined to a fixed local co-ordinate system with respect to the surface normal. Lafortune model presented in Equation (2) is one of the simplest forms to use. With six parameters, $\rho_d, \rho_s, C_x, C_y, C_z$ and α, Lafortune model is more flexible compared to the Ward model, is computationally efficient and expressive to fit complex reflectances. In Equation (2), ρ_d is the diffuse, and, ρ_s the specular albedo. C_x, C_y, C_z, and α controls the shape and orientation of the specular lobe, retro-reflection (with C_x, C_y, C_z as positive), and anisotropy (with $C_x \neq C_y$). $l_{x,y,z}$ and $v_{x,y,z}$ are direction components of the incident ($\mathbf{l}$) and viewing ($\mathbf{v}$) direction vectors.

$$f_r(\mathbf{l},\mathbf{v}) = \frac{\rho_d}{\pi} + \rho_s \left[C_x l_x v_x + C_y l_y v_y + C_z l_z v_z \right]^{\alpha} \tag{2}$$

Löw et al. [10] introduced two isotropic models for accurate and efficient rendering of glossy surfaces, either based on the Rayleigh-Rice light scattering theory or on the micro-facet theory; both models makes use of a modified version of the ABC model [24, 25]. In particular, the micro-facet model introduced in [10] Equation (3) is based on the Cook-Torrance model [19]:

$$f_r(\mathbf{l},\mathbf{v}) = \frac{k_d}{\pi} + \frac{S(\sqrt{1-(\mathbf{n}\cdot\mathbf{h})}F(\theta_h)G(\mathbf{n}\cdot\mathbf{l},\mathbf{n}\cdot\mathbf{v})}{(\mathbf{n}\cdot\mathbf{l})(\mathbf{n}\cdot\mathbf{v})} \tag{3}$$

In Equation (3), G and F are the geometrical attenuation and Fresnel factors as defined in [19] and given below in Equation 5 and 6 respectively. θ_h is the half angle between the normal and the halfway vector $\mathbf{h}$, $\mathbf{l}$ and $\mathbf{v}$ are the incident and viewing direction vectors, $\mathbf{n}$ is a normal at a point on the surface and k_d is the scaling parameter for the diffuse component. Finally, S is the ABC-based micro-facet distribution, reported in Equation (4):

$$S(f) = \frac{A}{(1+Bf^2)^C}, \tag{4}$$

In the above equation, which represents a non-normalised distribution, B and C respectively controls the width of the specular peaks and the fall-off rate of wide-angle scattering, while

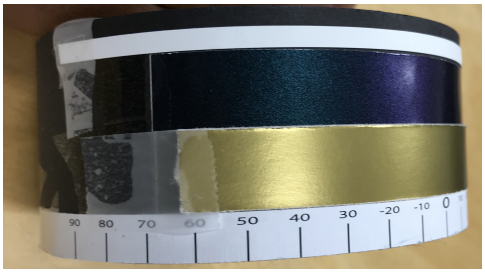

Fig. 1. The two flexible samples used in our paper, wrapped around a cylinder, used in our measurement setup.

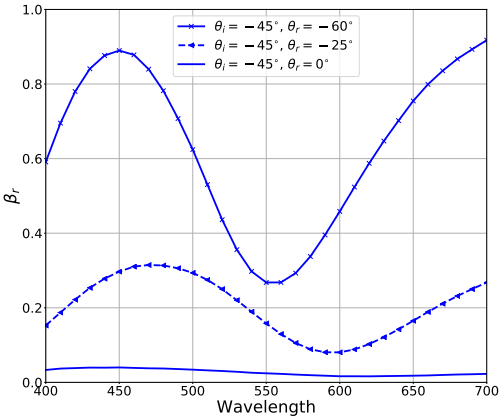

Fig. 2. Colour shift obtained from the spectral radiance factor measurements of the Blue-Green sample surface when measured at different viewing directions [18].

A is a scaling factor for the specular component. f is defined as $\sqrt{f_x^2 + f_y^2}$ where, $f_x = (\sin\theta_r \cos\phi_r - \sin\theta_i)/\lambda$ and $f_y = (\sin\theta_r \sin\phi_r)/\lambda$. λ is wavelength of the incident light.

$$G = \min\left\{1, \frac{2(\mathbf{n}\cdot\mathbf{h})(\mathbf{n}\cdot\mathbf{v})}{(\mathbf{v}\cdot\mathbf{h})}, \frac{2(\mathbf{n}\cdot\mathbf{h})(\mathbf{n}\cdot\mathbf{l})}{(\mathbf{v}\cdot\mathbf{h})}\right\} \quad (5)$$

$$F = \frac{(g-c)^2}{2(g+c)^2}\left\{1 + \frac{[c(g+c)-1]^2}{[c(g-c)+1]^2}\right\} \quad (6)$$

In Equation (6), $c = \mathbf{v}\cdot\mathbf{h}$, $g = \eta^2 + c^2 - 1$ and η is the index of refraction. In the following, we will refer to the model described by Equation (3) as "ABC model".

3. Method

3.1 Measurement samples

In our paper, we focus our attention on the two flexible packaging samples reported in Figure 1. The Gold sample is a metallic gold thin cardboard commonly used for decorative purposes in print and packaging industry while, the Blue-Green sample is a packaging paper printed using effect pigments and varnish coatings. Both samples are non-diffuse with the Blue-Green sample also being goniochromatic. Figure 2 shows the spectral shift in the Blue-Green sample with the change in viewing direction. A Munsell white N9/ sheet (MW), produced according to the ANSI standards, was measured along with Gold and the Blue-Green sample. The MW measurements are used as a reference white for bidirectional reflectance calculations from the sample measurements obtained from our measurement setup. Along with the print samples, a non-diffuse paint sample, BMP, from the MERL dataset [16] is used to asses the performance of in-plane BRDF measurements against a full BRDF measurement dataset to successfully represent appearance of the print samples.

3.2 BRDF measurement setup

Our measurement setup for flexible samples is schematically represented in Figure 3. In order to measure a sample, this is wrapped around a cylinder of known radius. Each point on the curved sample surface corresponds to an incident (θ_i) and reflection (θ_r) angle with respect to the surface normal and incident direction (θ_L) of the light source in the setup. Our setup performs in-plane measurements (azimuthal angles $\phi_i = \phi_r = 0$) and the captured image records the radiance ($L_r(\theta_i, \theta_r)$) exited from the sample surface in terms of digital pixel values (R,G,B) with respect to the camera sensors ($\bar{r}$, $\bar{g}$, $\bar{b}$). 'TOP VIEW' in Figure 3 shows a schematic diagram of our measurement setup. Print samples were measured at four different illumination directions ($\theta_L = 0°, -20°, -30°$, and $-40°$) (refer Figure 3). In order to capture retro-reflected light from the sample surface, $\theta_L = 0°$ incident light direction was used during the measurements. Due to setup limitations it was not possible to have incident light direction ($\theta_L = 0°$) in-plane with the camera as it blocks the camera view. In order to overcome this limitation, the samples were measured at approximately $\phi_L = 4.6°$ (refer 'SIDE VIEW' in Figure 3). The azimuthal angle ($\phi_L = 4.6°$) being small, we have considered these measurements as in-plane with $\phi_i = \phi_r = 0°$.

Print samples were measured using both our measurement setup and the goniospectrophotometer (GCMS) instrument. GCMS instruments records the spectral radiance factor (390nm - 730nm at 10nm intervals) at anormal incident (θ_i) and reflection (θ_r) angles in the range of $+80°$ to $-80°$ at $5°$ intervals. GCMS uses a tungsten halogen light bulb as a light source and a silicon photo-diode array as a detector. The sample to be measured is positioned flat on a plate, which rotates between anormal angles $\pm 80°$ with respect to incident light source that is normal to the sample surface. Automatic correction for the change in illumination and viewing area due to sample rotation is done by the instrument with radiance factor as a measurement output. The reference white plate used in the instrument is assumed as a perfect reflecting diffuser and therefore we calculate sample BRDF using $\beta = \pi f_r$. Please refer to Murakamis GCMS-3B Goniospectrophotometric Color Measurement System manual[1]

[1] Gcms-3 goniospectrophotometer system, `http://www.aviangroupusa.com/pdf/GCMS3_Des.pdf`. Accessed: 2019-06-18

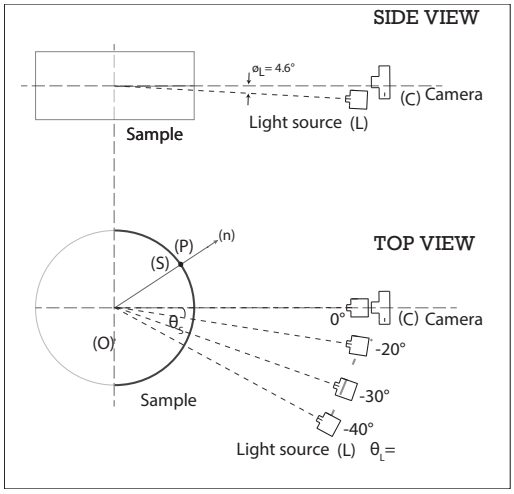

Fig. 3. Sample measurements: with our setup, we take measurements at four different illumination directions (θ_L).

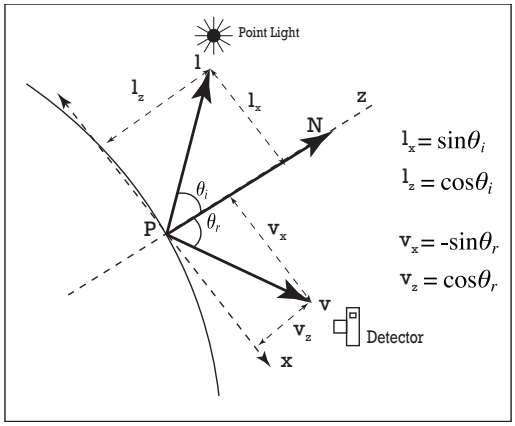

Fig. 4. Directional vectors in the co-ordinate system used in our setup, with respect to the surface normal at point (P) on the curved sample surface.

for details and specifications of this instrument.

Following the definition of radiance factor from [26, 27] and the discussions in [27], we calculate the bidirectional reflectance for the sample using Equation (7).

$$f_r(\theta_i, \phi_i, \theta_r, \phi_r, \lambda) = \frac{\pi L_r(\theta_i, \phi_i, \theta_r, \phi_r, \lambda)}{L_r^{PRD}(\theta_i, \phi_i, \theta_r, \phi_r, \lambda)} \tag{7}$$

In Equation (7), L_r and L_r^{PRD} is radiance at the sample and the perfect reflecting diffuser (PRD) surface. θ and ϕ are the polar and azimuth angles respectively. Indexes i and r are incident and reflected radiation and λ is the wavelength. PRD not being real, in practice, reference white materials like the spectralon tile that can be traceable to a metrological reference or a transfer standard is commonly used as a PRD [24]. We use the MW, which is wrapped around the cylinder along with the Gold and Blue-Green sample, as a PRD in Equation (7).

3.3 BRDF fitting

Choice of the fitting metric

Estimating the optimal set of the parameters for a reflectance model, given an optimisation algorithm, cost function and the measured reflectance data, is a common task to allow extrapolating material BRDF data, for instance in rendering. However, as reported for in [10], the choice of the cost function for fitting is not obvious, and depends also on the sample to be measured and the reflectance model used. Print samples, such as the ones used in [18], show non-diffuse and goniochromatic properties which are a challenge to visualise. Due to these complex optical properties we use two different metrics as cost functions when optimising the model parameters. The cost function, M_1, given in Equation (8), uses a $\cos\theta_i$ assuming an uniform incoming radiance at the sample surface thus weighing the error more in the specular region [17].

$$M_1 = \sum_{RGB} \sqrt{\frac{\sum_P \left[(f_{r_m}(\mathbf{l}, \mathbf{v}) \cos\theta_i) - (f_{r_e}(\mathbf{l}, \mathbf{v}) \cos\theta_i) \right]^2}{P}} \tag{8}$$

In Equation (8), f_{r_m} and f_{r_e} is the bidirectional reflectance measured and estimated using the reflectance model respectively. θ_i is the anormal incident angle. The cost function M_2 as defined by Löw et al. [10] and given in Equation (9) uses a logarithmic function with the understanding that it will yield a better visual reproduction of wide-angle scattering compared to the M_1 metric.

$$M_2 = \sum_{RGB} \sqrt{\frac{\sum_P \left[\ln(1 + f_{r_m}(\mathbf{l}, \mathbf{v}) \cos\theta_i) - \ln(1 + f_{r_e}(\mathbf{l}, \mathbf{v}) \cos\theta_i) \right]^2}{P}} \tag{9}$$

In Equation (9), similar to the M_1 cost function, f_{r_m} and f_{r_e} are the bidirectional reflectance measured and estimated using the reflectance model respectively and θ_i is the anormal incident angle.

The BRDFs of the print samples, as well as the BMP sample (from the MERL dataset), were estimated using an optimal set of BRDF parameters for the two reflectance models described in Section 2, Lafortune [22] and micro-facet model by Löw et al. [10]. The print samples were measured both using our setup and the GCMS instrument.

Lafortune model

Figure 4 shows the directional vectors of the Lafortune model, in our setup co-ordinate system. Since both our setup and the GCMS instrument perform in-plane measurements, and the samples used are isotropic ($C_x = C_y = C_{xy}$), Equation (2) can be re-written as in Equation (10), where we report also the normalisation factor used.

$$f_{r_{RGB}}(\mathbf{l}, \mathbf{v}) = \frac{\rho_{d_{RGB}}}{\pi} + \frac{\alpha + 2}{2\pi \left[\max\left(|C_{xy}|, |C_z| \right) \right]^\alpha} \left[-C_{xy} \sin\theta_i \sin\theta_r + C_z \cos\theta_i \cos\theta_r \right]^\alpha \tag{10}$$

where diffuse (ρ_d) and specular (ρ_s) albedo are optimised per channel. The Lafortune model parameters $\rho_{d_{RGB}}$, $\rho_{s_{RGB}}$, C_{xy}, C_z

and α, were optimised using M_1 cost function, Nelder-Mead down-hill simplex algorithm [21] as the optimisation tool, and the measured data from our setup (all θ_L directions); additionally, measurement from the GCMS instrument were used for comparisons.

ABC model

Using individual diffuse (ρ_d) and specular (ρ_s) component albedo per channel, the micro-facet ABC model from Equation (3) can be re-written as given in Equation (11) to estimate the sample BRDF.

$$f_r(\mathbf{l},\mathbf{v}) = \frac{k_{d_{RGB}}}{\pi} + \frac{S_{RGB}\left(\sqrt{1-(\mathbf{n}\cdot\mathbf{h})}\right) F(\theta_h)\, G(\mathbf{n}\cdot\mathbf{l}, \mathbf{n}\cdot\mathbf{v})}{(\mathbf{n}\cdot\mathbf{l})(\mathbf{n}\cdot\mathbf{v})} \tag{11}$$

S_{RGB} is the modified ABC distribution with parameter A (in S_{RGB}) being used as a scaling parameter per channel for the specular component albedo and $k_{d_{RGB}}$ is the diffuse component albedo.

To find a salient measurement dataset for analytically estimating material BRDF using the micro-facet ABC model, we performed in total eight optimisation's consisting of two cost functions (M_1 and M_2), and four different measurement data subsets. These data subsets were part of the measurements made for each samples using our setup, as detailed in the following:

1. Measurement Setup measurements at illumination direction $\theta_L = 0°$ (retro-reflection measurements),
2. Measurement Setup measurements at illumination direction $\theta_L = 0°$ and $-40°$ (retro-reflective plus an additional direction to further improve the analytical estimate),
3. Measurement Setup measurements at all illumination directions, $\theta_L = 0°, -20°, -30°, -40°$.

In addition to the above, for each print sample we fitted the GCMS measurements. For the BMP sample, in-plane measurements from the MERL dataset were used, testing both cost functions described in the above.

Estimating an optimal set of ABC model parameters using Nelder-Mead down-hill simplex algorithm proved to be difficult, as A in (S_{RGB}) is not normalised. The model parameters, $k_{d_{RGB}}$, A_{RGB} (in S), B, C, and η (in F), were therefore optimised for the three samples using the M_1 and M_2 cost functions and the GA method instead, as detailed in the next subsection.

Fitting algorithm

When using an optimisation algorithm, given a range of possible model parameter values, the algorithm calculates the minimum cost function value to obtain an optimal set of model parameters. Using algorithms like the Nelder-Mead down-hill simplex or Powells may lead to one or many local minima if the objective function used is non-convex. To address this issue, a GA-based method can be used instead, in particular in situations where a large number of BRDF model parameters need to be optimised. It is a classical evolutionary algorithm, which can be used to optimise a large number of variables in both constrained or unconstrained non-linear systems. GA methods have been successfully used in computer graphics, to derive new BRDF models [28] and for image-based BRDF parameter remapping [29]. In the context of BRDF fitting, among their potential advantages there are the increased probability to have in output a set of parameters derived from a global minimum of the fitting metric. Furthermore, GA do not require the user to specify an initial guess of the parameters, which might prove to be particularly difficult in case of goniochromatic materials and BRDF models with many parameters, given that the latter not always have a clear effect on material appearance [29].

The parameters range has a significant impact both on the quality of the solution and on the fitting time. This is particularly true for the ABC model, in which the micro-facet distribution is not normalised and the parameters controlling it (A, B and C) do not have a clear upper bound. To address this issue, we rely on the fitting results available in the supplemental material of [10], assuming that the range of the ABC parameters derived by fitting the MERL dataset allows to represent most materials. Analogous considerations about the gamut of the MERL dataset have been used in previous work([11, 30]).

4. Results

Mitsuba renderer [31] was used to render the estimated BRDFs of the materials. To display our results, we used the geometry and lighting described in Havran *et al.* [32]. Figures 9, 10 and 11 show the renderings obtained using the optimised reflectance models, and are discussed in section 5.

Figure 5 shows the results using the optimised Lafortune model parameters obtained with measurements from our setup (all θ_L directions) and the GCMS instrument. When optimising Lafortune model parameters, Nelder-Mead down-hill simplex algorithm converged to a local minimum making it difficult to obtain an optimal set of the model parameters. As the samples are isotropic, we use the Lafortune model with the condition $C_x = C_y$, which forces the cost function to converge to a minimum when the C_x and C_z parameter values get interchanged resulting into a local minima. This makes it challenging to optimise the Lafortune model parameters using just in-plane measurements made by the Measurement Setup. Similar was the case using the measurements from the GCMS instrument and also for the BMP sample with in-plane measurements. We therefore did not optimise the Lafortune model parameters further using M_2 cost function, the GA method and different measurement datasets. Figure 6 shows the results using the optimised micro-facet ABC model parameters model fittings for the micro-facet ABC model optimised with measurement dataset obtained from the Measurement Setup and the GCMS instrument. To assess the performance of using in-plane BRDF measurements instead of the full BRDF, optimal model parameters were obtained for the BMP sample using in-plane measurements and the reflectance models. Figure 7 shows the model fittings for the BMP sample.

To objectively evaluate a salient measurement dataset used to analytically estimate material BRDF, relative error (Err) was calculated using Equation (12) which calculates a relative error using the maximum value in the measurements. In Equation (12), f_{r_m} represents the measurements obtained using the

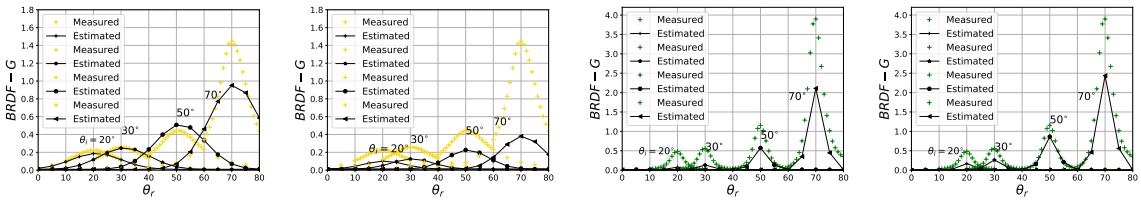

(a) Cost function: M_1, Dataset: Measurement Setup (θ_L = ALL)

(b) Cost function: M_1, Dataset: GCMS instrument

(c) Cost function: M_1, Dataset: Measurement Setup (θ_L = ALL)

(d) Cost function: M_1, Dataset: GCMS instrument

Fig. 5. G-channel Gold [(a) and (b)] and Blue-Green [(c) and (d)] sample measurements using GCMS instrument and estimation using the Lafortune model. In (a) and (c) we used data measured with our setup, whereas in (b) and (d) reflectance data was acquired with the GCMS instrument measurements. In all cases, the M_1 fitting metric was used.

Measurement Setup, f_{r_e} represents the data estimated using the optimised micro-facet ABC model, and N is the total number of measurement points (P).

$$Err = \frac{1}{3}\sum_{RGB}\frac{1}{N}\frac{\sum_P | f_{r_m} - f_{r_e} |}{max(f_{r_m})} \tag{12}$$

Figure 8 shows the relative error obtained while using different measurement datasets and both the cost functions.

Figure 9, 10 and 11 show renderings obtained using the Lafortune and micro-facet ABC model optimised using different measurement datasets and cost functions for BMP and the print samples.

5. Discussions

We characterise bidirectional reflectance of two print samples having complex optical properties by analytically calculating sample BRDF with commonly used reflectance models. Goniochromatic and non-diffuse optical properties are visualised using the estimated BRDF.

Referring to Figure 5 and 9, in-plane measurements made using our setup or the GCMS instrument were not sufficient to analytically calculate Lafortune model parameters. The $C_x = C_y$ condition for isotropic materials, along with in-plane only measurements resulted into optimisation converging to sub-optimal local minima, which represents a limitations when using measurements from our setup. Using three free parameters for weighting the dot product in the Lafortune model ($C_x \neq C_y$) could help improving Lafortune model parameters fitting. However, this would require out-of-plane, in order to produce robust estimates. Even though the estimated BRDF shows a good fit with the measurements (Figure 5), the renderings obtained fail to display the goniochromatic properties of the sample. Gold sample renderings (Figure 9 (a)) show a greenish color cast, which we believe is due to the spectral sensitivity functions ($\bar{r}$, $\bar{g}$, and $\bar{b}$) of the camera that was used as a detector.

For the micro-facet ABC model, parameter A (in S_{RGB}) is used as a scaling factor for the specular term resulting into a distribution that is not normalised. This resulted in using a GA method instead of the commonly used optimisation tools to estimate an optimal set of model parameters. For the print samples measured in this paper, the micro-facet ABC model with GA method, as an optimisation tool, was able to visually render the non-diffuse and goniochromatic properties. The cost functions, however, converged to a local minima when optimising for the material refractive index (η) within the Fresnel parameter due to missing information in the grazing directions. In fact, with our setup we were able to acquire very few measurements in the grazing directions, due to setup limitations. A possible solution to this limitation could be replacing the cylinder in our setup with an elliptical surface.

The micro-facet ABC model parameters were optimised using different measurement datasets. In-plane retro-reflective measurements ($\theta_L = 0°$) were sufficient to obtain a good enough rendering for the print samples measured (Figure 10). Adding additional measurements ($\theta_L = -40°$) helped obtain good renderings especially for the goniochromatic Blue-Green sample. The GCMS instrument measurements being sparse (at 5° intervals), struggle with the non-diffuse and goniochromatic properties, compared to measurements with our setup, locally more dense. In fact, our setup can perform dense measurements, depending on the cylinder radius on which the sample is curved, the distance between detector and the sample, and the resolution of the camera used as a detector. Performing measurements using our setup is also faster compared to measuring using the GCMS instrument, as expected.

Referring to the relative error calculated between the measurements and estimated data (Figure 8), performance of both the fitting functions (M_1 and M_2) was objectively not much different. Renderings obtained using the logarithmic cost function (M_2) showed a more realistic renderings including the goniochromatic properties of the Blue-Green sample. A visual difference can be noticed for the BMP sample rendered using the micro-facet ABC model and the two cost functions (M_1 and M_2) (Figure 11).

6. Conclusion

Sample BRDF of two print samples having complex optical properties were estimated and visual renderings were obtained using common reflectance models.

In-plane retro-reflective measurements taken with our setup, along with the GA method as an optimisation tool, was suc-

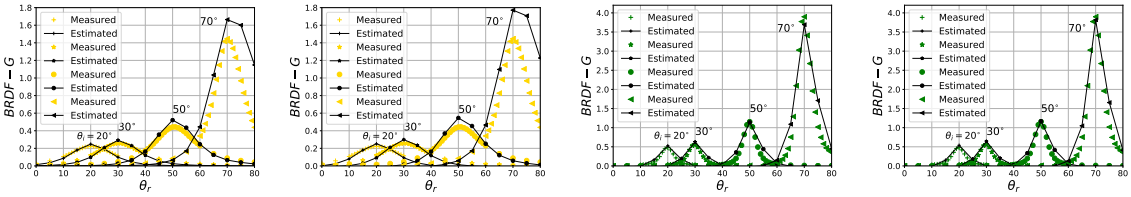

(a) Cost function: M_1, Dataset: GCMS instrument (b) Cost function: M_2, Dataset: GCMS instrument (c) Cost function: M_1, Dataset: GCMS instrument (d) Cost function: M_2, Dataset: GCMS instrument

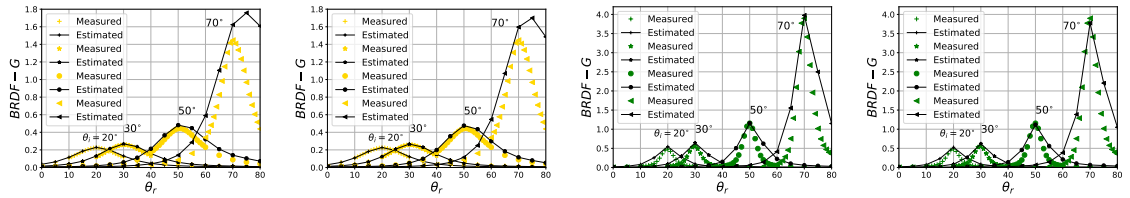

(e) Cost function: M_1, Dataset: Measurement Setup (θ_L = ALL) (f) Cost function: M_2, Dataset: Measurement Setup (θ_L = ALL) (g) Cost function: M_1, Dataset: Measurement Setup (θ_L = ALL) (h) Cost function: M_2, Dataset: Measurement Setup (θ_L = ALL)

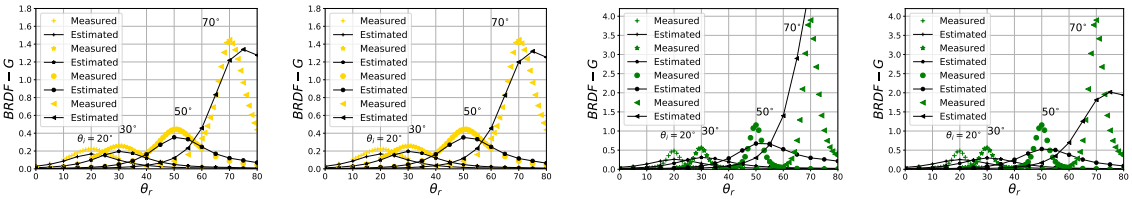

(i) Cost function: M_1, Dataset: Measurement Setup ($\theta_L = 0°$) (j) Cost function: M_2, Dataset: Measurement Setup ($\theta_L = 0°$) (k) Cost function: M_1, Dataset: Measurement Setup ($\theta_L = 0°$) (l) Cost function: M_2, Dataset: Measurement Setup ($\theta_L = 0°$)

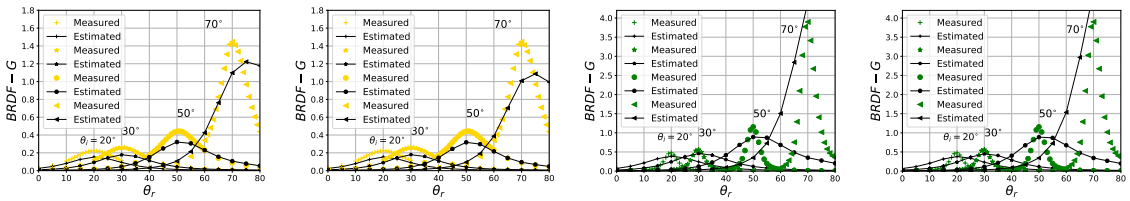

(m) Cost function: M_1, Dataset: Measurement Setup ($\theta_L = 0°$ and 40°) (n) Cost function: M_2, Dataset: Measurement Setup ($\theta_L = 0°$ and 40°) (o) Cost function: M_1, Dataset: Measurement Setup ($\theta_L = 0°$ and 40°) (p) Cost function: M_2, Dataset: Measurement Setup ($\theta_L = 0°$ and 40°)

Fig. 6. G-channel Gold (a) and (b) and Blue-Green (c) and (d) sample measurements using GCMS instrument and estimated using ABC model optimised with Measurement Setup and GCMS instrument measurements.

cessful in estimating an optimal set of the reflectance model parameters. The renderings obtained show that using just in-plane retro-reflective measurements are salient enough to render non-diffuse and goniochromatic properties of the print samples measured. However, more measurements led to better renderings, especially for the goniochromatic sample. In-plane measurements obtained from our setup, as well as from the goniospectrophotometer, were insufficient to find an optimal set of Lafortune model parameters. For the samples measured in this paper, out-of-plane measurements would be needed to calculate material BRDF using the Lafortune model.

The Measurement Setup as a simple and fast measurement tool, along with GA method as an optimisation tool can be further investigated to model and render isotropic and an-isotropic packaging materials with complex optical properties such as discrete sparkles, along with goniochromatism and specularity.

Acknowledgments

References

[1] Maile, FJ, Pfaff, G, Reynders, P. Effect pigmentspast, present and future. Progress in Organic Coatings 2005;54(3):150 – 163. doi:10.1016/j.porgcoat.2005.07.003.

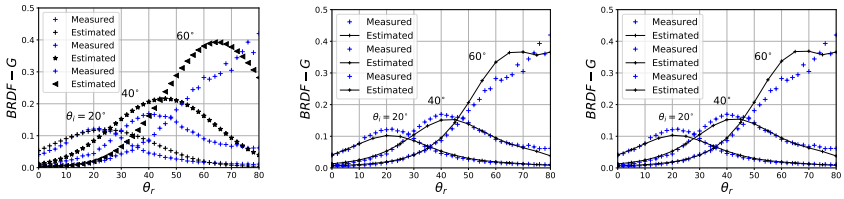

(a) Cost function: M_1, Lafortune model

(b) Cost function: M_1, Micro-facet ABC model

(c) Cost function: M_2, Micro-facet ABC model

Fig. 7. G-channel BMP sample measurements from the MERL dataset and estimated using Lafortune model (a) and ABC model (b, c) optimised using in-plane MERL dataset measurements and both the cost functions.

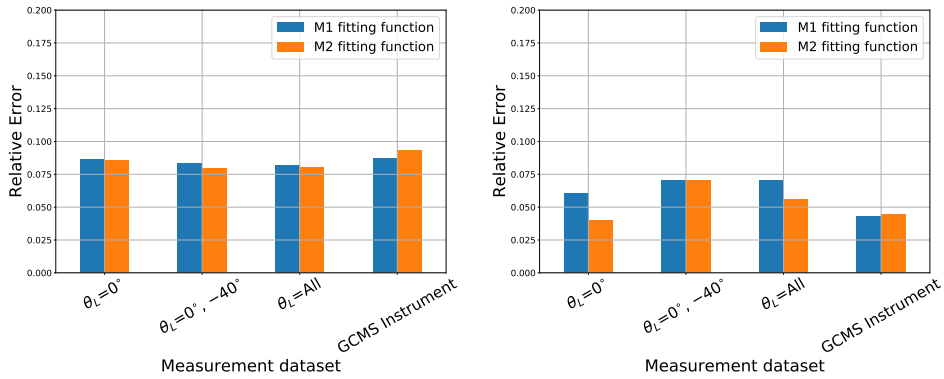

(a) Gold sample

(b) Blue-Green sample

Fig. 8. Relative error calculated using Equation (12) between the measured and estimated measurement data using ABC model optimised with different measurement datasets.

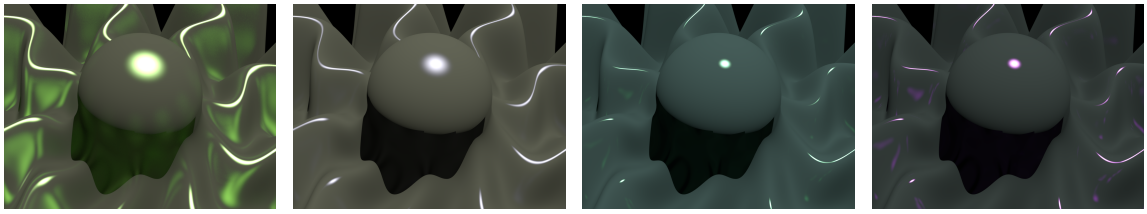

(a) Measurement Setup

(b) GCMS instrument

(c) Measurement Setup

(d) GCMS instrument

Fig. 9. Comparison of the rendered images using our setup and the GCMS instrument. G-channel Gold (sub-figure (a) and (b)) and Blue-Green (sub-figure (c) and (d)). In all cases the M_1 fitting function was used.

[2] Kehren, K. Optical properties and visual appearance of printed special effect colors. Ph.D. thesis; Technischen Universität Darmstadt; Darmstadt, Germany; 2013.

[3] Eugène, C. Measurement of "total visual appearance": a cie challenge of soft metrology. In: 12th IMEKO TC1 and TC7 Joint Symposium on Man, Science and Measurement. Annecy, France; 2008, p. 61 – 65.

[4] McCamy, C. Observation and measurement of the appearance of metallic materials. part i. macro appearance. Color Research & Application 1996;21(4):292–304.

[5] Guarnera, D, Guarnera, G, Ghosh, A, Denk, C, Glencross, M. Brdf representation and acquisition. Computer Graphics Forum 2016;35(2):625–650. doi:10.1111/cgf.12867.

[6] Ashikhmin, M, Premoze, S. Distribution-based brdfs. Unpublished Technical Report 2007;:10.

[7] Guo, J, Pan, J. A physically-based brdf model for retroreflection. In: Proceedings of the Computer Graphics International Conference. ACM; 2017, p. 36.

[8] Guo, J, Guo, Yw, Pan, Jg. A retroreflective brdf model based on prismatic sheeting and microfacet theory. Graphical Models 2018;96:38–46.

[9] Dupuy, J, Jakob, W. An adaptive parameterization for efficient material acquisition and rendering. Transactions on Graphics (Proceedings of SIGGRAPH Asia) 2018;37(6):274:1–274:18. doi:10.1145/3272127.3275059.

[10] Löw, J, Kronander, J, Ynnerman, A, Unger, J. Brdf models for accurate and efficient rendering of glossy surfaces. ACM Transactions on Graphics (TOG) 2012;31(1):9.

[11] Matusik, W. A data-driven reflectance model. Ph.D. thesis; Massachusetts Institute of Technology; 2003.

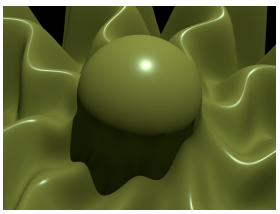

(a) Cost function: M_1, Dataset: GCMS instrument

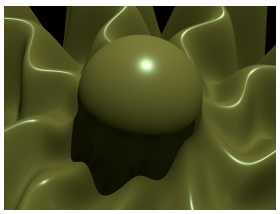

(b) Cost function: M_2, Dataset: GCMS instrument

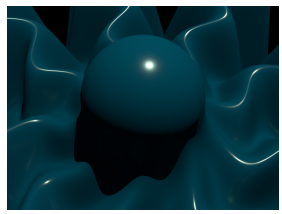

(c) Cost function: M_1, Dataset: GCMS instrument

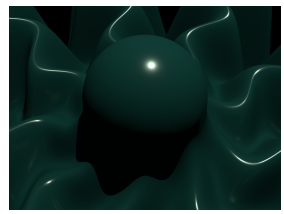

(d) Cost function: M_2, Dataset: GCMS instrument

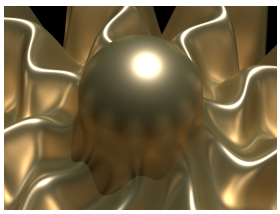

(e) Cost function: M_1, Dataset: Measurement Setup (θ_L = ALL)

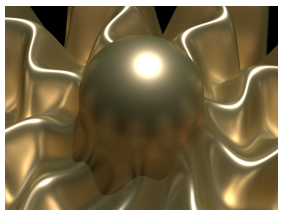

(f) Cost function: M_2, Dataset: Measurement Setup (θ_L = ALL)

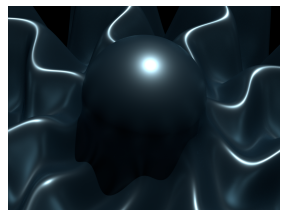

(g) Cost function: M_1, Dataset: Measurement Setup (θ_L = ALL)

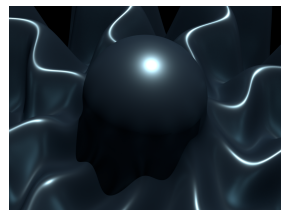

(h) Cost function: M_2, Dataset: Measurement Setup (θ_L = ALL)

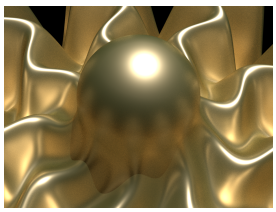

(i) Cost function: M_1, Dataset: Measurement Setup ($\theta_L = 0°$)

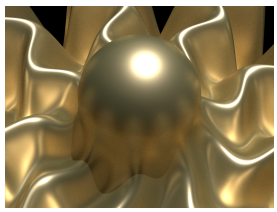

(j) Cost function: M_2, Dataset: Measurement Setup ($\theta_L = 0°$)

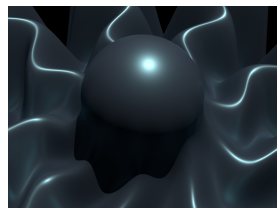

(k) Cost function: M_1, Dataset: Measurement Setup ($\theta_L = 0°$)

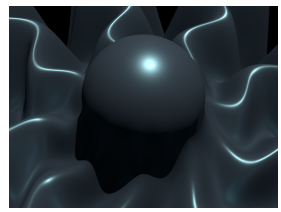

(l) Cost function: M_2, Dataset: Measurement Setup ($\theta_L = 0°$)

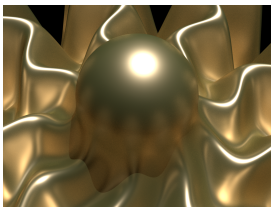

(m) Cost function: M_1, Dataset: Measurement Setup (θ_L = 0° and 40°)

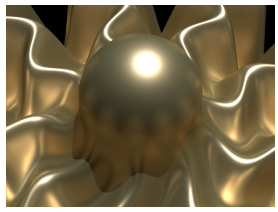

(n) Cost function: M_2, Dataset: Measurement Setup (θ_L = 0° and 40°)

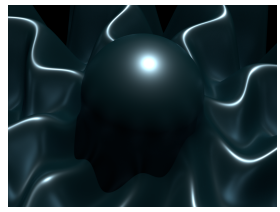

(o) Cost function: M_1, Dataset: Measurement Setup (θ_L = 0° and 40°)

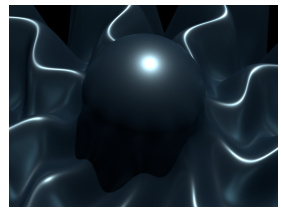

(p) Cost function: M_2, Dataset: Measurement Setup (θ_L = 0° and 40°)

Fig. 10. G-channel Gold (a) and (b) and Blue-Green (c) and (d) sample renderings using the micro-facet ABC model. The input data is measured using the GCMS instrument (first row) and using our setup (second, third and last row).

[12] Nicodemus, FE, Richmond, J, Hsia, JJ, Ginsberg, IW, Limperis, T. Geometrical considerations and nomenclature for reflectance. National Bureau of Standards; 1977.

[13] Rong Lu, J, Koenderink, J, Kappers, AML. Optical properties (bidirectional reflection distribution functions) of velvet. Applied Optics 1998;37(25):5974 – 5984.

[14] Marschner, SR, Westin, SH, Lafortune, EPF, Torrance, KE, Greenberg, DP. Image-based brdf measurement including human skin. In: 10th Eurographics Workshop on Rendering. 1999, p. 139 – 152.

[15] Tominaga, S, Tanaka, N. Estimating reflection parameters from a single color image. IEEE Computer Graphics and Applications 2000;20(5):58 – 66.

[16] Matusik, W, Pfister, H, Brand, M, McMillan, L. A data-driven reflectance model. ACM Transactions on Graphics 2003;22(3):759–769.

[17] Ngan, A, Durand, F, Matusik, W. Experimental analysis of brdf models. Rendering Techniques 2005;2005(16th):2.

[18] Sole, A, Farup, I, Nussbaum, P, Tominaga, S. Bidirectional reflectance measurement and reflection model fitting of complex materials using an image-based measurement setup. Journal of Imaging 2018;4(11). doi:10.3390/jimaging4110136.

[19] Cook, RL, Torrance, KE. A reflectance model for computer graphics. ACM Trans Graph 1982;1(1):7–24. doi:10.1145/357290.357293.

[20] Ward, GJ. Measuring and modeling anisotropic reflection. SIGGRAPH Comput Graph 1992;26(2):265–272. doi:10.1145/142920.134078.

[21] Nelder, JA, Mead, R. A simplex method for function minimization. The Computer Journal 1965;7(4):308 – 313.

[22] Lafortune, EPF, Foo, SC, Torrance, KE, Greenberg, DP. Non-linear approximation of reflectance functions. In: Proceedings of the 24th An-

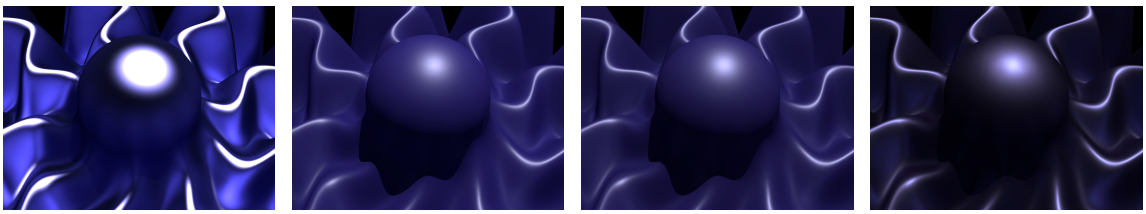

(a) BMP sample - in-plane dataset, M_1, Lafortune model

(b) BMP sample - in-plane dataset, M_1, ABC model

(c) BMP sample - in-plane dataset, M_2, ABC model

(d) BMP sample - full MERL BMP sample dataset

Fig. 11. G-channel BMP sample rendering using full BRDF measurement dataset and the Lafortune and micro-facet ABC model optimised using in-plane MERL dataset measurements.

nual Conference on Computer Graphics and Interactive Techniques. SIGGRAPH '97; New York, NY, USA: ACM Press/Addison-Wesley Publishing Co. ISBN 0-89791-896-7; 1997, p. 117–126. doi:10.1145/258734.258801.

[23] Phong, BT. Illumination for computer generated pictures. Commun ACM 1975;18(6):311–317. doi:10.1145/360825.360839.

[24] Church, EL, Takacs, PZ, Leonard, TA. The prediction of brdfs from surface profile measurements. In: Scatter from Optical Components; vol. 1165. International Society for Optics and Photonics; 1990, p. 136–151.

[25] Church, EL, Takacs, PZ. Optimal estimation of finish parameters. In: Optical Scatter: Applications, Measurement, and Theory; vol. 1530. International Society for Optics and Photonics; 1991, p. 71–86.

[26] Palmer, J, Grant, BG. The Art of Radiometry. ISBN 978-0-8194-7245-8; SPIE Press Bellingham, Washington USA; 2010.

[27] Höpe, A, Hauer, KO. Three-dimensional appearance characterization of diffuse standard reflection materials. Metrologia 2010;47(3):295.

[28] Brady, A, Lawrence, J, Peers, P, Weimer, W. genbrdf: discovering new analytic brdfs with genetic programming. ACM Transactions on Graphics (TOG) 2014;33(4):114.

[29] Guarnera, D, Guarnera, GC, Toscani, M, Glencross, M, Li, B, Hardeberg, JY, et al. Perceptually validated cross-renderer analytical brdf parameter remapping 2018;.

[30] Serrano, A, Gutierrez, D, Myszkowski, K, Seidel, HP, Masia, B. An intuitive control space for material appearance. ACM Trans Graph 2016;35(6):186:1–186:12.

[31] Jakob, W. Mitsuba renderer, 2010. 2010.

[32] Havran, V, Filip, J, Myszkowski, K. Perceptually motivated brdf comparison using single image. In: Computer Graphics Forum; vol. 35. Wiley Online Library; 2016, p. 1–12.